DEVELOPMENT OF MICRO-GRINDING MECHANICS AND MACHINE TOOLS

A Dissertation
Presented to
The Academic Faculty

By

Hyung Wook Park

In Partial Fulfillment
of the Requirements for the Degree
of Doctor of Philosophy in the
George W. Woodruff School of Mechanical Engineering

Georgia Institute of Technology
April, 2008

DEVELOPMENT OF MICRO-GRINDING MECHANICS AND MACHINE TOOLS

Approved by:

Dr. Steven Y. Liang, Advisor
George W. Woodruff School of Mechanical Engineering
Georgia Institute of Technology

Dr. Chen Zhou
H. Milton Stewart School of Industrial and Systems Engineering
Georgia Institute of Technology

Dr. Steven Danyluk
George W. Woodruff School of Mechanical Engineering
Georgia Institute of Technology

Dr. Paul Griffin
H. Milton Stewart School of Industrial and Systems Engineering
Georgia Institute of Technology

Dr. Shreyes N. Melkote
George W. Woodruff School of Mechanical Engineering
Georgia Institute of Technology

Date Approved: 12/19/2007

ACKNOWLEDGEMENTS

I would, first of all, like to thank my advisor Dr. Steven Y. Liang for all the support, guidance and encouragement throughout the course of my graduate study. I would also like to thank the members of my thesis committee, Professors Shreyes Melkote, Steven Danyluk, Chen Zhou and Paul Griffin. Thanks are also due to Steven Sheffield for his assistance in conducting my experiments. I would also like to thank all the support staff in MARC and ME for all their help especially John Morehouse, Pam Rountree, Glenda Johnson, Trudy Allen and Wanda Joefield.

I would like to thank my colleagues, Siva, Ramesh Singh, Sathyan Subbiah, Jiann-Cherng Su, Kuan-Ming Li, Adam Cardi, Carl Hanna, Qiulin Xie, Injoong Kim, Sangil and Haiyan Deng for their help and support during my stay at Georgia Tech.

Finally, I would like to thank my family and my wife, Jinae lee, for their love, support, encouragement and understanding throughout my graduate study. This thesis would not be possible without them.

TABLE OF CONTENTS

LIST OF TABLES

LIST OF FIGURES

LIST OF SYMBOLS

r	cutting edge radius
t_m	minimum undeformed chip thickness
α_{cr}	critical rake angle
α_s	effective rake angle
t_0	undeformed chip thickness
τ	shear strength
φ	angle of inclination
β_i	instantaneous friction angle
α_i	instantaneous friction angle
ϕ_i	nominal friction angle
$F_{cg,x}$, $F_{cg,y}$	chip formation forces per grit
$dF_{cg,x}$, $dF_{cg,y}$	differential chip formation forces per grit
$F_{pg,x}$, $F_{pg,y}$	ploughing forces per grit in the normal and tangential directions
$F_{brinell}$	Brinell hardness force
HB	Brinell hardness
μ_p	ploughing friction coefficient
w	width of indentation
D	ball diameter
b	diameter of the impression
A,B,C , m , n	Johnson-Cook model coefficients

ϕ_n, α_n	nominal shear and rake angles
l_s	length of a shear plane
C_{oxley}	Oxley's constant
V_{sh}	shear velocity
V_w	feedrate
V_s	grinding velocity
$\varepsilon, \dot{\varepsilon}$	strain and strain rate
$\gamma, \dot{\gamma}$	shear strain and strain rate
$\upsilon_{chip}, \upsilon_{work}$	volume ratios of the chip and workpiece deformation
ν	Poisson ratio
M	Taylor factor
α_{cont}	material's constant
b_{bg}	burger vector of dislocations
ρ_t	total dislocation density
ρ_0	dislocation density in the volume between boundaries
ρ_b	dislocation density per unit volume
D_d	average grain diameter
k	constant of the geometry boundary
K_{HP}	Hall-Petch coefficient
G	shear modulus
θ_{av}	average misorientation

d_e	diameter of the micro-grinding wheel
q, q_o	heat flux
T_m	melting point of material
T_o	environment temperature
T	material temperature
l_c	contact length
R_r	roughness factor
R_w	heat partition ratio to the workpiece
R_s	heat partition ratio to the micro-grinding wheel
e_c	process specific energy
e_c	energy to melt the workpiece materials
k_g	grit thermal conductivity
k_c	thermal conductivity
ρ	density
c	specific heat
C_s	static grit density
C_d	dynamic grit density
c_g	constant of the dynamic effect
θ_{infeed}	infeed angle
A_s, k_s	constants of regression
$E(X)$	expectation

$Var(X)$	variance
E	modulus of elasticity
I	moment of inertia
A_b, B_b, C_b	constants of machine dimensions
α_t	thermal expansion coefficient
$[M]$	mass matrix
$[C]$	damping matrix
$[K]$	joint stiffness matrix
$[G(w)]$	receptance matrix
ω	rotational frequency
α_R, β_R	constants of Rayleigh damping model
ξ_i	damping ratio
ω_{ni}	rotational frequency in mode i
$\alpha_{ei}, \beta_{ei}, \gamma_{ei}$	rotation errors
$\delta_{xei}, \delta_{yei}, \delta_{zei}$	translation errors
C_i	weighing factor

SUMMARY

Micro-grinding with microscale machine tools is a micro-machining process in precision manufacturing of microscale parts such as micro sensors, micro actuators, micro fluidic devices, and micro machine parts. Mechanical micro-machining generally consists of various material removal processes. Micro-grinding of these processes is typically the final process step and it provides a competitive edge over other fabrication processes. The quality of the parts produced by this process is affected by process conditions, micro-grinding wheel properties, and microstructure of materials. Although a micro-grinding process resembles a traditional grinding process, this process is distinctive due to the size effect in micro-machining because the mechanical and thermal interactions between a single grit and a workpiece are related to the phenomena observed in micro-machining. However, there have not been enough modeling studies of the micro-grinding process and as a result, little knowledge base on this area has been accumulated.

In this study, the new predictive model for the micro-grinding process was developed by consolidating mechanical and thermal effects within the single grit interaction model at microscale material removal. The size effect of micro-machining was also included in the proposed model. In order to assess thermal effects, the heat partition ratio was experimentally calibrated and compared with the prediction of the Hahn model. Then, on the basis of this predictive model, a comparison between experimental data and analytical predictions was conducted in view of the overall micro-grinding forces in the x and y directions. Although there are deviations in the predicted

micro-grinding forces at low depths of cut, these differences are reduced as the depth of cut increases. On the other hand, the optimization of micro machine tools was performed on the basis of the proposed design strategy. Individual mathematical modeling of key parameters such as volumetric error, machine working space, and static, thermal, and dynamic stiffness were conducted and supplemented with experimental analysis using a hammer impact test. These computations yield the optimal size of miniaturized machine tools with the technical information of other parameters.

CHAPTER 1

INTRODUCTION

1.1 Background

Manufacturing technology has advanced to higher levels of precision to satisfy the increasing demand to reduce the size of parts and products in the electronics, computer, and biomedical industrial sectors. New processing concepts, procedures and machines are thus needed to fulfill the increasingly stringent requirements and expectations.

Mechanical micro-machining is an emerging technology carrying large benefits and equally great challenges in fabrication of microscale parts. Existing micro-machining processes can be broadly classified into mechanical micro-machining, chemical-mechanical micro-machining, high energy beams-based machining, and scanning probe micro-machining in Figure 1-1.

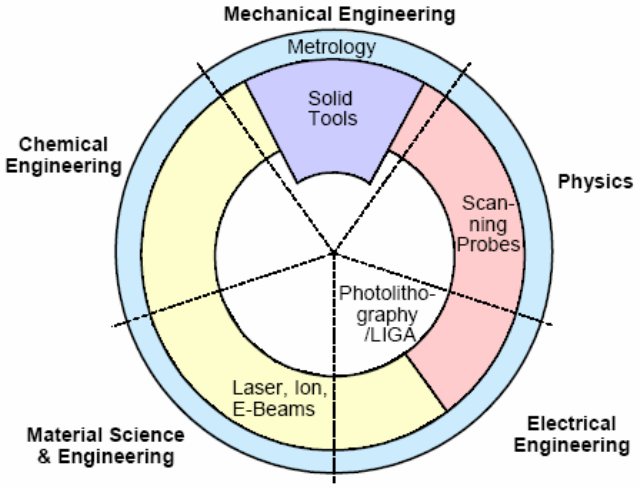

Figure 1-1: Disciplinary areas for various micro manufacturing by Liang [1]

Among these technologies, mechanical micro-machining using miniaturized machine tools is one research direction and it has a number of inherent advantages. These advantages include: the significant reduction of required space and energy consumption for machine drive; the improvement of machine robustness against external error sources due to increasing thermal, static, and dynamic stabilities; increased positioning accuracy due to decreased overall size of machine; and a greater freedom in the selection of work-piece materials, the complexity of the product geometry, and the cost of investment.

Mechanical micro-machining generally consists of various material removal processes. Within these processes, micro-grinding is typically the final process step and like conventional grinding, it provides a competitive edge over other processes in fabrication of microscale parts such as micro sensors, micro actuators, micro fluidic devices, and micro machine parts. But, since conventional grinding wheels are very large compared to target products, their capability is usually limited to grinding simple parts as indicated in Figure 1-2.

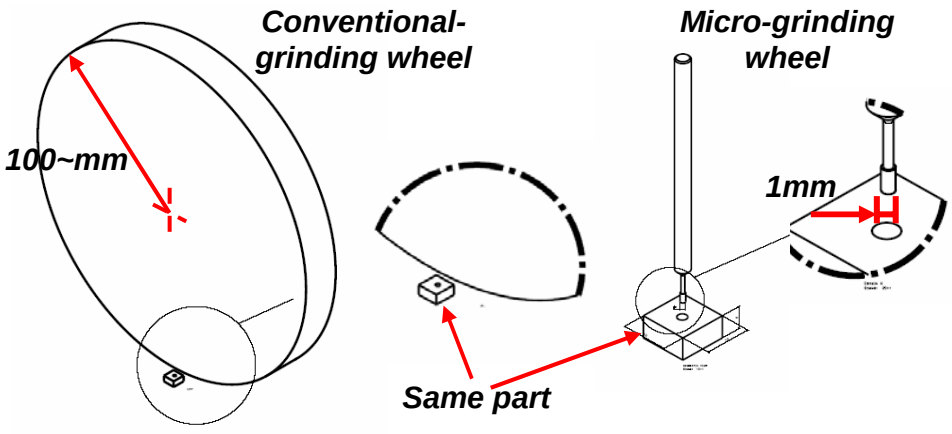

Figure 1-2: Fabrication of microscale parts using conventional and micro grinding

On the other hand, although a micro-grinding process resembles a conventional grinding process, this process is distinctive due to the size effect in micro-machining whereby the mechanical and thermal interactions between a single grit and a workpiece are related to the phenomena observed in micro-machining, which are summarized in Table 1-1.

The quality of the parts produced by this process is influenced by process conditions, micro-grinding wheel properties, and microstructure of materials. However, there have not been enough modeling studies of the micro-grinding process and as a result, little knowledge in this area has been accumulated

As the diameter of grinding wheels decrease, the negligible effects in the conventional grinding process such as ploughing forces and grinding wheel deformation becomes more important in micro-grinding. Although the boundary between micro and conventional grinding is not clear, micro-grinding is not simply reduction of the conventional grinding process, which is shown in Figure 1-3.

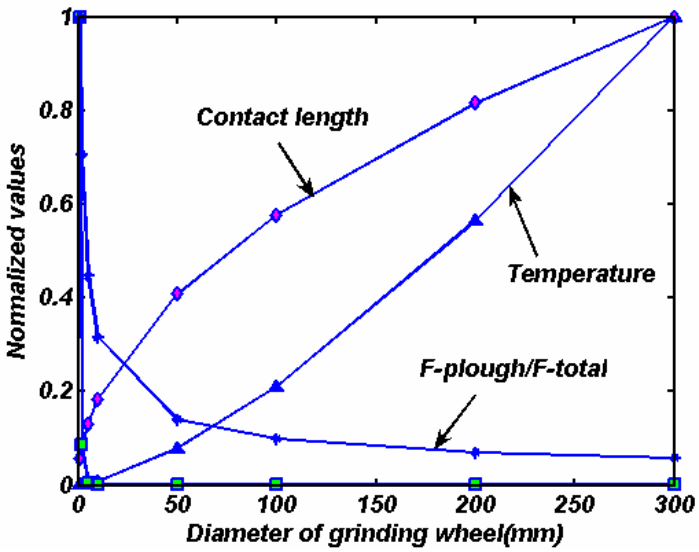

Figure 1-3: Variation trend of main parameter according to varying wheel dimensions

The quality of the parts produced by this process is influenced by process conditions, micro-grinding wheel properties, and microstructure of materials. However, there have not been enough modeling studies of the micro-grinding process and as a result, little knowledge in this area has been accumulated.

Table 1-1: Characteristics of the micro-grinding process

	Macro-grinding	Micro-grinding
Ratio of the depth of cut to the grit radius	50-100	0.1-1
Ploughing Effect	Not significant($\approx 0\%$)	Significant($\approx 20-30\%$)
Friction on the interface	$\mu = \mu_c$	$\mu = \mu_c(depth\ of\ cut) + \mu_p$
Rake angle	Constant negative	Variable negative
Material removal rate	$10^{n} \sim 10^{-1} mm^3 / mm \cdot s$	$10^{-1} \sim 10^{-3} mm^3 / mm \cdot s$

In addition to the above research problems, in view of the design of micro machine tools, miniaturization of traditional machine tools unavoidably reduces the available work volume, prohibiting the unrestricted reduction of machine size. Therefore, at a conceptual design stage, optimization in terms of a machine size and configuration must address competing issues at the functionality level of machine tools. For microscale machine tools, the overall structural size of the machine tool can be an important contributor to the achievable precision and economic justification. The reduction of machine tool structural volume by several thousand times from that of traditional machine tools is technically feasible. From the standpoint of economic benefits, the miniaturization of machine tools can lead to the reduction of the occupied floor space, consumed energy, machine structure material cost, the expense for machine transportation, and the cost for flexible automation. On the technical performance side,

smaller manufacturing systems can provide higher static rigidity, thermal resistance, and dynamic stiffness, thereby improving machining accuracy and precision. Recently, the shapes of miniaturized machine tools have become more complex and precise. However, there has not been enough discussion to provide a basic approach to the suitable configuration for the design parameters of microscale manufacturing systems because the previous design procedure of commercial manufacturing systems depends on designer and company experience.

1.2 Research objective

Micro-grinding with miniaturized machine tools is an emerging area due to possible impacts on the industrial field. Although there are many efforts to model the conventional grinding process by experimental and analytical methods, these are limited to grinding with a conventional grinding wheel.

In this research, after reviewing work relevant to micro-grinding with miniaturized machine tools, in order to predict the micro-grinding force as a function of the kinematics of the grinding process and wheel topography, the following tasks were undertaken:

- Development of the single grit interaction between the workpiece and the abrasive particle considering the size effects.
- Assessment and modeling of the thermal effects in micro-grinding.
- Calibration of the heat partition ratio in micro-grinding.

- Characterization of the micro-grinding wheel.
- Development of a material model incorporating crystallographic effects
- Model validation with experimental data.

Micro-grinding is carried out using miniaturized machine tools. So optimization of the structure of miniaturized machine tools has to be pursued. To optimize the size of machine structure according to different machine configurations and sizes, in this research, the following tasks are taken

- Development of mathematical models of key parameters such as volumetric error, machine working space, and static, thermal, and dynamic stiffness
- Optimization and sensitivity analysis of the weighing factors

1.3 Dissertation organization

This dissertation is laid out as follows in Figure 1-4. Chapter 2 describes the literature and relevant works in microscale machine tools, physical modeling of the conventional grinding process, and mechanical micromachining. Modeling of the single grit interaction for micro-grinding and modeling of thermal effects in micro-grinding with calibration of the heat partition ratio to the workpiece is presented in Chapter 3.

Experimental and analytical studies of the micro-grinding wheel topography are described in Chapter 4. Chapter 5 describes experiments of micro-grinding forces and microstructure and comparison between experimental data and predictions. Optimization of the size of machine tool structure is described in Chapter 6. Finally, Chapter 7 describes the conclusions and the recommendations for future research.

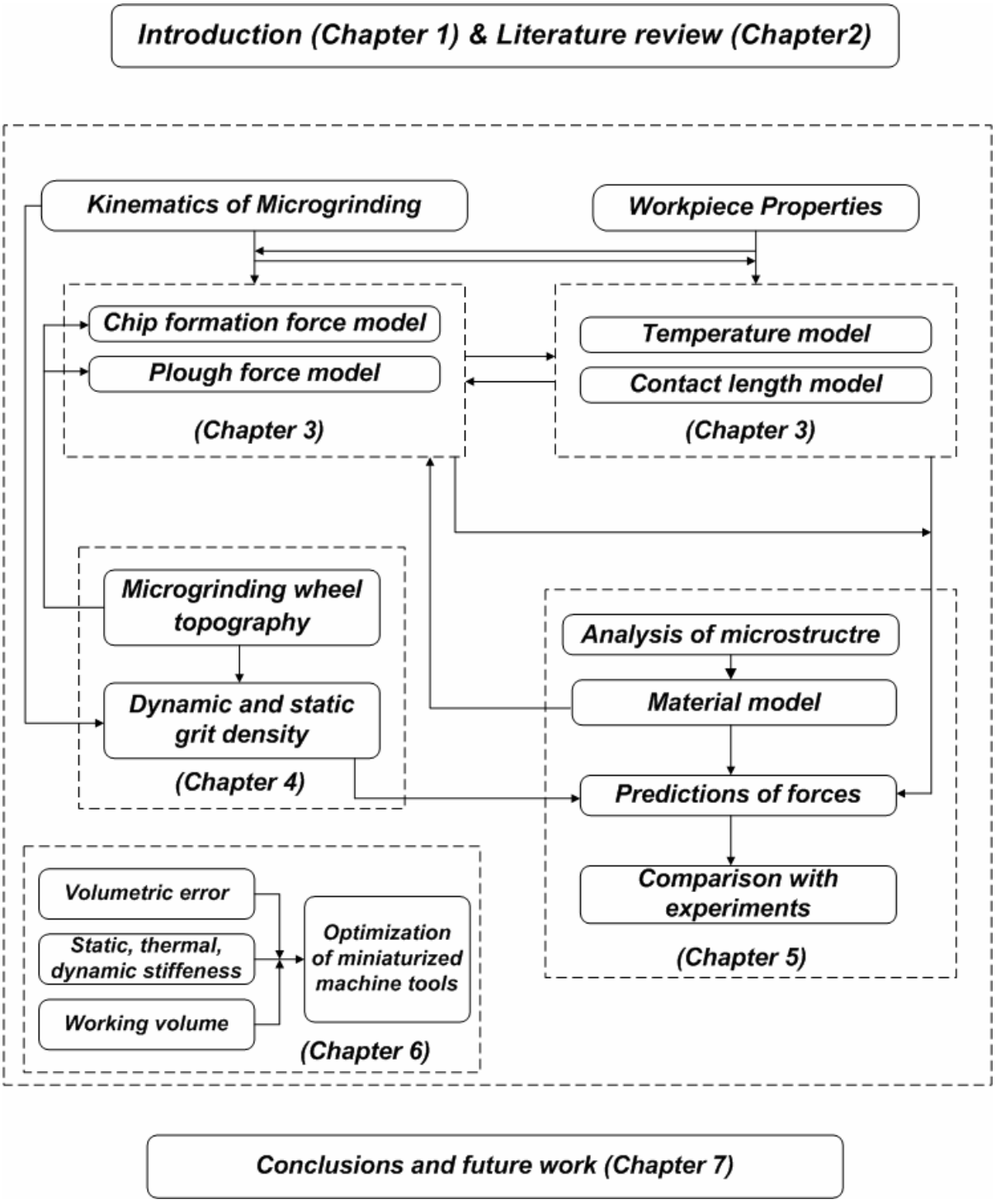

Figure 1-4: Flow chart of thesis organization

CHAPTER 2

LITERATURE REVIEW

This chapter presents a review of literature in relevant areas to the proposed works. These works provide an overview of past and current research relating to microscale machining which covers microscale machining using solid tools and fabrication of microscale precision machines. A general synopsis of the literature review is conveniently divided into three groups: (i) Microscale manufacturing systems, (ii) Physical modeling of conventional grinding, (iii) Micromachining. The research on microscale manufacturing systems will include reviews on the recent development of prototypes such as micro lathes, micro turning, and design methodology of microscale machine tools. Physical modeling of conventional grinding will include information on mechanical interaction modeling, thermal effect modeling, and grinding wheel topography. The literature review of the size effect will discuss experimental and analytical studies of these effects.

2.1 Micro/meso-scale machine tools

Increasing demand for fabrication of microscale parts in electronic, computer, and biomedical industrial sectors has created the need to minimize conventional machine tools because the size of their target's product is small compared to their size. In view of this, the development of micro and meso scale machine tools has become an attractive

area to researchers. Many attempts to fabricate microscale prototype machine tools have been conducted, primarily understand the underlying mechanisms of microscale machine tools. Current research in microscale machine tools can be broadly classified into two groups: (i) Construction and evaluation of various prototypes of microscale machine tools and (ii) Design of microscale machine tools.

2.1.1 Current developments on microscale machine tools

Economic aspects such as cost savings of consumed power and used floor space and technical advantages such as reduction of thermal deformation and enhancements of static and dynamic stabilities[2, 3] have driven the development of smaller machine tools. In the late 1980s, Japanese engineers started to develop prototypes of microscale machine tools with the support of the Japanese government. Most researches at this early stage sought to develop various prototypes of microscale machine tools [4-6]. In the earliest attempt to develop a prototype of a microscale machine tool, a micro lathe was developed by Kitahara *et al.*[4]. It has dimensions of 32mmx25mmx30.5mm. This machine consists of an X-Y moving unit driven by a laminated piezo actuator and a small main shaft driven by a micro motor. Its power consumption is 1/1000 that of a conventional lathe. Lu and Yoneyama[5] summarized the growing issues of development of the microscale machine tools and developed a new micro turning system which has a new point tool. It is applied to a micro turning at an elevated rotation speed. Mishima *et al.*[6] developed a micro factory consisting of three machine tools and two small manipulators. This factory shows the capability to fabricate a ball bearing. Vogler *et al.*[7] developed a meso scale

machine tool with the dimensions of 25x25x25mm. In this research, two new major concepts of driving were relative accuracy and volumetric utilization.

Some early successes in the development of microscale machine tools and some recent advances in component technologies including the high speed spindle, positioning table, handling system, and metrology system[8] provide a foundation for the development of more accurate and better performance microscale machine tools. Based on previous design experiences and prototypes, second generation microscale machine tools have been developed at national laboratories and academic institutions around the globe. Rahman et al.[9] developed a CNC micro turning machine tool. Its dimensions are 560x600x660 mm and each axis has an optical linear scale with resolution of 0.1μm. Kurita et al.[10] developed a CNC multiprocess machine tool. This machine tool has five changeable machining heads and dimensions of 557×604×655mm. In this study, the machining energy of products and installation space volume of the developed machine tool are compared with those of conventional machine tools in Figure 2-1.

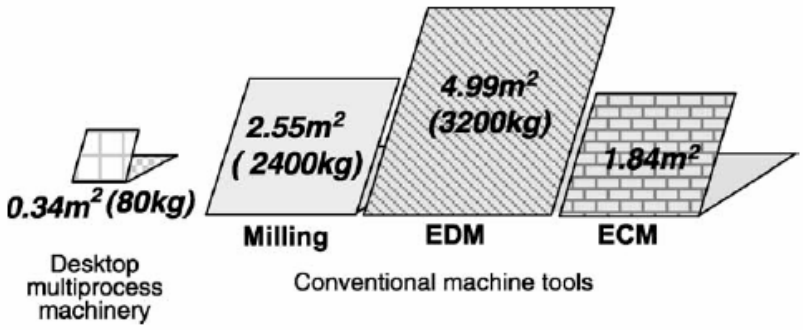

Figure 2-1: Installation space of various machine tool

Lee et al.[11] developed a CNC based microscale machine tool which is used to machine the V-groove substrate as an optical fiber in Figure 2-2(a). In this study, this

developed machine shows the physical capability to machine an arbitrary 3D shape. It indicates that the stiffness of a machine tool is closely related to the quality of the products. The university of Illinois at Urbana-Champaign[8] developed a micro milling machine. Its dimensions are 180×180×300mm and the movement travel range is 25×25×25mm. This machine is a three axis horizontal microscale machine tool with voice coil motors, a 160k RPM air-turbine, air bearing spindle, and 0.1mm encoder resolution as shown in Figure 2-2(b).

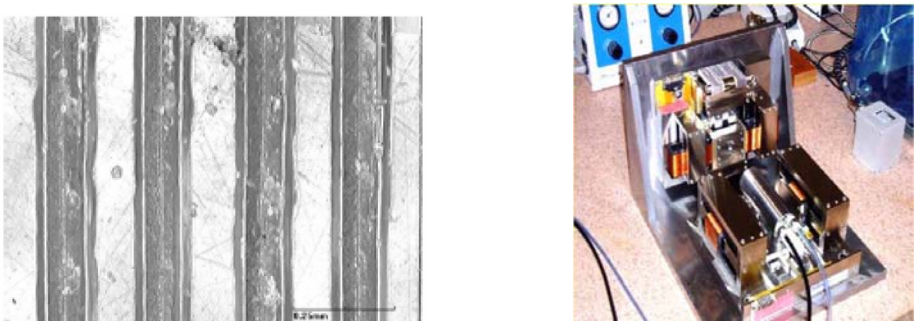

(a) (b)

Figure 2-2: (a) Machined grooves[11] and (b) 2nd generation UIUC Miniature Machine Tool[8]

Consequently, extensive researches involving the recent developments of microscale machine tools like Chen et al.[12] ,Cox et al.[2], Okazaki et al.[13], and Lin et al.[14] have been pursued. In order to provide further improvement of these microscale machine tools, fundamental understanding of the issues in microscale machine tools is needed.

2.1.2 Technical review of component technologies

This section covers the current state of unit technologies because these are important to the development of better microscale machine tools. These components include a miniature spindle, positioning table, machine frame, and visual system. Kapoor et al.[8] and Williams et al.[15] summarized recent advances of component technologies. The position tables of current microscale machine tools can be categorized into the following groups: (i) the actuators based on piezoelectric mechanism [16] (ii) a linear motor with a crossed motor and (iii) voice coil actuated technology. In microscale machine tools, a spindle component has to run at high speed and has a very low runout. Current spindle research is focusing on achieving these requirements. Based on current advances of spindle technologies and reduction of a spindle size, possible spindles of microscale machine tools are air turbine spindle, dental handpieces, and brushless DC motor. Due to the requirements such as high stiffness and low thermal response, Invar 36 steel alloy is often used to provide structural stiffness to microscale machine tools. Currently, advances in fabricating microscale tools such as micro milling cutter, micro drill, and micro grinding wheels provide microscale tools which are less than 1mm in diameter as shown in Figure 2-3. The material and geometry of microscale tools are crucial factors because the size of the tool limits the feature size.

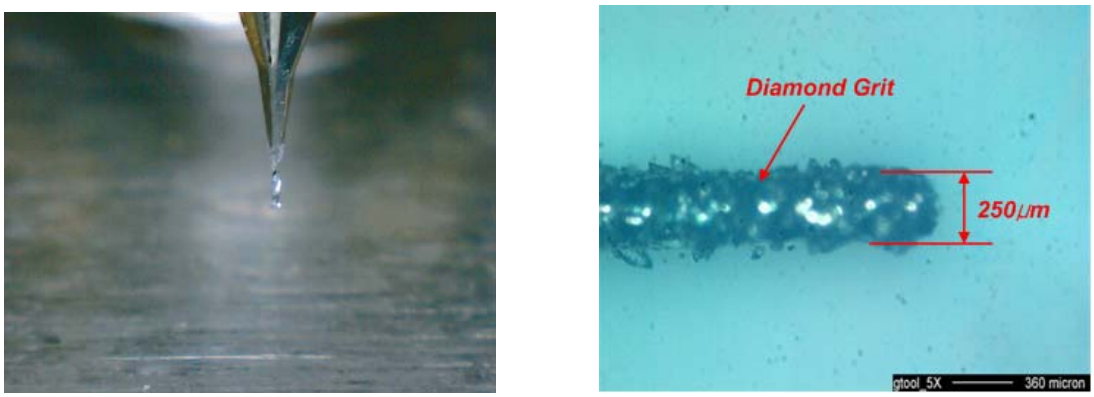

(a) (b)

Figure 2-3: (a) 100 μm micro milling cutter and (b) 250μm micro grinding wheel

In microscale machine tools, although an inspection system doesn't affect the micromachining process, it is an important device to ensure good performance of microscale machine tools. Due to the feature size of this process, observation of micromachining processes using magnification is needed. Generally, optical magnification cameras have been used in microscale machine tools because there is a limitation of machine space.

2.1.3 Design methodology of microscale machine tools

In the case of traditional machine tools, the design methodology has matured through experimental learning and methodological improvement[17]. However, there is not enough accumulated knowledge for microscale machine tool design based on experience and knowledge. There is no sufficient discussion devoted to the optimization of individual miniaturized machine designs. As of yet, fairly little design experience and knowledge base toward miniaturization of a manufacturing system have been

accumulated. Although several attempts have been made [12, 18, 19], the optimal size of the miniaturized machine tool has not yet been systematically attained.

At the beginning of the research for miniaturized machine tools design, Mishima *et* al.[20, 6, 19] presented a design evaluation method for miniaturized machine tools. This method adopted a kinematic representation of machine structures with the Taguchi method to estimate the contribution of each local error component, which serves as proper background for this study. In this study, results showed that the spindle whirling error and horizontal direction error of the feed unit have a considerable influence on machining accuracy. Chen et al.[12] developed a novel virtual machine tool (VMT) integrated design environment in which kinematic functionality was embedded in the description of the sub-components. It was found that the results of the VMT configuration analysis for miniaturized machine tools are similar with configuration candidates of traditional machine tools. In these studies, volumetric error for various machine configurations is used as a key criterion to estimate the proper configuration for miniaturized machine tools. Recent work by Lee et al.[18] studies the dynamic behavior characterization of a mesoscale machine tool (mMT). In this study, the size effect in the dynamic behavior of the mMT was investigated experimentally and numerically. The outcomes show that the characterization of the dynamic properties of the joints of mMTs is an important factor in determining the dynamic behavior of mMTs. However, previous works in Table 2-1 don't provide information about the optimal dimensions per each design configuration.

In design of traditional and miniaturized machine tools, a conceptual design stage of all major elements is important. This step defines basic features and capabilities of

traditional and miniaturized machine tools. In the case of miniaturized machine tools, this design stage acquires more importance because the ratio of the overall size of the miniaturized machine tools to the target products significantly decreases compared to traditional machine tools. The conceptual design for miniaturized machine tools has to be accompanied with comprehensive analyses of possible effective factors such as static, dynamic, and thermal stiffness, machine accuracy, and machine working volume.

Table 2-1: Category of previous works

	Mishima et al.[20]	Chen et al.[12]	Lee et al.[18]
Geometrical error	Error transformation matrix and form shaping function	Multi-axis kinematic error module	N/A
Dynamic stiffness	N/A	N/A	Structural dynamics of machine tools and scaling analysis
Thermal/static stiffness	N/A	N/A	N/A
Others	Effect of design parameters and error components	Development of a comprehensive integrated design environment	An equivalent lumped parameter model

2.2 Introduction of the micro-grinding process

Micro-grinding apparently resembles the conventional grinding process in terms of its stochastic characteristics. It is distinctive in view of the size effect on the interaction between a single grit and the workpiece. Analytical modeling of micro-grinding starts from the individual grit interaction and then is commonly extrapolated into a whole grinding wheel surface as in models of the conventional grinding process. In the micro-grinding process, the deformation caused by a single grit during its interaction with the

workpiece is closely related with deformation modes, including micro-machining and ploughing mechanisms. The following sections provide related past studies of (i) models in grinding, (ii) modeling of thermal effects in grinding, and (iii) wheel characterization of micro-grinding wheel.

2.2.1 Modeling in the grinding process

In micro and macro grinding, abrasive grits, which are hard particles with sharp edges, are bonded to a wheel rotating at high speed to carry out the cutting process. The orientation of individual grits on the grinding wheel surface is random. So conventional grinding has historically been considered a complex manufacturing process. Due to this complexity, most grinding models are based on empirical relations where the main process variables like the cutting depth, velocity ratio and equivalent diameter are driven to an exponent and multiplied by coefficients that are obtained experimentally by curve fitting of experimental data.

Hahn and Linsay [21-24] experimentally addressed various aspects of the grinding process and provided several quantitative relationships in material removal rate, wheel wear, chatter, surface finish, and geometry. In this study, empirical equations were obtained among process parameters. Malkin et al.[25] presented empirical observations of the grinding process and established the equations for most grinding parameters. Shaw [26] summarized the fundamental studies of grinding in his book. Tönshoff et al.[27] reviewed most aspects of the grinding process including wheel topography, chip thickness, grinding energy, temperature, and surface roughness. Most models in this review are established based on experimental data except for the temperature model. In

industry, the empirical model has been extensively used to determine the setup parameters of the machining. However, the exponents and coefficients in empirical models must be adjusted for each different combination of workpiece material, wheel topography, and kinematics of the grinding using time consuming and costly experimental tests. This shows a constraint on the empirical model in predicting the grinding process and drawing optimal solutions for the different grinding configurations.

Due to the random nature of the cutting edges and to poor understanding of the behavior of a material subjected to extreme conditions, there has been motivation to develop a physical model by first modeling the interaction of an individual grit with the workpiece. After construction of the single grit interaction model, the single grit interaction model can be extrapolated into the whole grinding wheel. Past works by Shaw [28], Maan et al.[29], Komanduri [30], and Torrance [31] showed that the interaction between a grit and the workpiece is dominated by high negative rake angle and high strain rate. Figure 2-4 shows two primary mechanisms between previous proposed works. Shaw [28] assumed a spherical grit shape and presented the single grit model to predict the force per grain based on a force equilibrium between the hardness of the material and the indention force acting on a grit. However, this model doesn't cover the effects of process conditions. On the other hand, Komanduri [30] proposed that the single grit interaction is similar to machining with a high negative rake angle. This research showed that there is a stagnation point which is referred as to a minimum chip thickness. While these two mechanisms are practically plausible, they cannot be used in the single grit model for the micro-grinding process because, in the micro-grinding, the single grit undergoes two phenomena: (i) micro-scale indentation, (ii) micro-cutting with the high

negative rake angle and the high strain rate. Thus, in the prediction of the micro-grinding force, two phenomena will be considered in developing the single grain interaction model in the micro-grinding process.

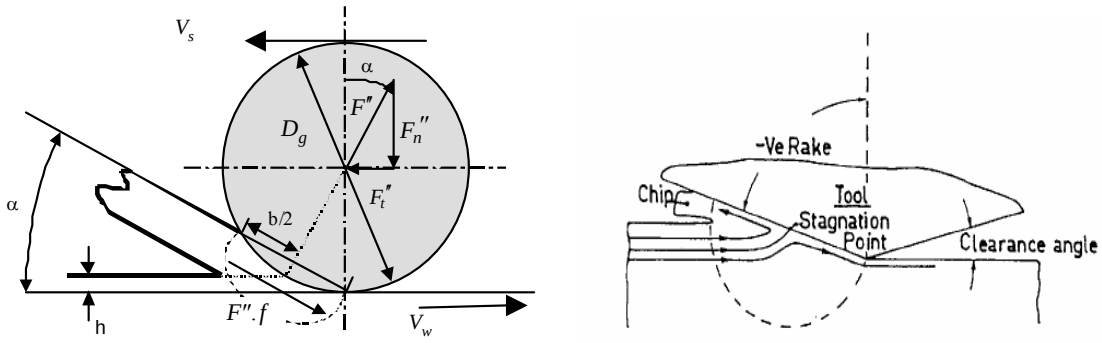

(a) (b)

Figure 2-4: (a) Ductile extrusion ahead of the grit by Shaw[28], (b) Chip formation process with a high negative angle by Komanduri [30]

The other modeling approach is to predict grinding forces based on the slip line method. Challen and Oxley[32] proposed three slip line fields: wave formation, wear, and cutting. This model provides that forces of grit can be obtained as a function of the depth of cut, attack angle of a grit, the hardness of the workpiece, and the shear strength of the lubricant films. William and Xie[33] proposed a three dimensional model of the interaction between a grit and the workpiece and assumed that a single hard pyramid-shape moves on a soft workpiece. These models are relatively simple compared to other models. However, in this model, the workpiece is assumed as a rigid-perfectly plastic material.

2.2.2 Modeling of thermal effects in grinding

In the grinding process, since the energy density in the grinding zone is high compared to traditional machining processes such as turning, milling, planning, and broaching, the thermally induced stress to the workpiece is an important parameter on the workpiece property. There are many efforts devoted to modeling the thermal effects in the grinding process using various techniques such as analytical and experimental methods. These works seek to understand the heat partition in grinding and to predict the temperature as well as its influence on surface integrity.

In most theoretical modeling of thermal effects, a moving heating source analysis by Jaeger[34] was used to predict the temperature in grinding. In that model, the grinding zone is assumed as a band source of heat that moves along the surface of the workpiece at the workpiece feedrate, and the temperature rise was driven in direction of movement of the heat source and the depth into the workpiece.

At the early stage, Outwater and Shaw[35] suggested that the possible sources of heat generation are as follows:(i) heat, (ii) kinetic energy of the chips, (iii) surface energy needed to form new surfaces, and (iv) potential energy residing in the workpiece and the chips. They indicated that most grinding energy is transformed into heat and other energies can be negligible. They presented a model of heat transfer to the workpiece based on a sliding heat source at the shear plane; this is the shear plane partitioning model. Hahn [36] proposed a sliding model for the heat partition ratio between the workpiece and the wheel in grinding, in which the primary heat source is the grit and workpiece rubbing surfaces. This study more accurately described heat generation by considering

the forces at the contact between the grit and the workpiece and ignoring the forces in the shear plane. Makin[37] summarized the results of earlier researches and Makin and Anderson [38, 39] proposed a model of the grinding zone temperature and the temperature at the surface as a sum of a local temperature generated by grinding of an individual grit and considered the frictional heating at the wear flat and shear deformation on the shear plane. Ramanath and Shaw[40] showed that the fraction of heat conducted in the workpiece depends on the thermal properties of workpiece and grits. They pointed out that a small portion of the heat generated in grinding is conducted into the workpiece and the grits carry away most of the heat. Tönshoff et al.[27] suggested that the locations of heat generation in grinding are shearing zone, rake face friction, cutting edge, flank friction, and bond and coolant frictions, and they indicated that the flank friction is a important heat source in grinding because most energy generated in grinding is consumed on sliding and plowing. In grinding, their works showed that the frictional energy is very important to model thermal effects and the principal source of heat generation. Therefore, the frictional heat model is suitable to represent the temperature in grinding.

The other approach is to use the finite element method (FEM) to find the surface temperature. Werner et al.[41] adapted finite element analysis(FEA) to model temperature in grinding and showed that the temperature at the workpiece surface decreases with increasing depth of cut. One of their earlier attempts was to model the effect of all four heat sinks. The FEM approach is a very useful way to assess thermal damage in grinding. But it requires considerable computing time and power.

Measuring temperatures in grinding is a challenging problem because in a short time period, there are multiple contacts between grits and the workpiece through the

grinding zone. Experimental techniques used in grinding experiments can be classified into three: (i) an embedded thermocouple and (ii) an embedded infrared detector using a fiber optic linked to a two color pyrometer. A thermocouple was first used to measure the temperature in grinding and is still used at this time. The other technique is an infrared method to measure the flash temperature. Although this method shows good capability to measure the grain temperature, this method can be applicable when the fluid exists in grinding. So, the thermocouple method is more suitable in micro-grinding experiments and to improve the response time of this thermocouple, a smaller size for the thermocouple is desired.

Xu and Malkin[42] compared three different methods such as the thermocouple method and the infrared method by measuring the temperature of grinding AISI 1010 steel using a Cubic Boron Nitride (CBN) abrasive particle. All three methods provided comparable temperature responses, which were consistent with analytical predictions from a moving heat source analysis.

In thermal modeling, the heat partition ratio that is the fraction of the heat flux that is transferred into the workpiece is an important factor[36, 43]. The estimation of the heat partition is still the challenging problem. Experiments to determine the heat partition ratio to the workpiece are generally based on the above techniques and temperature matching by Kohil et al.[44]or inverse heat transfer techniques are used to find the heat partition ratio. Generally, since the inverse heat transfer technique is not plausible, temperature matching method is used in calibrating thermal models.

In the temperature matching method, data input to the workpiece were obtained by measuring the temperature profile in the workpiece using an embedded thermocouple technique and matching the results with analytically computed values.

2.2.3 Characterization of grinding wheel topography

The complexity of the grinding process comes from the grinding wheel, which contains various abrasive particles. These grits are randomly distributed on the grinding wheel surface. So there is significant variation of the process due to this randomness. But information regarding the density, size, and shape of these grits is not given by the wheel specifications. Identification of the topography of a grinding wheel provides a good reliability to predict the overall grinding forces because the total grinding forces highly depend on the total number of the grits engaged in grinding. The number of active grits depends not only on the static density of the cutting edges but also on the kinematics of grinding.

König et al.[45] combined the number of active cutting edges with the dynamic chip thickness as well as the shape and angle of the cutting edges. They showed that all static cutting edges within a contact zone are not engaged in grinding.

Verkerk et al.[46] reviewed different methods to measure the static and dynamic density of grits such as the taper print, piezoelectric sensors, and stylus method. Their studies proposed the common ground of two different parameters in grinding such as the static and dynamic density of cutting edges. It was found that the experiments of measuring the dynamic density of grits are complicated because the distinction between

cutting and plowing mechanisms is not clear. Generally, the static density of cutting edges is obtained from direct measurements. But, the dynamic density of cutting edges is determined from experimental data with the analytical approach considering the kinematics of cutting edges.

Younis et al. [47] showed that the percentage of the dynamic cutting edges to the static cutting edges is 2% to 12%.

Characterization of the grinding wheel is a crucial factor to allow better prediction of a grinding process. Various techniques have been developed to get better information about grinding wheel topography. The main techniques for grinding wheel topography are

- Stylus methods
- Replication methods
- Microscopic methods

The principle of the stylus method is similar to that used for the surface roughness measurement. A stylus with the small spherical tip is dragged over the wheel surface to measure the profile of the grinding wheel surface. A two-dimensional profile of the grinding wheel surface is obtained from this method. The experimental results can be used as an input to predict the grinding process.

But there are drawbacks to this method. First, the accuracy of the method really depends on the shape and size of the stylus tip. There is also the wear of the stylus due to a continued contact between hard abrasive particles and the stylus tip. König et al.[48] presented new techniques to obtain a three-dimensional image of a grinding wheel surface by scanning the wheel in the transversal and circumferential directions.

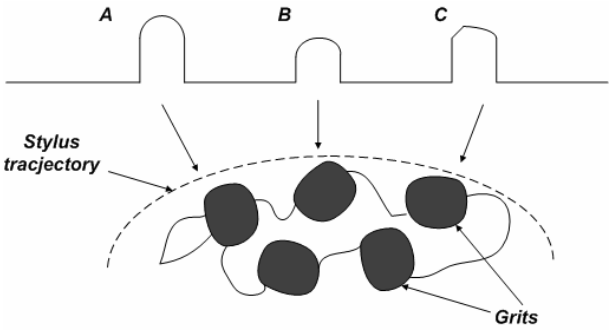

Figure 2-5: A stylus trace of a grinding wheel surface

The replication method includes replicating or imprinting the wheel surface on soft metal and this is not a measurement technique. The technique has been widely used because there is a difficulty in directly measuring the static and dynamic density of the grinding wheel. The replicas generated in this way can be measured by stylus, optical, and microscope techniques. Previously, water based plastic system and epoxy resin system were used and showed capability to replicate surface structure with low shrinkage. Brough et al.[49] pressed a soft polished lead into the grinding wheel to the depth of the active layer. While making a replica, depths of penetration into the lead and forces applied on the grit have to be carefully controlled by applying proper pressure and time. Lead has a low resistance compared to other materials so that it is likely to minimize damage to grinding wheel topography. Recently, Cai [50] used a two-part synthetic rubber compound known as Microset 101. Although it is very soft compared to lead, this material provides a high resolution (~0.1μm) and high contrast characteristics for optical methods.

Microscopic methods are based on an optical microscope and a scanning electron microscope (SEM) to get the topographic information of the grinding wheel. A stereo

microscope using a built-in vertical illuminator is relatively inexpensive and invaluable. This microscope provides fine details of the surface using a large magnification. But at low magnifications, sometimes, it is hard to distinguish between grits and bonds.

SEM provides detailed and clear information about the grinding wheel surface with high magnifications. The problems of this microscope are that sections of a wheel have to be small enough to fit to the observation area and the size of SEM chamber and that the replication materials tend to melt during experiments.

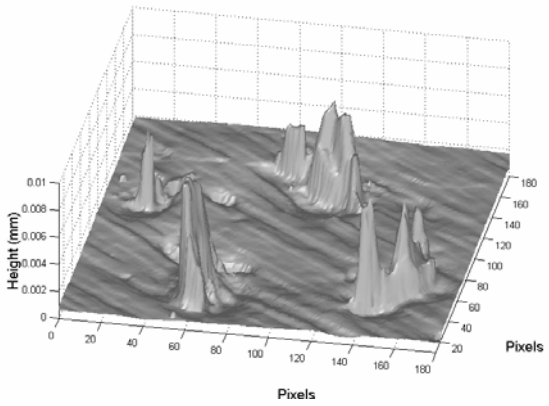

Figure 2-6: Image of the wheel topography by interferometer[51]

Currently, an optical interferometer provides quantitative characterization of a grinding wheel according to depths of cut. This equipment can produce a three-dimensional image of a grinding wheel. These techniques have to be supplemented by an image processing program such as Matlab for the analysis of the wheel topography.

2.3 Micromachining process

The micro-grinding process shares some aspects with mechanical machining at the microscale in view of the single grit interaction. Machining is a well established

material removal process for fabricating three dimensional macroscale components. As the demand for fabrication of microscale components increases, mechanical machining at the microscale, more commonly referred to as micromachining, is an emerging technology because it can produce intricate three dimensional features which satisfy stringent dimensional tolerance and high surface finish requirements. However, there are still numerous challenges to address in order for micro-cutting to be economically viable and reliable for fabricating microscale components.

Currently, there have been numerous studies of tool life, edge radius effect, surface generation, size-effect in the specific cutting energy, minimum chip thickness, micro-structural effects as well as finite element modeling and molecular dynamics simulation of microscale cutting. However, there is no fundamental understanding and general consensus on the mechanism that dominates mechanical machining at the microscale. Specifically, there is no basic understanding of the size effect in specific cutting energy in micromachining and there is no knowledge of how these process responses differ from those in macro-scale cutting.

2.3.1 Size effect in micromachining

In these studies of micro-cutting forces, the specific energy in machining, which is required to remove a unit volume of metal, is typically found to increase at small values of the undeformed chip thickness. This increase is associated with an increase in the specific cutting force with decreasing chip thickness, which phenomenon has been termed the size effect. On the basis of previous findings, Subbiah and Melkote[52] summarized possible contributors for the size effect. These contributors are tool edge

radius effects, sub-surface plastic deformation, material strengthening effects, and material separation effects.

Shaw[53] and Backer et al.[54] attributed the size effect in shear energy per unit volume to strain hardening and the short range inhomogeneity in metals, which is related with a dislocation theory. Based on this theory, material strength in plastic deformation of metals is determined by the motion of dislocation and their interactions. Nakayama[55] attributed the size effect to the decrease of the shear angle due to the finite edge radius of the tool and to greater energy dissipation which is related with sub-surface plastic deformation of the workpiece. Atkins[56] attributed the size effect to the material separation effect which is related with the energy required to create new surfaces via ductile fracture.

Beside the above explanations, Masuko et al.[57] attributed the size effect to an extra force required to penetrate the workpiece, which is related to an indentation force due to ploughing before chip formation. Albrecht[58] suggested that the plough force is a contributor to the size effect. The reason is that at small depths of cut, the ploughing force contributes a greater proportion of the total cutting force.

Recent works by Dinesh et al.[59] and Joshi and Melkote[60] have suggested the likelihood of strain gradient plasticity effects at the shear plane leading to the size effect in machining. This phenomenon refers to an increase in yield stress of a material with increasing strain gradient. Kai and Melkote[61] developed the FE model of orthogonal cutting incorporating strain gradient effects. There is still no general consensus and definitive explanation established for the size effect phenomenon. In this study, among

the described effects, the effects of the ploughing force and the tool edge radius are implemented in the model developed.

2.3.2 Crystallographic effects

In micromachining, the cutting depth and feed rate are smaller with respect to conventional machining. So the depth of cut can be smaller at machining polycrystalline materials than the average grain size. During micromachining, the tool works intra-crystalline and it cuts through grain boundaries, which is related with the grain size of materials. In both cases, the crystallographic orientation and size have important effects on the micromachining processes.

In micromachining, Moriwaki[62] showed that the fundamental mechanism of the cutting process is affected by the material properties and microstructure of the material. In micromachining single crystal materials, the specific orientation of the materials with respect to the cutting direction will be important. On the other hand, in the case of polycrystalline materials, the machining mechanism highly depends on individual grains and crystallographic orientations in Figure 2-7.

Ueda and Iwata [63] showed that the cutting behavior and the pattern of chip formation in the single crystal is largely affected by the cutting direction with respect to the crystallographic orientation. They used the direct scanning electron microscope observation of in-situ chip formation as an experimental technique. Sato et al.[64] conducted an orthogonal cutting using a high precision machine to study the characteristic phenomena in aluminum single crystals. Their experiments showed that

surface finish, chip topology, and cutting force significantly vary during micromachining of single crystal aluminum.

In the case of polycrystalline materials, Turkovich et al.[65] found that the principal shear action becomes dominant in the case in which the lamellae align to the cutting direction; they found further that the thickness of the chip depends on the crystallographic orientation.

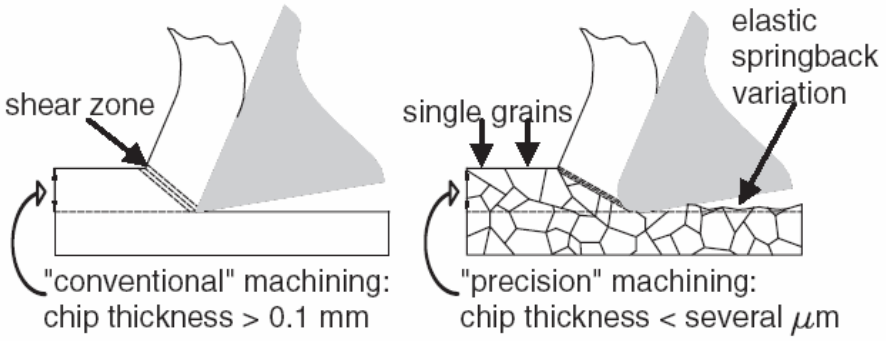

Figure 2-7: Comparison between conventional and micromachining processes[62]

Furukawa and Moronuki [66] showed that the cutting mechanism are very different for polycrystalline, single crystal or amorphous material. They found that cutting forces varied as the tools passed grain boundaries in Figure 2-8(a).

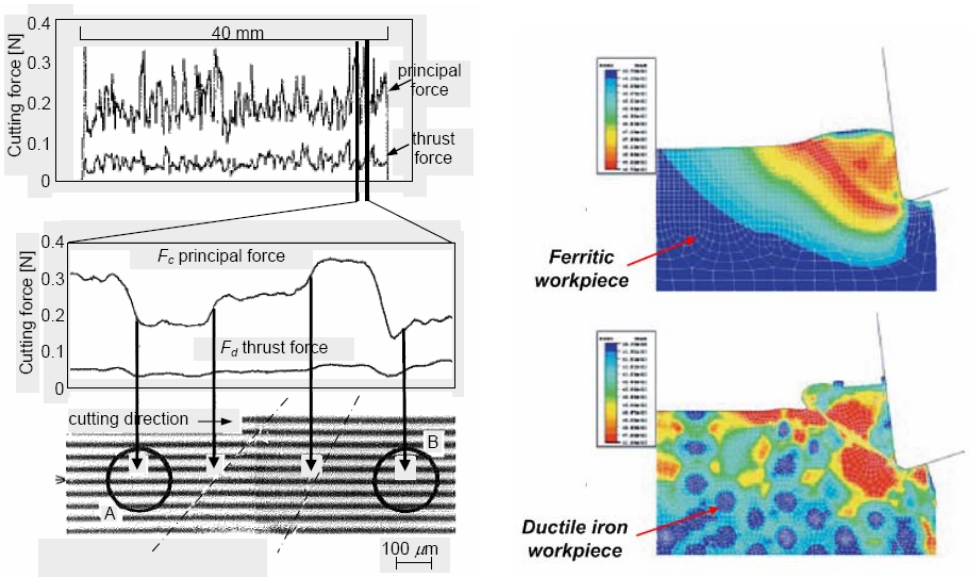

(a) (b)

Figure 2-8: (a) Variation of cutting forces corresponding with the grain boundary of Al alloy [66]and (b) FE model of heterogeneous materials[67]

Recent works by Chuzhoy[67, 68] studied the influence of microstructure effects in micromachining. They developed a finite element (FE) model for simulation of heterogeneous materials. They found that the variation of simulated forced in micromachining the multiphase materials is larger than that in micromachining a single phase material in Figure 2-8(b)

2.4 Summary

Based on literature reviews relating to micro-grinding and micro-machine tools, a little knowledge of micro-grinding and design of microscale machine tools has been accumulated in this emerging field. So, there is a need to develop an analytical model of micro-grinding including the kinematics of micro-grinding, and workpiece properties. Specially, development of the single grit interaction model including the size effect has to

be performed. On the other hand, as the shapes of miniaturized machine tools have become more complex, optimization of the structure of microscale machine tools is needed on the basis of mathematical models of key parameters such as volumetric error, machine working space, and static, thermal, and dynamic stiffness.

These research directions are to fill these gaps outlined in this review of prior works.

CHAPTER 3

MODELING OF MICRO-GRINDING FORCES AND THERMAL EFFECTS

3.1 Introduction

Grinding has been widely used to produce high quality parts. But, due to the approximate size of conventional grinding wheels, conventional grinding is limited to machining simple parts. So, grinding with the microscale grinding wheel, which is referred to as micro-grinding in this dissertation, is a good candidate for producing high quality parts at the micro domain by Feng et al.[69]. In micro-grinding, the single interaction between the grit and a workpiece is more important because the micro-grinding process is the cumulative outputs of numerous single grit interactions. So modeling the single grit interaction is important for the predictions of process variables.

This chapter describes in detail the single grit interaction model for micro-grinding. There are two major interactions in the grinding process: mechanical and thermal interactions. The model for mechanical interaction between the workpiece and an individual grit on the micro-grinding wheel is discussed in this chapter, considering both micro-cutting and ploughing mechanisms along with associated friction effects at the contact interface. Next, in order to estimate thermal effects in a micro-grinding process, a thermal model is presented, which considers a moving heat source on the micro-grinding zone under given machining conditions.

In addition, the ratio of heat partition into the workpiece in micro-grinding is calculated by matching experimental data using embedded thermocouple measurement to

analytical calculations. The following sections described the models developed and used to calculate forces per grit.

3.2 Modeling the single grit interaction in micro-grinding

In this section, the micro-grinding process is defined as grinding with the ratio of the depth of cut to the grit radius smaller than 1. Further, in micro-grinding, the ratio of a grit size to the grinding wheel increases compared to the conventional grinding process. So, the analytical model of the individual grit interaction is the critical factor to use in predictions about the micro-grinding process. This single grit interaction can be characterized by micro-cutting with a high negative angle at a high strain rate. The size effect is applied through the coupling of micro-cutting and ploughing mechanisms with associated friction effects within the single grit interaction for the micro-grinding process. In this study, the deformation of a workpiece subjected to micro-grinding is assumed as pseudo orthogonal machining by considering microchips as a series of elements of infinitesimal width and assuming no heat loss along primary and secondary heat zones. In the following sections, the physical models for the microchip formation and the ploughing mechanisms are independently presented.

3.2.1 Modeling of Chip Formation Forces in individual grits

Since the geometry of grits is random with other aspects in grinding, the grit shape has to be approximated by a specific geometry to simplify the mathematical

modeling of the individual grit interaction. Modeling this interaction starts from simplified geometries such as pyramidal, conical, spherical shapes. Gilormini et al.[70] approximated the abrasive grit as idealized pyramidal indenters and Shaw[28] modeled abrasive grits as a spherical shape. In this study, the abrasive grit shape on the wheel surface is assumed to be a spherical shape.

Based on the above described assumptions, a mathematical framework for the individual grit interaction in micro-grinding starts by assuming the two dimensional process involving the phenomena of micro-cutting and ploughing. Basuray et al.[71] related the transition point from the ploughing to microchip formation to a critical rake angle on the basis of the slip line model.

In micromachining, there are two important rake angles: (i) a negative rake angle (α_s) which changes according to varying depth of cut, (ii) a critical rake angle (α_{cr}) which is the transition point from the micro-cutting and ploughing in Figure 3-1.

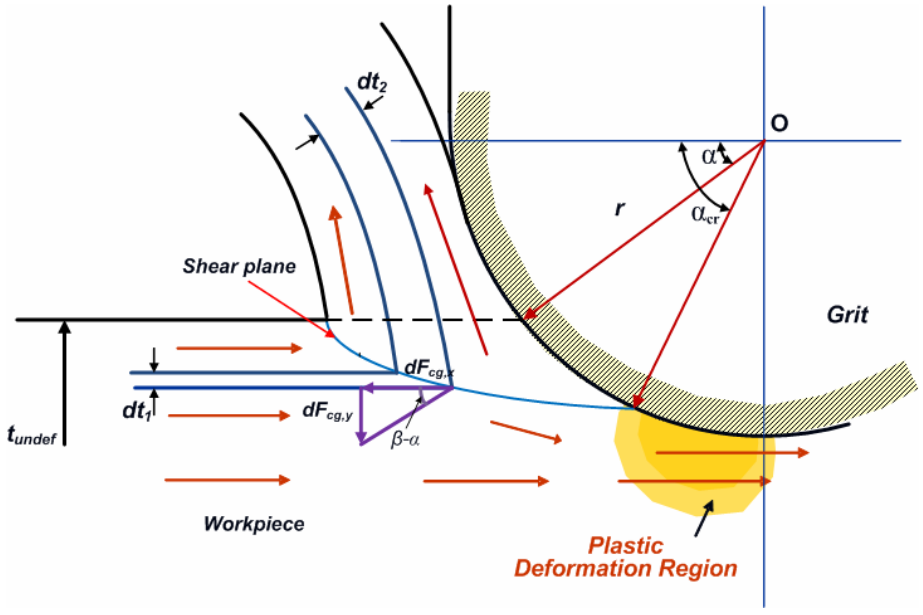

Figure 3-1: A mechanical interaction of the single grit in micro-grinding

The critical rake angle is the rake angle below which a workpiece material is deformed by the ploughing effect. On the basis of the geometry relationship, the critical rake angle can be determined by the minimum undeformed chip thickness and the cutting edge radius according to the following:

$$\alpha_{cr} = \sin^{-1}\left(\frac{r - t_m}{r}\right) \tag{3.1}$$

where r is the cutting edge radius, t_m is the minimum undeformed chip thickness, and α_{cr} is the critical rake angle

In the case of previous findings[71, 72], Ikawa et al.[72] showed that the minimum undeformed chip thickness strongly depends on the sharpness of the cutting edges. They suggested that the minimum undeformed chip thickness may be at the order of 1/10 of the cutting edge radius. Based on the slip line analysis, Basuray et al.[71] predicted that a stagnation point is constant and equal to 37.6˚ which is close to 2/10 of the cutting edge radius. These results provide the approximate location of the stagnation point. In this study, the minimum undeformed chip thickness is assumed to be between 0.1-0.2 of the cutting edge radius.

In the micromachining regime, the micro-cutting mechanism above the minimum uncut chip thickness can be represented by applying the Merchant model to each of the infinitesimal elements; this model is adapted from Liu[73] and Son et al.[74]. Considering an element of undeformed chip thickness, dt_1, being cut at a position corresponding to the associated local rake angle, a pair of chip formation and thrust

forces can be related with the friction and rake angles. The relationship between these can be given as:

$$dF_{cg,y} = dF_{cg,x} \tan(\beta_i - \alpha_i) \tag{3.2}$$

Hence, the incremental cutting and thrust forces per unit width in the two dimensional simplified configuration can be expressed as follows:

$$dF_{cg,x} = -\frac{\tau_s \cos(\beta_i - \alpha_i)}{\sin\phi_i \cos(\phi_i + \beta_i - \alpha_i)} dt_1 \tag{3.3}$$

$$dF_{cg,y} = -\frac{\tau_s \sin(\beta_i - \alpha_i)}{\sin\phi_i \cos(\phi_i + \beta_i - \alpha_i)} dt_1 \tag{3.4}$$

where τ is shear strength of the material, β_i is the instantaneous friction angle, α_i is the instantaneous rake angle, and ϕ_i is the shear angle.

In micro-grinding, the effective rake angle (α_s) is negative in the case in which the undeformed chip thickness is below the cutting edge radius. The instantaneous rake angle is obtained from a geometrical relationship like the following:

$$\alpha_s = \sin^{-1}\frac{(r - t_0)}{r} \tag{3.5}$$

where r is the cutting radius and t_0 is the undeformed chip thickness

In micro-grinding, as the spherically shaped grit moves horizontally, the front half of the hemisphere is involved in the material removal process. The chip formation forces in micro-cutting can be obtained by multiplying the projected area of the contacting surface as shown in Figure 3-2.

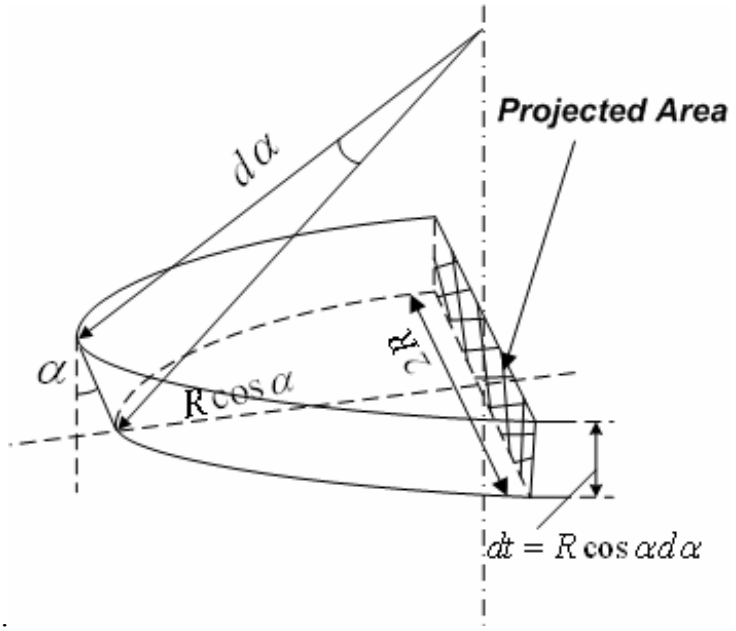

Figure 3-2: Illustration of the geometric configuration on the spherical shape grit

The cross section area of an ideal spherical shape grit between the increment of the depth of cut and rake angle is

$$dA_i = 2r^2 \cos^2 \alpha_i d\alpha_i \tag{3.6}$$

The total cutting and thrust forces per each grit are obtained by integrating the Equations (3.3)and(3.4). Finally, the expressions of the overall normal ($F_{cg,y}$) and tangential forces ($F_{cg,x}$) per each grit are

$$F_{cg,x} = \int_{\alpha_{cr}}^{\sin^{-1}\frac{(r-t_0)}{r}} \frac{\tau_s \cos(\beta_i - \alpha_i)}{\sin\phi_i \cos(\phi_i + \beta_i - \alpha_i)} 2r^2 \cos^2 \alpha_i d\alpha \tag{3.7}$$

$$F_{cg,y} = \int_{\alpha_{cr}}^{\sin^{-1}\frac{(r-t_0)}{r}} \frac{\tau_s \sin(\beta_i - \alpha_i)}{\sin\phi_i \cos(\phi_i + \beta_i - \alpha_i)} 2r^2 \cos^2 \alpha_i d\alpha \tag{3.8}$$

In the above equations, the shear stress is calculated on the basis of the material model to be discussed in Session 3.3.

3.2.2 Prediction of the ploughing Force

The workpiece material below the minimum undeformed chip thickness undergoes a different phenomenon in the micro-grinding process. At this region, the workpiece is plastically deformed in the front of the grit without chip formation. This plastic deformation of the material is referred to as ploughing and is similar to the plastic deformation of the material in a spherical indentation process. Both Albrecht[58] and Masuko[75] have attributed the size effect in micro-cutting to the ploughing process.

Shaw[28] adapted a Brinell indentation hardness test to describe the single grit interaction because the behavior of material beneath a Brinell ball resembles the material deformation below a grit. So, the stress in the plough region can be associated with the Brinell hardness test. In the Brinell test, the spherical tip is pressed against the workpiece surface, which creates the plastic deformation zone similar to the stresses at the rounded tool and workpiece interface in Figure 3-3.

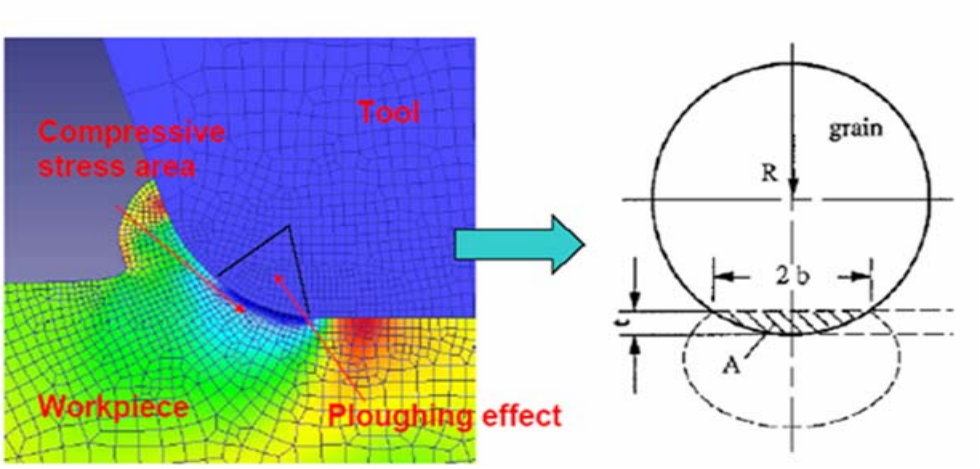

Figure 3-3: Simplification of the plough effects into a spherical indentation

The Brinell hardness number (HB) is defined as the ratio of the load ($F_{brinell}$) to the curved area of indentation as the following:

$$HB = \frac{2F_{brinell}}{\pi D\left(D - \sqrt{D^2 - b^2}\right)} \tag{3.9}$$

where HB is the Brinell hardness number, $F_{brinell}$ is the indentation force, D is the ball diameter, and b is the diameter of the impression

In this analysis, the indentation force acting in the direction of α_{cr} with respect to the normal direction is attributed to the ploughing force. The relative movement also generates friction between the grit and the workpiece. The tangential and normal ploughing forces per grit can be estimated by combining the indentation effect with the friction reaction as follows:

$$F_{pg,y} = F_{brinell}(\sin\alpha + \mu_p \cos\alpha) \tag{3.10}$$

$$F_{pg,x} = F_{brinell}(\cos\alpha - \mu_p \sin\alpha) \tag{3.11}$$

where μ_p is the ploughing friction coefficient

At very low depths of cut, the coefficient of friction is highly influenced by the ratio of the depth of indentation to the tool nose radius. Sin and Suh [76] extended the predictive model of Goddard and Wilman [77] to estimate adhesion and ploughing friction coefficients in a simple groove experiment under given conditions.

Assuming that the adhesion effect is negligible in the small depth of cut, the ploughing mechanism in the individual grit interaction resembles the simple groove experiment. Hence, in the ploughing region of a sliding spherical hard particle in Figure 3-4, the friction coefficient can be estimated by the following equation:

$$\mu_p = \frac{2}{\pi}\left[\left(\frac{w}{2r}\right)^{-2}\sin^{-1}\left(\frac{w}{2r}\right) - \left\{\left(\frac{w}{2r}\right)^{-2} - 1\right\}^{\frac{1}{2}}\right] \tag{3.12}$$

where w is the width of indentation and r is the spherical grit radius.

Bhushan [78] proposed the ploughing friction model in sliding cylinder. The model is

$$\mu_p = \left[\frac{1}{2(r/t_0) - 1}\right]^{1/2} \tag{3.13}$$

where r is the cylinder radius and t_0 is the depth of cut

In both models, the ratio of the depth of cut of the radius has influenced a coefficient of ploughing friction, which is shown in Figure 3-4(b). But, the effect of pile-up of material ahead of the sliding sphere and cylinder is not involved in both cases.

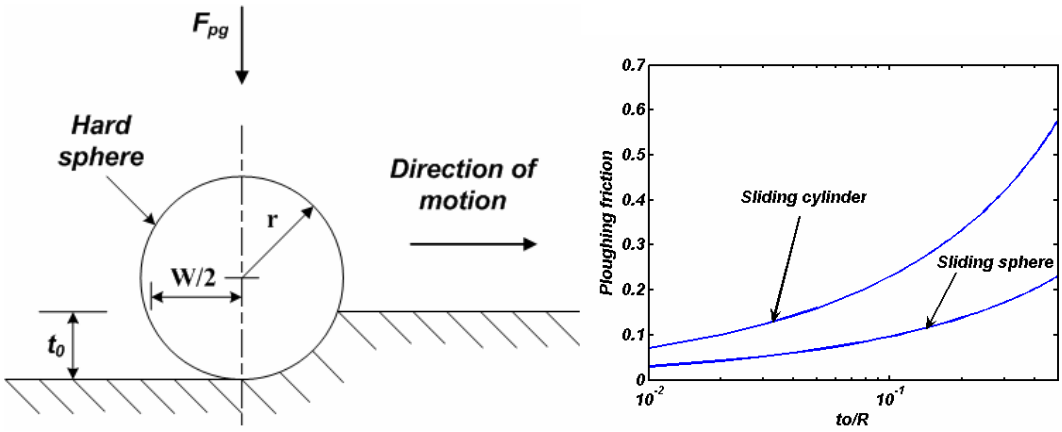

(a) (b)

Figure 3-4: (a) Schematic of hard sphere sliding on a softer material and (b) Ploughing friction coefficient as a function of the ratio of the depth of cut to the tool nose radius

3.2.3 Shear angle in the single grit interaction

The shear angle has a great influence in predicting the machining process because it determines the geometry of the primary deformation in machining. The mathematical models in Equations (3.7) and (3.8) have to be accompanied with the knowledge of the shear angle.

Traditionally, the shear angle solution from the Ernst and Merchant model[79] has been widely used though the model is based on the assumption that the direction of shear coincides with the direction of maximum shearing stress. Expression of the Ernst and Merchant model is given by

$$\phi = \frac{\pi}{4} - \frac{1}{2}(\beta - \alpha) \tag{3.14}$$

Consequently, many attempts have been made to predict the relationship between the shear, friction, and rake angles and these have confirmed the linear relationship among these parameters. However, in dealing with the negative rake angle in the single

grit interaction of micro-grinding, there is no basic understanding of the quantitative relationship for materials.

In this study, FEM is used to capture trends in relationship between ϕ and β-α and the contribution of main parameters. The FE model is based on an updated Lagrangian formulation and performed using DEFORM 2D. The results of the FEM simulations show a linear trend with the Ernst and Merchant model. But, the coefficient representing the slope in Equation (3.15) is less than that of the Ernst and Merchant model.

$$\phi = 35.218 - 0.213(\beta - \alpha) \tag{3.15}$$

But, the values of the shear angle obtained as a result of the FEM simulations change according to the advanced FEM software used [80]. A sensitivity analysis of simulation parameters has been performed. The parameters chosen in analysis are rake angle, depth of cut, friction coefficient, and cutting speed. This analysis shows that the shear angle is highly influenced by the rake angle among other parameters in Therefore, the shear angle changes locally corresponding to the rake angle, so that at low depth of cut, the shape of a shear plane is a curved line compared to a classical shear plane.

So, based on the assumption that the shear plane orients to ensure minimum energy consumption in machining, the Ernst and Merchant model can be adopted. The overall forces per grit can be obtained by integrating with the stipulation that the shear angle follows Equation(3.14).

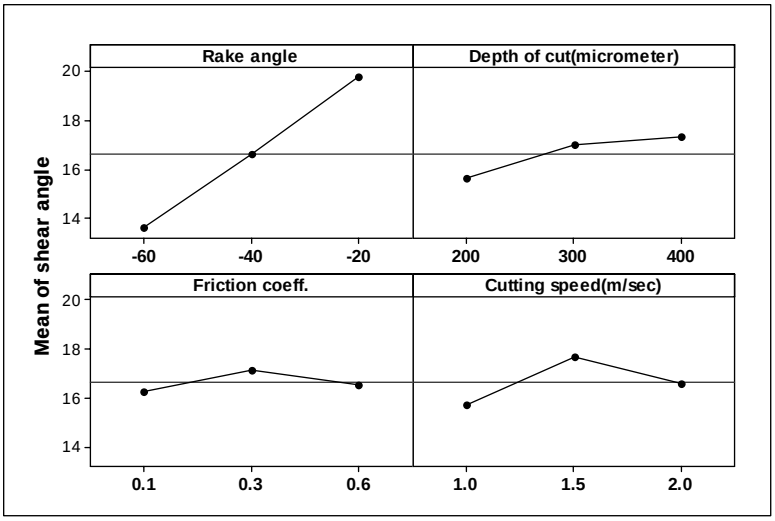

Figure 3-5: Main effects plot for the shear angle predictions

Substituting the Ernst and Merchant model in Equations (3.7)and(3.8), the mathematical models of chip formation forces are given by

$$F_{cg,x} = \int_{\alpha_{cr}}^{\sin^{-1}\frac{(r-t_0)}{r}} \frac{\tau_s \cos(\beta_i - \alpha_i)}{\sin\left(\pi/4 - (\beta_i - \alpha_i)/2\right)\cos\left(\pi/4 + (\beta_i - \alpha_i)/2\right)} 2r^2 \cos^2 \alpha_i d\alpha \qquad (3.16)$$

$$F_{cg,y} = \int_{\alpha_{cr}}^{\sin^{-1}\frac{(r-t_0)}{r}} \frac{\tau_s \sin(\beta_i - \alpha_i)}{\sin\left(\pi/4 - (\beta_i - \alpha_i)/2\right)\cos\left(\pi/4 + (\beta_i - \alpha_i)/2\right)} 2r^2 \cos^2 \alpha_i d\alpha \qquad (3.17)$$

3.3 Material model in micro-grinding

3.3.1 Material model of conventional flow stress

In this study, due to the nature of the micro-grinding process, the workpiece in this process is subjected to deformation at high strains and strain rates. In order to incorporate temperature, strain, and strain rate effects, the Johnson-Cook model[81] is

adopted to represent the material deformation behavior on the shear plane, which is given by

$$\sigma = \left(A + B\varepsilon^{n}\right)\left(1 + C\ln\frac{\dot{\varepsilon}}{\dot{\varepsilon}_0}\right)\left(1 - \left(\frac{T - T_0}{T_m - T_0}\right)^{m}\right) \tag{3.18}$$

where σ is the material flow stress, $\dot{\varepsilon}$ is equivalent strain, T_m is the melting temperature, T_0 is the environment temperature, A,B,C, m, and n are material constants.

Based on the above equation, the shear stress in Equations (3.16) and (3.17) can be obtained as

$$\tau_s = \frac{1}{\sqrt{3}}\left(A + B\varepsilon^{n}\right)\left(1 + C\ln\frac{\dot{\varepsilon}}{\dot{\varepsilon}_0}\right)\left(1 - \left(\frac{T - T_0}{T_m - T_0}\right)^{m}\right) \tag{3.19}$$

In the calculation of strain and strain rate, there are two possible methods: (1) the Oxley's model[82] with the assumption that the tool is perfectly sharp and (2) the Manjunathaiah and Endres model[83]. In the Oxley's model, the strain along a shear plane is given by

$$\varepsilon = \frac{1}{2\sqrt{3}}\frac{\cos\alpha_n}{\cos(\phi_n - \alpha_n)\sin\phi_n} \tag{3.20}$$

where ϕ_n is the nominal shear angle and α_n is the nominal rake angle

The strain rate along a shear plane is given by

$$\dot{\varepsilon} = \frac{C_{oxley}}{\sqrt{3}}\frac{V_{sh}}{l_s} \tag{3.21}$$

where C_{oxley} is constant, V_{sh} is the shear velocity, and l_s the length of a shear plane.

In Equation(3.21), the shear velocity of a shear plane is given by

$$V_{sh} = V_s \frac{\cos \alpha_n}{\cos\left(\phi_n + \alpha_n\right)} \tag{3.22}$$

In the case of the length of shear plane, since the shear plane is created above the minimum undeformed chip thickness, the length of the shear plane is obtained by

$$l_s = \frac{t_0 - t_m}{\sin \phi_n} \tag{3.23}$$

Recent work by Manjunathaiah and Endres[83] proposed a new strain and strain rate model based on the geometrical relationship and the slip line analysis in Figure 3-6(a). This method provides the strain and strain rate effect in machining with an edge-rounded tool, which is similar to the case in the micromachining process.

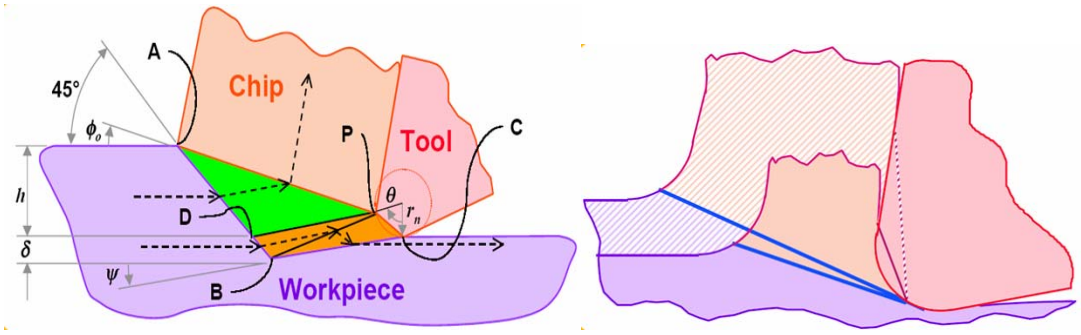

(a) (b)

Figure 3-6: (a)Geometry model (b) process variation according different depths of cut by Manjunathaiah and Endres[83]

In this model, the effective strain is obtained from weighing the shear strains: (i) the stain of the chip (γ_{chip}) and (ii) the strain of the workpiece (γ_{work}) corresponding to the volume ratios of the chip (υ_{chip}) and workpiece (υ_{work}) deformations

$$\varepsilon = \frac{1}{\sqrt{3}}\left(\frac{\upsilon_{chip}\gamma_{chip}}{\upsilon_{chip}+\upsilon_{work}} + \frac{\upsilon_{work}\gamma_{work}}{\upsilon_{chip}+\upsilon_{work}} \right) \tag{3.24}$$

The shear strains of the chip and workpiece are given by

$$\gamma_{chip} = \frac{\sqrt{2}\sin\theta_{PD}}{\sin(\pi/4+\theta_{PD})} + \frac{\cos(\gamma_{avg}+\theta_{PD})}{\cos(\gamma_{avg}-\phi)\sin(\phi+\theta_{PD})} \tag{3.25}$$

$$\gamma_{work} = \frac{\sqrt{2}\sin\theta_{PD}}{\sin(\pi/4+\theta_{PD})} + \frac{\sin\left(\theta_{PD}+\theta/2\right)}{\sin(\theta_{PD}+\pi/2)\sin(\theta_{PD}+\theta_{PB})} + \frac{\sin\theta/2}{\sin(\psi)\sin(\psi+\theta/2)} \tag{3.26}$$

where ψ is the inclination of BC in Figure 3-6.

In the model, the strain rate is computed across the entire deformation zone ABCP which includes the chip and workpiece deformation zone. The strain rate of materials is obtained from the method to obtain the shear strain as follows:

$$\dot{\varepsilon} = \frac{1}{\sqrt{3}}\left(\frac{\upsilon_{chip}\dot{\gamma}_{chip}}{\upsilon_{chip}+\upsilon_{work}} + \frac{\upsilon_{work}\dot{\gamma}_{work}}{\upsilon_{chip}+\upsilon_{work}} \right) \tag{3.27}$$

The strain rates of the chip and workpiece deformation are given by

$$\dot{\gamma}_{chip} = 2V_s \frac{\gamma_{chip}}{\sqrt{2}\sin(\pi/4+\theta_{PD})\overline{PD}} \tag{3.28}$$

$$\dot{\gamma}_{work} = 2V_s \frac{\gamma_{work}}{\sqrt{2}\sin(\pi/4+\theta_{PD})\overline{PD} + \dfrac{\sin(\psi+\theta/2)}{\sin\psi}\overline{PC}} \tag{3.29}$$

The drawback of this model is that information about the chip ratio is necessary to calculate the strain and strain rate. In this study, two methods are adopted to compute the strain and strain rate along the shear plane in predictions of forces.

3.3.2 Material model considering the crystallographic effects

The depth of cut in micro-grinding is less than the size of a grain in the material. So the crystallographic effects have to be considered in a material model for prediction. The effects include grain size and orientation effects. The frame on this research work is to analytically represent these microstructure effects by assuming a linear additive contribution of incidental dislocation boundaries and geometrical dislocation boundaries.

Huges et al.[84] proposed a material model to represent the effect of dislocations influencing the macroscopic flow stress. The dislocation boundaries can be divided into two types: geometrically necessary boundaries (GNB) and incident dislocation boundaries (IDB). The flow model proposed consists of three parts:(i) conventional flow stress (ii) the flow stress by IDB (iii) the flow stress by GNB

This model incorporates the strength contribution of the IDB which can be expressed as

$$\sigma_{IDB} = M \alpha_{cont} G b_{bg} \sqrt{\rho_t} \tag{3.30}$$

where M is the Taylor factor, α_{cont} is the material constant, G is the shear modulus of material, b_{bg} is the burger vector of dislocations, and ρ_t is the total density of dislocation

The total density of dislocation consists of the dislocation density in the volumes between boundaries (ρ_0) and the dislocation in the boundary area per unit area (ρ_b), which is

$$\rho_t = \rho_0 + \rho_b \tag{3.31}$$

Based on the assumption that the average grain boundary spacing is equal to the grain size, the total dislocation density can be represented incorporating a microstructure parameter as the following term.

$$\rho_t = \sqrt{\frac{k\theta_{av}}{D_d b_{bg}}} \tag{3.32}$$

So, the flow stress for dislocations in IDB can be given by

$$\sigma_{IDB} = M\alpha_{cont} G b_{bg} \sqrt{\frac{k\theta_{av}}{D_d b_{bg}}} \tag{3.33}$$

Generally, as a strain and stress increase, the misorientation angle in the GNBs increases and becomes a high angle boundary. So recent work by Huges et al.[84] introduced a Hall-Petch equation for high angle boundaries; the flow stress for dislocations in the GNBs can be represented as described in (3.34)

$$\sigma_{GNB} = \frac{K_{HP}}{\sqrt{D_d}} \tag{3.34}$$

The overall flow stress can be described as the sum of these three components of the above equations and can represent the crystallographic effects such as grain orientation and grain size. In this research, the modified material model of micro-grinding is proposed as the following:

$$\sigma = \sigma_i(\varepsilon, \dot{\varepsilon}, T) + \frac{K_{HP}}{\sqrt{D_d}} + M\alpha_{cont} G \sqrt{\frac{kb\theta_{av}}{D_d}} \tag{3.35}$$

The distribution of a grain size and misorientation used in this model is obtained and discussed in Chapter 5.

3.3.3 Material properties of Al 6061-T6

Al 6061-T6 has been widely used in the aerospace industry and is currently used in a wide range of applications as well as its increased usage in microscale dies for other microscale processes. The material constants of the Johnson-Cook model for Al 6061-T6 which are obtained from Keith[85] are listed in Table 3-1.

Table 3-1: Material constants of Johnson-Cook model of Al 6061-T6[85]

Material	A(Mpa)	B(Mpa)	C	M	n
Al 6061-T6	293.4	121.26	0.002	1.34	0.23

Additional material properties used to model mechanical and thermal forces are provided in Table 3-2.

Table 3-2: Material properties of Al 6061-T6

Parameters	Description	Values	References
HB	Hardness Brinell	95	Boyer et al.[86]
k_c	Thermal Conductivity	166.9 W/m-k	Boyer et al.[86]
T_m	Melting Temperature	582 ˚C	Boyer et al.[86]
ν	Poisson Ratio	0.33	Boyer et al.[86]
c	Specific Heat Capacity	0.896 J/g-˚C	Boyer et al.[86]

The key properties of Al 6061-T6 used to compute microstructure effects are summarized in Table 3-3. On the basis of an experimental result[87], the minimum and maximum slopes, K_{HP} of the Hall-Petch relationship for an Al-Mg Alloy are 32.5

$Hv\sqrt{\mu m}$ ($318.7\,Hv\sqrt{\mu m}$)and $52\,Hv\sqrt{\mu m}$ ($510\,Hv\sqrt{\mu m}$), which is shown in Figure 3-7. In this research, the modified material model is used in Equation(3.35).

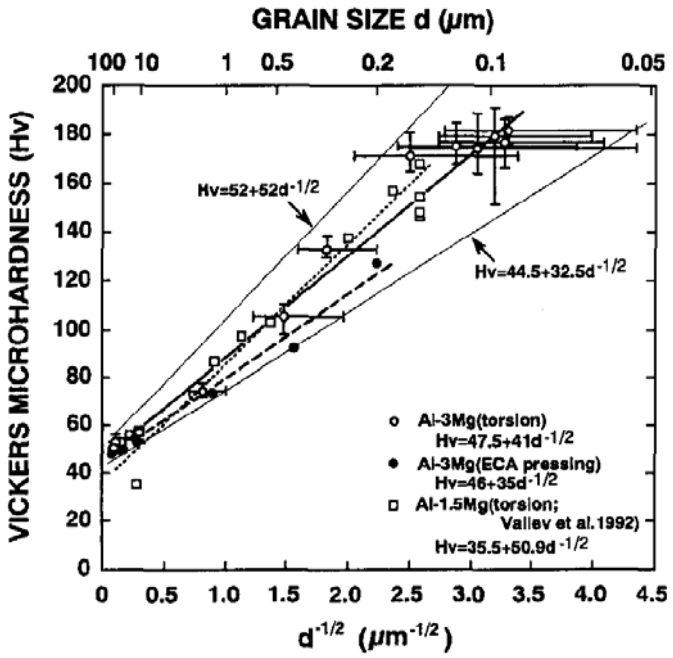

Figure 3-7: Variation in vicker's microhardness with d-1/2 for Al-Mg alloys[87]

Table 3-3: Key properties of microstructure of Al 6061-T6

Parameter	Description	Value	References
b_{bg}	Burger's vector(Pure aluminum)	2.86×10^{-10}m	Totten and Mackenzie[88]
G	Shear Modulus	26Gpa	Boyer et al.[86]
α_{cont}	Material constant	0.2-0.4	Nabarro et al.[89]
M	Taylor Factor	3.1	
k	Constant of the geometry boundary	2-4	Liu et al.[90]
θ_{av}	Average misorientation value	35.13º	Kang et al.[91]
K_{HP}	Hall-Petch Coefficient	$32.5\sim52\,Hv\sqrt{\mu m}$	Furukawa et al.[92]

3.4 Analysis of the single grit force model behavior

Machining with a single grit is similar to the grooving process. The force model described above is used to predict the overall single grit forces based on the conventional material model in section 3.3. A breakdown of the predictions of the single grit forces is shown in Figure 3-8 and Figure 3-9.

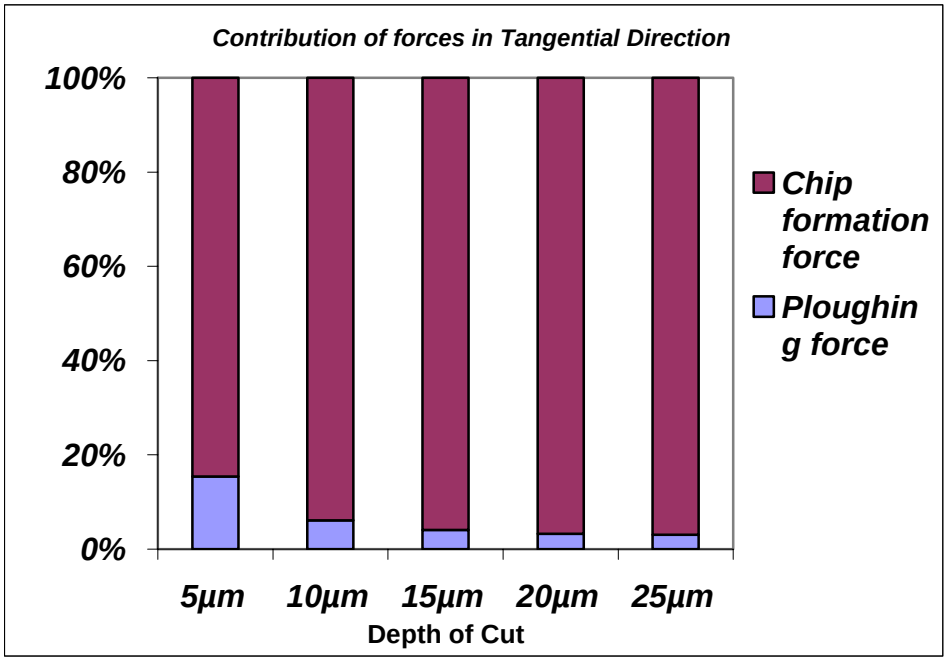

Figure 3-8: Breakdown of single grit force in normal direction for Grit size= 43µm, Vw=1mm/sec, and spindle RPM=60000

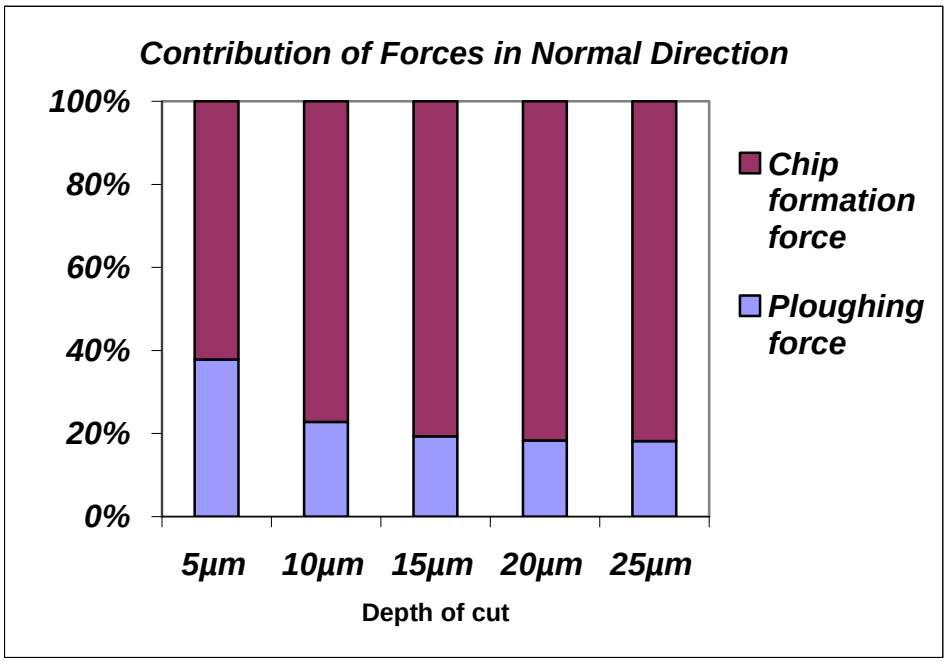

Figure 3-9: Breakdown of single grit force in tangential direction for Grit size= 43µm, Vw=1mm/sec, and spindle RPM=60000

These figures show that the ploughing effect becomes significant in small depths of cut as compared to micro-cutting. The overall forces of a single grit consist of chip formation and ploughing forces. In the radial direction, the ploughing force is around 40% of the overall forces of the single grit at low depths of cut. As the depth of cut increases, the percentage of the ploughing force decreases and chip formation forces become a dominant factor. In the case of the tangential direction, the contribution of ploughing force is smaller compared to a normal direction in Figure 3-9.

As the depth of cut increases, the contribution of the chip formation forces increases. The results of a breakdown of forces signify the effect of depth of cut while predicting the overall grinding forces.

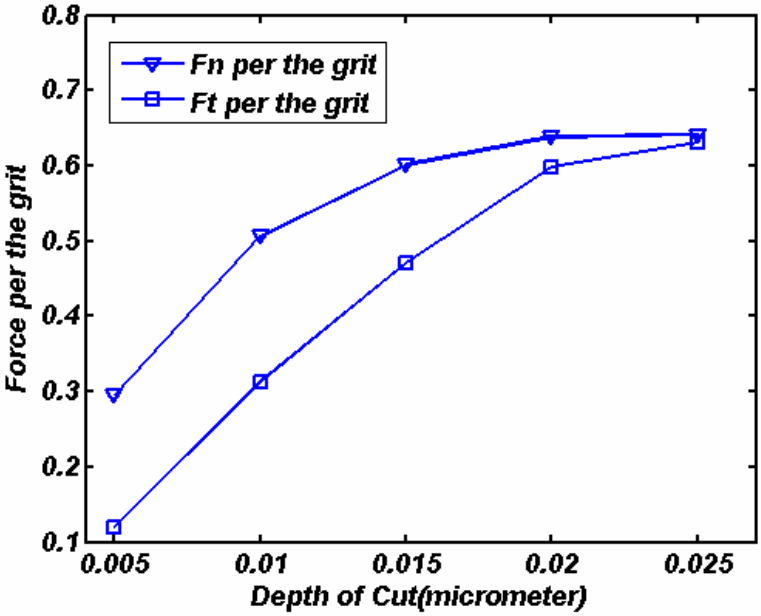

(a)

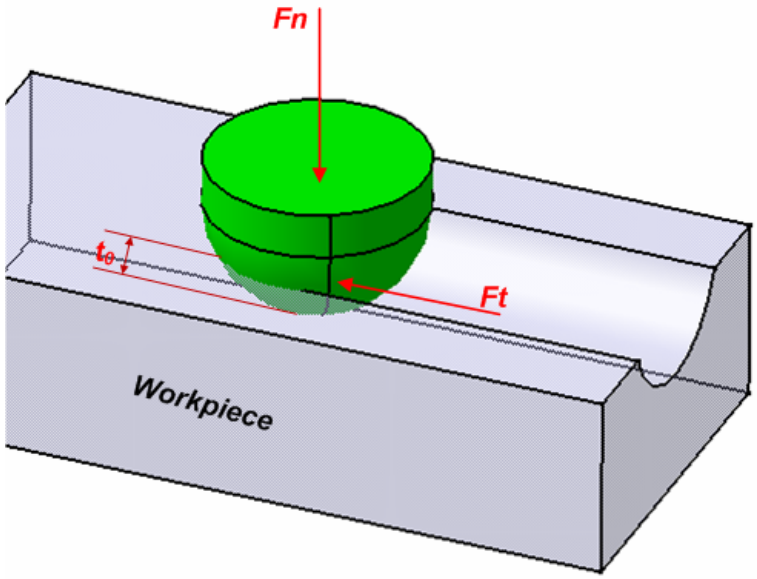

(b)

Figure 3-10: (a) Forces trend of the single grit in normal and tangential directions for $V_w = 1mm/\sec$ and (b) force configuration

In the case of the single grit forces, the normal forces are larger than the tangential forces. But the amount of the difference between them decreases as depth of cut increases.

3.5 Modeling of thermal effects in micro-grinding

Thermally induced stress to the workpiece during micro-grinding affects material behavior. During grinding, the duration of the heat pulse due to an individual grit is much shorter than that of the heat pulse on the workpiece contact zone. There are some examples of heat flux distribution such as a uniform and triangular law flux. A uniform flux in which pressure is uniform is used for polishing and honing processes. A triangular flux is approximate where the volume of chips is proportional to the depth of cut for grinding. The experiments of measuring grinding temperatures by Rowe et al.[93] supported this triangular flux approximation.

In this analysis, the heat generated during micro-grinding is approximated as a triangular heat source moving along the direction of the x-axis with the angle, φ, in Equation (3.37) between the line of motion and the plane of the band source as shown in Figure 3-11.

$$\varphi = \sin^{-1}\sqrt{\frac{t_0}{d_e}} \tag{3.36}$$

where φ is the inclination angle of the micro-grinding zone, t_0 is the depth of cut, and d_e is the micro-grinding wheel diameter

This band of heat on the contact zone between the workpiece and the grinding wheel is considered as a series of moving heat source elements. The solution for moving

heat source elements can be represented by Bessel functions and obtained by summing over the length of the micro-grinding contact surface.

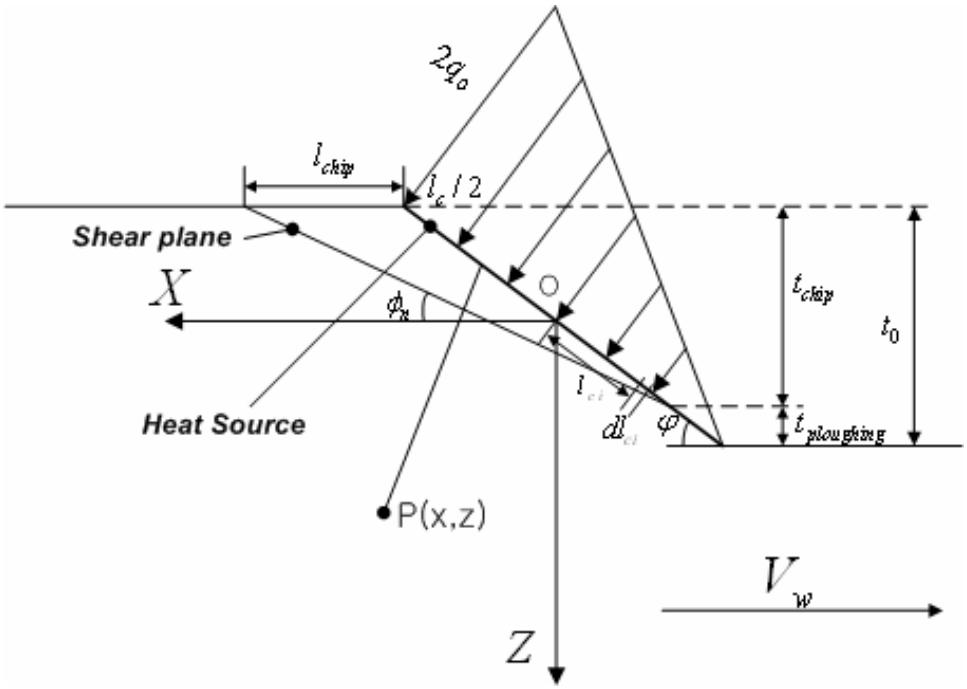

Figure 3-11: Schematic of the micro-grinding thermal model

Based on the Jaeger moving heat source model[34], the summation for the moving inclined triangular band source can be performed as the following:

$$T_{(x,z)} = \frac{qR_w}{\pi k}\int_{-\frac{l_c}{2}}^{\frac{l_c}{2}} e^{-\frac{V_w(x+a\cos\varphi)}{2\alpha}} K_0\left\{\frac{v[(x+a\cos\varphi)^2+(z-a\sin\varphi)^2]^{1/2}}{2\alpha}\right\}da \tag{3.37}$$

where K_0 is the second kind modified Bessel function, R_w is the heat partition ratio to the workpiece, q is the heat flux, φ is the inclined angle, V_w is the workpiece speed, k is the thermal conductivity, l_c is the contact zone, and α_{diff} is the thermal diffusivity.

For the triangular heat flux on the contact zone, the flux distribution can be expressed in the following form:

$$q = q_0\left(1+\frac{2a}{l_c}\right) \tag{3.38}$$

where $q_0 = \frac{F_x(V_s+V_w)}{l_c b}$ and $-\frac{l_c}{2} \le a \le \frac{l_c}{2}$

Based on the geometric relationship among parameters, the coordinate value of the shear plane corresponding to Figure 3-11 can be represented by

$$z_i = -\tan\phi_n\left(x_i+\cos\varphi\left(\frac{l_c}{2}-\frac{t_m}{\sin\varphi}\right)\right)+\sin\varphi\left(\frac{l_c}{2}-\frac{t_m}{\sin\varphi}\right) \tag{3.39}$$

The contact length model and its relation to the depth of cut is important to estimate the thermal effect in micro-grinding. Since elastic deflections between the tool and the contact surface can produce a change in the contact length, the geometric contact length model is not sufficient to describe the real contact length. Additionally, the surface of the workpiece in the microscopic view is not smooth. In order to account for these factors, the real contact length is calculated as Rowe et al.[94]

$$l_c = \left(t_0 d_e + 8R_r F_y^{'} d_e (K_s+K_w)\right)^{\frac{1}{2}} \tag{3.40}$$

where t_0 is the depth of cut, d_e is the effective diameter, R_r is the roughness factor, $F_y^{'}$ is the normal force per unit length, and K_i is the wheel (i=w)and workpiece(i=s) elasticity

The estimation of the real contact length based on this model will be more accurate as compared to the model that ignores the deflection effect. Within the model,

the roughness factor (R_r) is the ratio of the rough and smooth contact lengths. In the case of the rough surface, Rowe et al.[94] showed that a value of $R_r = 5$ provides a reasonable agreement between predicted and experimental contact lengths.

3.6 Calibration of heat partition ratio to the workpiece

To assess thermal effects in micro-grinding, it is important to understand heat transfer in micro-grinding. There are two different scales of heat transfer in grinding: (i) the heat transfer between the grit and workpiece and (ii) the heat transfer between the grinding wheel and workpiece. Heat transfers on two different scales interact with each other.

In dry micro-grinding, the total heat in the contact zone flows into three heat sinks: the workpiece, the micro-grinding wheel, and microchips because there is no heat loss due to fluid. So, partition ratios can be defined as the proportions of these fluxes to the total flux. Considering the energy convected by the microchips in the heat partition ratio to the workpiece is expressed as

$$R_w = R_{ws}\left(1 - \frac{e_{cc}}{e_c}\right) \tag{3.41}$$

where e_c is the process specific energy and e_{cc} is the energy to melt the workpiece material

In the micro-grinding process, the process specific energy is high and therefore the value of e_{cc} / e_c is negligible. The relationship of partition ratios is

$$R_w + R_s = 1 \tag{3.42}$$

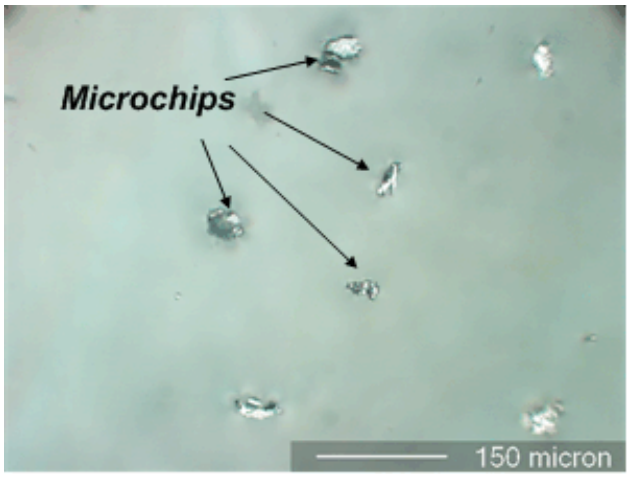

Figure 3-12: Microchips at 20μm depth of cut in micro-grinding

In this study, the heat partition ratio to the workpiece was calibrated by matching between experimental data using an embedded thermocouple and the analytically calculated temperature response in Figure 3-13.

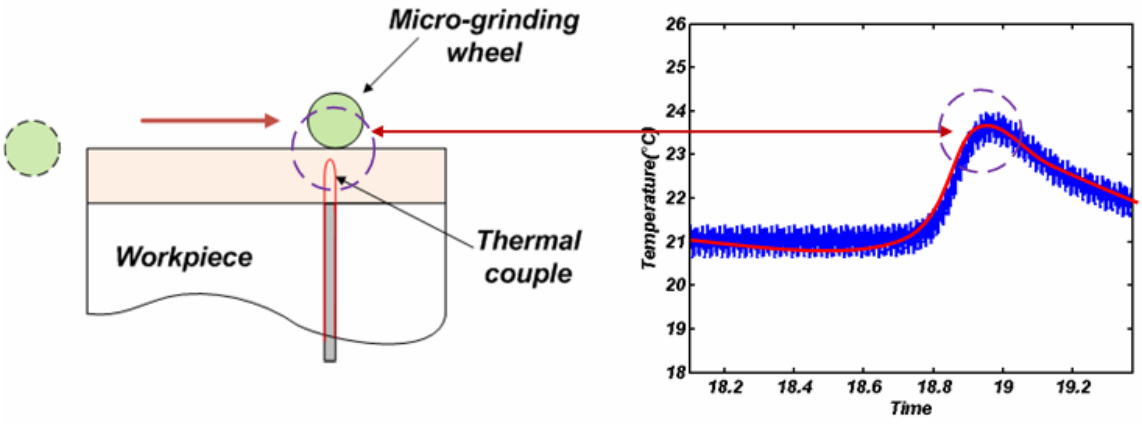

Figure 3-13: Temperature matching technique

The experimental setup to calibrate the heat partition ratio is illustrated in Figure 3-14. The surface micro-grinding experiment was conducted using an electroplated

micro-grinding wheel with diameter $d_e = 1$mm. The workpiece material was Al 6061-T6 with 15mm width and 1mm thickness. In order to measure the surface temperature, the embedded thermocouple technique was used with a K-type chromega®-alomega® thermocouple of diameter 0.0762mm.

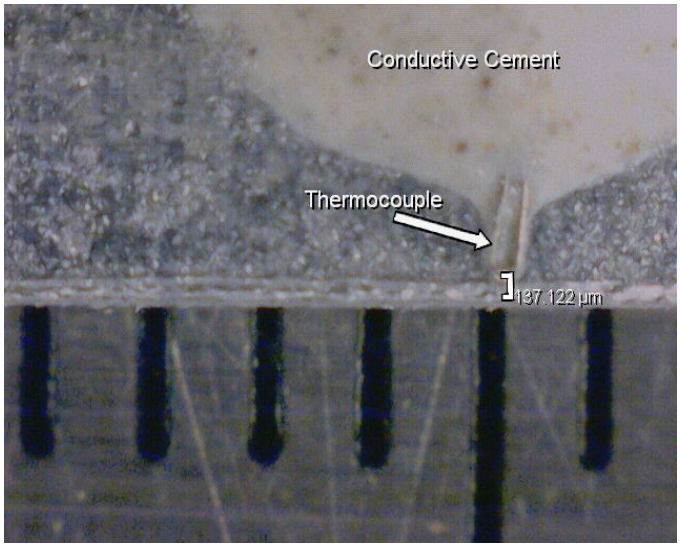

Figure 3-14: Experiment configuration for measuring the surface temperature

Tests were conducted in the upgrinding mode with the wheel speed of V_s =3.141m/sec, depth of cut of 15µm and 20µm, workpiece speed of V_w=1, 10, and 30mm/sec. Temperature responses and forces date were obtained for each test in order to determine the net heat flux. On the basis of the above temperature model, the temperature response was analytically estimated and compared with the results of surface micro-grinding tests. As a result of these computations, heat partition ratios to the workpiece were obtained. The trend of heat partition ratios to the workpiece is listed in Table 3-4.

Table 3-4: Estimated heat partition ratios to the workpiece

Depth of cut	RPM	Workpiece Speed	Rw (Heat Partition)
15μm	60000	1mm/sec	0.398905
15μm	60000	10mm/sec	0.419129
15μm	60000	30mm/sec	0.379072
15μm	60000	1mm/sec	0.440004
15μm	60000	10mm/sec	0.440103
15μm	60000	30mm/sec	0.374008
15μm	60000	30mm/sec	0.340414
20μm	60000	1mm/sec	0.415059
20μm	60000	10mm/sec	0.460162
20μm	60000	30mm/sec	0.415059

The results of computations are compared with the predictions of the Hahn model[36]:

$$R_{ws} = \frac{R_w}{R_w + R_s} = \left(1 + \frac{k_g}{\sqrt{r V_s (k_c \rho c)_w}} \right)^{-1} \tag{3.43}$$

where k_g is the grit thermal conductivity, k_c is the thermal conductivity, ρ is density, and c is the specific heat

The approximated values of thermal properties for CBN obtained by Rowe et al.[43] are summarized in Table 3-5.

Table 3-5: Thermal properties of CBN

	Conductivity	Density heat	Specific heat	$\beta = \sqrt{k \rho c}$
CBN	240W/mk	3480(kg/m^3	506(J/kgK)	20,600(J/m^{2}sK

The experimental results show that the values of heat partition ratio to the workpiece are in good agreement with those of the Hahn model as shown in Figure 3-15. This predictive model can therefore be used to estimate the heat partition ratio to the workpiece in surface micro-grinding.

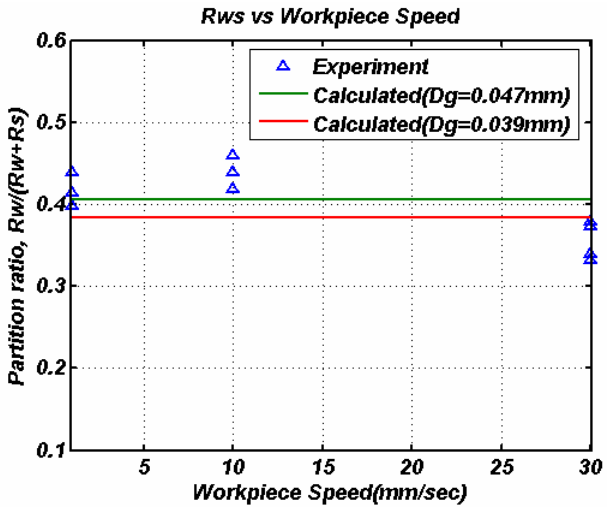

Figure 3-15: Comparison between experimentally calibrated values and analytical predictions

3.7 Summary

In this chapter, a new model for the mechanical interaction between the workpiece and an individual grit is developed considering both chip formation and ploughing mechanisms along with associated friction effects. It quantitatively predicts microgrinding forces per grit incorporating material properties as the functions of strain, strain rate and temperature. The results of computation of the single grit forces suggest that while the micro-cutting action is stronger than ploughing at large depths of cut, the ploughing effect becomes significant as the depth of cut becomes small.

The depth of cut in micro-grinding is less than the size of a grain in the material. Consequently the crystallographic effects become important. In order to capture the effect of microstructure including the grain size and dislocation in this study, additional stress terms based on the dislocation theory are added to the Johnson-Cook model.

For the assessment of thermal effects in micro-grinding, the temperature modeling based on the modified geometry and Jaeger's moving heat source model is performed. To understand the heat transfer in micro-grinding, the heat partition ratio to the workpiece is also experimentally calibrated and compared with the prediction of the Hahn model, which is one of the local scale models. It was found that the heat partition ratio to the workpiece is around 40% and these results are close to the calculated values of the Hahn model. But, the results are less than 65% of Outwater and Shaw[35] for typical grinding conditions.

CHAPTER 4

CHARACTERIZING THE TOPOGRAPHY OF A MICRO-GRINDING WHEEL

4.1 Introduction

The complexity in modeling the phenomena in micro and macro-grinding comes from the randomness of the shape and distribution of grit on the grinding wheel. The overall magnitude of micro-grinding forces depends on the topography of a micro-grinding wheel and the overall shape of its cutting edges. Understanding of micro-grinding wheel topography is crucial to modeling the micro-grinding process with high reliability. Various techniques such as profilometry, imprint method, scratch method, and microscopy have been developed to drive the topography of a grinding wheel. These techniques have their advantages and limitations. Verkerk et al.[46] provided the common distinction between static and dynamic cutting edge density. But, since measuring the dynamic cutting edge density is complicated, the dynamic cutting edge density is approximated from experimental data of the static cutting edge density incorporating the kinematics of cutting edges.

In this chapter, two methods that were adopted to derive the static cutting edge density corresponding to varying depths of cut are discussed. One is the optical method with replication and microscopic methods based on Hacker's approach [51]. The other one is the direct method based on the polishing method, which is proposed in this study. The static cutting edge densities using both methods are obtained with the assumption

described in Session 4.4. A comparison between the optical and direct method is performed. Then, the dynamic cutting edge density is obtained from the combination of the direct method and the kinematics of the cutting edges. The trend of the dynamic cutting edge density corresponding to changing workpiece speeds is illustrated.

4.2 Electroplated grinding wheel

The electroplated grinding wheel is a single layer wheel which is used for super-abrasives for economic reasons. Electroplated grinding wheels are fabricated at room temperature. In this study, since their sizes can be reduced below 1mm, Electroplated grinding wheels are adopted in micro-grinding. This type of grinding wheel consists of a single layer of super-abrasive grits such Diamond and CBN bonded to the steel core using nickel in Figure 4-1.

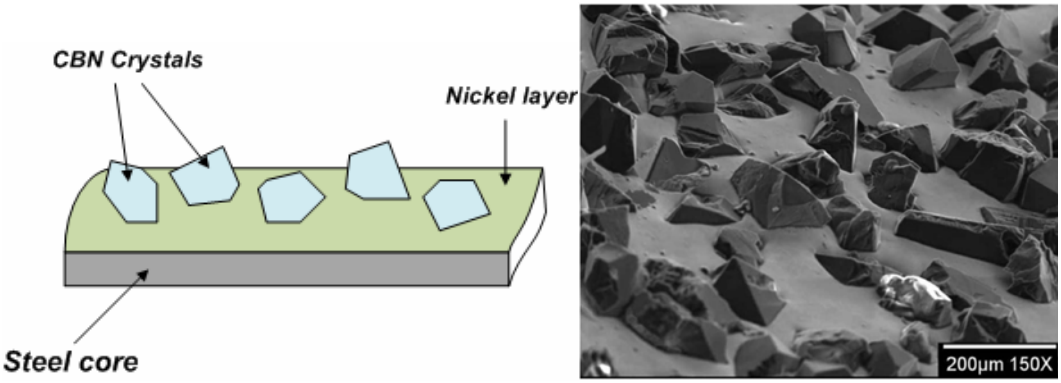

(a) (b)

Figure 4-1: Illustration of CBN grinding wheel and (b) SEM picture for 120 grit by Shi and Malkin[95]

4.3 Characterizing micro-grinding topography

In the following sections, the wheel topography of an electroplated CBN wheel specified as 85002-BM and with 240~270 grit number was experimentally analyzed. The size of this grinding is around 1mm based on the wheel specifications. Due to its size and curvature, it is very hard to directly extract information from the grinding wheel, which is shown in Figure 4-2.

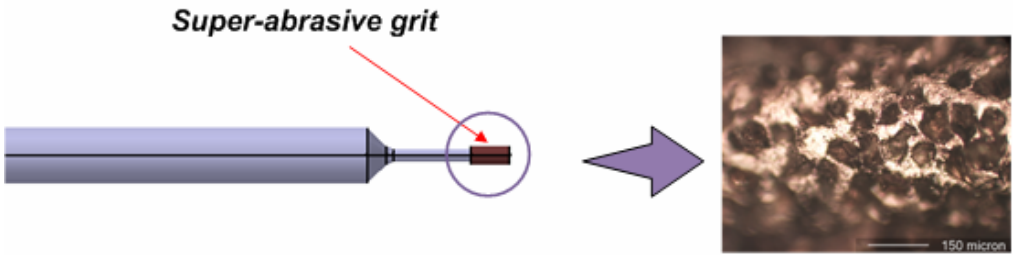

Figure 4-2: Illustration of 85002-BM electroplated CBN wheel

Due to resolution and the size of application, microscope method was adopted in this study. The direct method based on the polishing method is also proposed to characterize the micro-grinding wheel topography.

4.3.1 Optical method for the micro-grinding wheel topography

The ZYGO microscope offer a popular way to optically characterize the micro-grinding wheel topography because this method can provide a three dimensional profile of grinding wheel topography. Due to the difficulty of directly extracting the wheel topography, imprinting or replicating the wheel surface on a second body is necessary. For a second body for imprinting, lead plate is widely used due to its proper strength. But,

since the quality of acquired data is related to the surface reflectivity, polishing is needed in the preparation of lead samples.

A lead plate is polished with finer grade polishing papers. Then, the micro-grinding wheel surface is replicated or imprinted by the human hand which may not give a constant imprinting force. So, the maximum depth of penetration in replica surface is not consistent. The imprinted lead plate is shown in Figure 4-3.

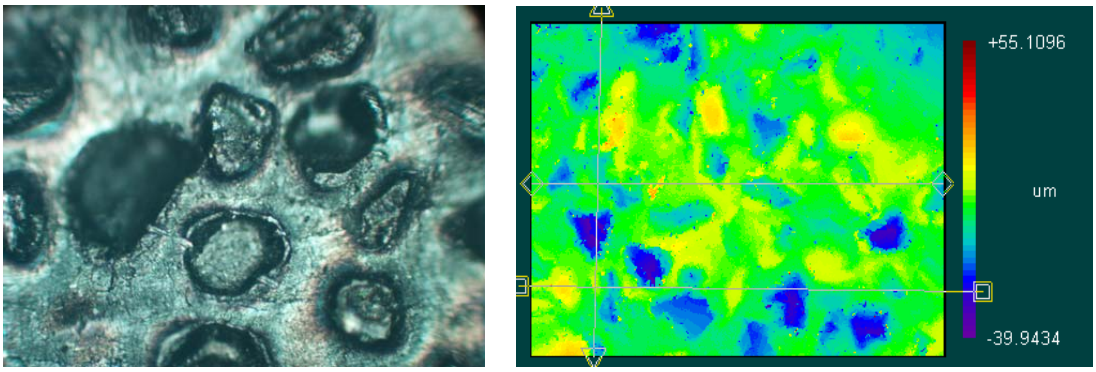

(a) (b)

Figure 4-3: (a) Example of replication on a lead plate and (b) measured profile of an imprinted lead plate

After imprinting a grinding wheel on a lead plate, the ZYGO white interferometer is adopted to measure the three dimensional profile of the imprinted lead plate with following optimal parameters:(i) Minimum modification:1%,(ii) Minimum size area:7,(iii)Scan length:40nm, and (iv) FDA resolution: normal. The resolution of an obtained image from the ZYGO microscopy is 2.2×2.2 microns per pixel. The images obtained have the overall size of 301×221 pixels.

Their actual size is equal to an area of 0.322 mm² per image. So, the static cutting edge density is given by

$$C_s = \frac{N_g}{0.322} \tag{4.1}$$

where N_g is the number of cutting edges and C_s is the static cutting edge density.

In this study, five different samples are prepared for experiments. Computational results of the optical method are shown in Figure 4-4.

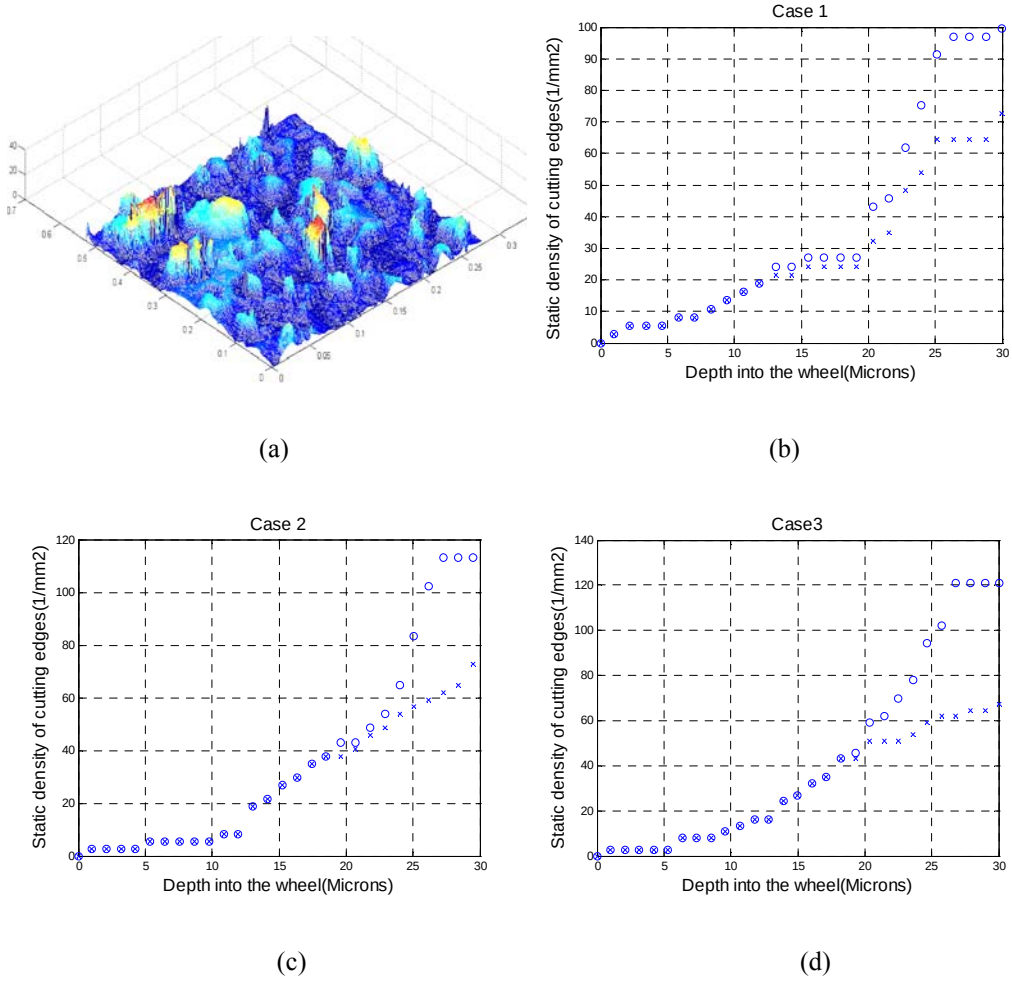

Figure 4-4: (a) Imported ZYGO optical image in MATLAB software, (b) Computed static cutting edge density in Case 1, (c) Case 2, (d) Case3, (e) Case4, and (f) Case 5

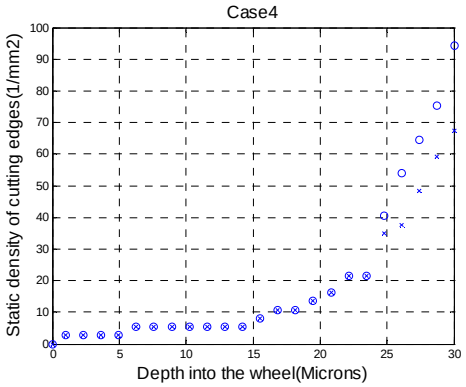

(e)

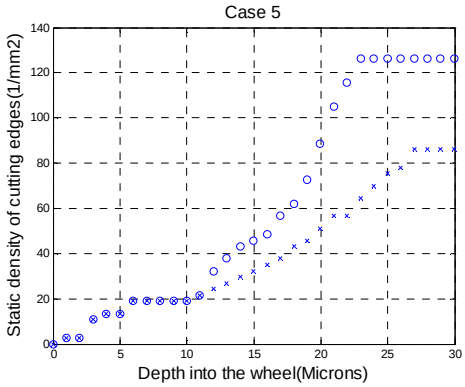

(f)

Figure 4-4: Continued

Experiment data of the optical method showed that there is significant variation of the static cutting edge density per each case. There are several error sources. One of these is that the quality of the obtained images highly depends on the amount of inadequate data at the measurement border and the inconsistency of the imprinted surface due to multiple reflections and optical signal distortion. The other reason is imprint process errors, which come from improper replication because the imprinting or replicating procedure of the hand press has uncertainty due to the elastic deflections of the grit and the micro-grinding wheel and the inconsistent hand pressing force.

4.3.2 Direct method for micro-grinding wheel topography

This proposed method is based on a polishing method with a cold mounting method and a 20x microscope to extract the profile of the micro-grinding wheel. The micro-grinding wheel size is around 1mm, which makes this technique possible. The

specimen samples for this proposed method are prepared using a castable mounting method because a castable mounting provides more accurate mounting. These specimens are polished with different size diamond suspensions in Figure 4-5(a).

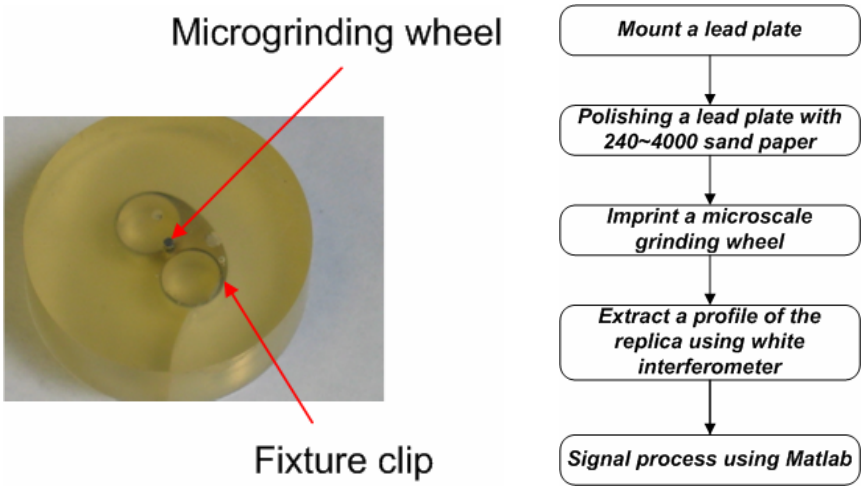

(a) (b)

Figure 4-5: (a) Illustration of a prepared sample and (b) Flowchart of the proposed direct method

In order to improve the quality of pictures, for one section profile, four pictures are taken and are assembled into one image, which is shown in Figure 4-6. There are two different experiments for fresh and worn micro-grinding wheels. Experimental data obtained from this method showed that in the case of worn tools. The nickel layer rapidly wears out and some grits are taken off from a base material.

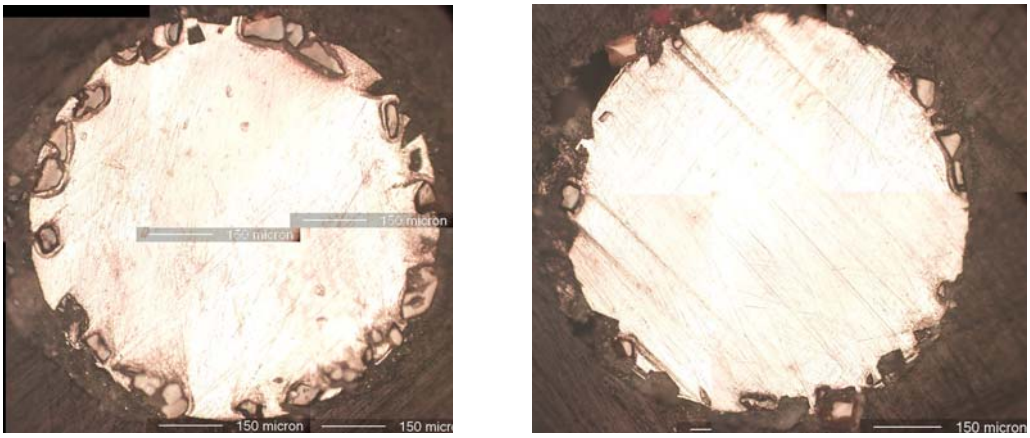

(a) (b)

Figure 4-6: Section profiles of (a) fresh and (b) worn micro-grinding wheels

On the basis of these constructed images, the profile is extracted using mathematical computation in MATLAB software. Profile data extracted from section cuts are used to compute the diameters of the micro-grinding wheels and the size of CBN grits.

In both cases, the least square nonlinear regression method is adopted because this method has been widely used to solve sets of nonlinear equations given extracted data points. The optimality criterion of this method is to minimize the sum of residual squares between observed data and the values of the approximate numerical model. In the case of two coordinate variables (x and y), a mathematical representation for the circle estimation is given by

$$f(x, y) = x^2 + y^2 ax + by + c = 0 \tag{4.2}$$

To determine the mathematical representation model parameters (a, b, and c), a least square error regression analysis will be pursued. Briefly, for a measured data

set (x_1, y_1) (x_2, y_2), …, $(x_{n,} y_n)$ a multiple regression least squares method can provide the best mathematical expression which is affected by two coordinate variables. This method assumes that the best mathematical representation form is the approximation that has the minimal sum of the least square error for a given set of data. According to the least square method, the best fitting mathematical expression has the following property:

$$D = \sum_{i=1}^{n} \left(y_i^2 - y_{ci}^2 \right)^2 = \sum_{i=1}^{n} \left\{ y_i^2 + \left(x_i^2 + a x_i + b y_i + c \right) \right\}^2 = \min \tag{4.3}$$

To obtain the least square error in this case, unknown coefficients (a, b, and c) have to produce the following zero first derivatives:

$$\begin{aligned} \frac{\partial D}{\partial a} &= 2 \sum_{i=1}^{n} \left(y_i^{\,2} + x_i^{\,2} + a x_i + b y_i + c \right) \cdot x_i = 0 \\ \frac{\partial D}{\partial b} &= 2 \sum_{i=1}^{n} \left(y_i^{\,2} + x_i^{\,2} + a x_i + b y_i + c \right) \cdot y_i = 0 \\ \frac{\partial D}{\partial c} &= 2 \sum_{i=1}^{n} \left(y_i^{\,2} + x_i^{\,2} + a x_i + b y_i + c \right) = 0 \end{aligned} \tag{4.4}$$

Expanding Equation(4.4), these formulations become

$$\begin{aligned} \left[\sum_{i=1}^{n} x_i^{\,2} \right] a \quad &+ \left[\sum_{i=1}^{n} x_i \cdot y_i \right] b + \left[\sum_{i=1}^{n} x_i \right] c = -\sum_{i=1}^{n} \left(x_i y_i^{\,2} + x_i^{\,3} \right) \\ \left[\sum_{i=1}^{n} x_i \cdot y_i \right] a + \left[\sum_{i=1}^{n} y_i^{\,2} \right] b \quad &+ \left[\sum_{i=1}^{n} y_i \right] c = -\sum_{i=1}^{n} \left(x_i^{\,2} y_i + y_i^{\,3} \right) \\ \left[\sum_{i=1}^{n} x_i \right] a \quad &+ \left[\sum_{i=1}^{n} y_i \right] b \quad + n \cdot c \qquad = -\sum_{i=1}^{n} \left(x_i^{\,2} + y_i^{\,2} \right) \end{aligned} \tag{4.5}$$

So, the unknown coefficients (a, b, and c) can be obtained by solving the above equations. On the basis of this concept, the estimation for the circle is performed. The computational output is in Figure 4-7.

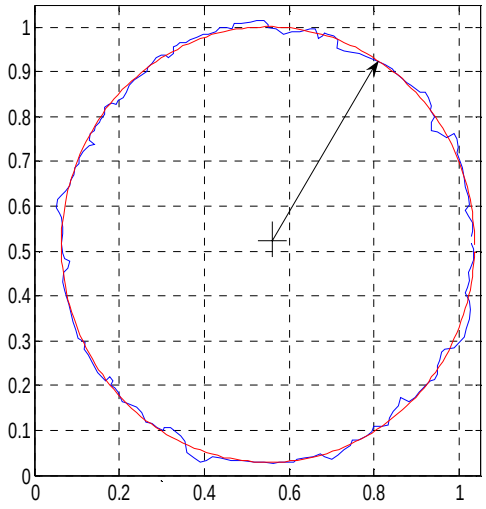

Figure 4-7: Circle fitting in MATLAB software

The results of estimation of the diameter of micro-grinding wheels showed that there is 10% difference of a diameter between fresh and worn tools. The reduction of a diameter in worn tools decreases the wheel speed.

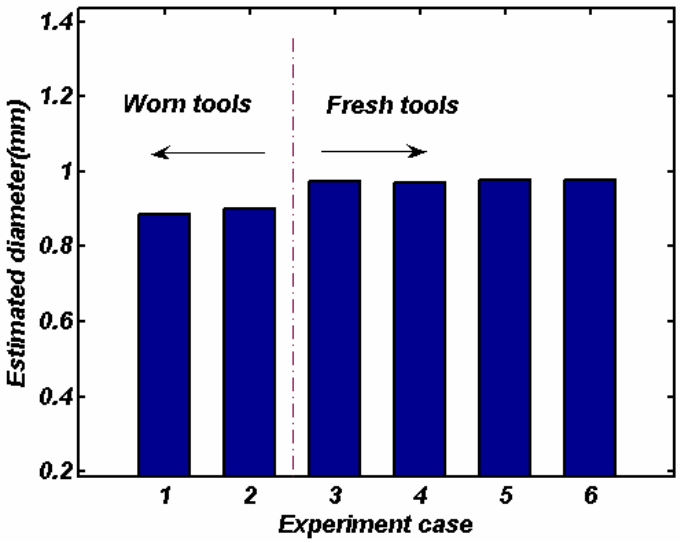

Figure 4-8: Estimated diameter of micro-grinding wheels

Table 4-1: Profiles of section cuts of CBN 85002-BM worn and fresh wheels

Type	Section cuts of 85002-BM micro-grinding wheel			
Worn wheels	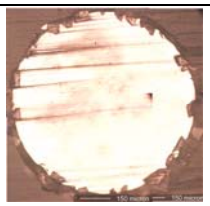		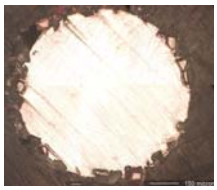	
	Case1		Case2	
Fresh wheels			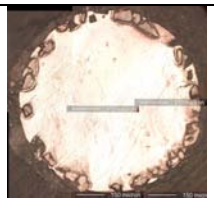	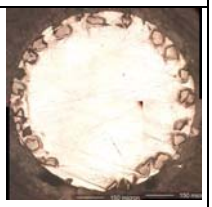
	Case3	Case4	Case5	Case6

In order to estimate the size of the grit, the profile of the grits is obtained and regressed using a method similar to that used in Figure 4-9.

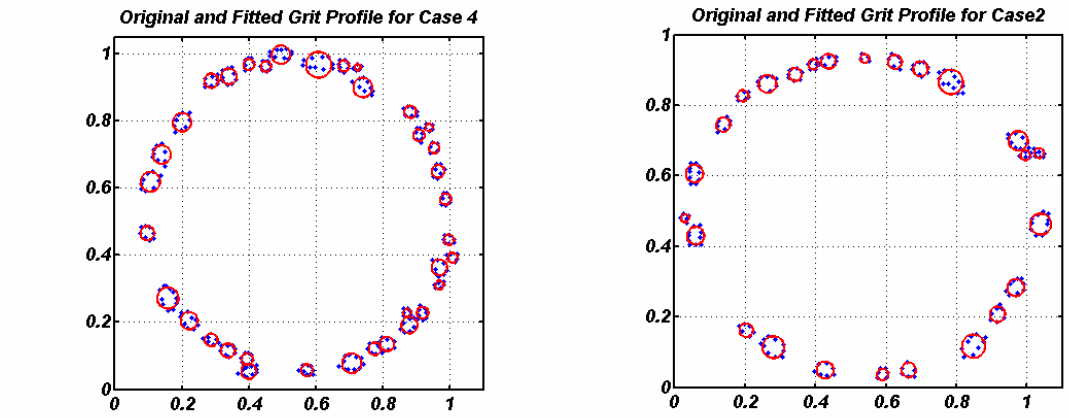

(a) (b)

Figure 4-9: Calibration of the grit size on (a) fresh and (b) worn micro-grinding wheels

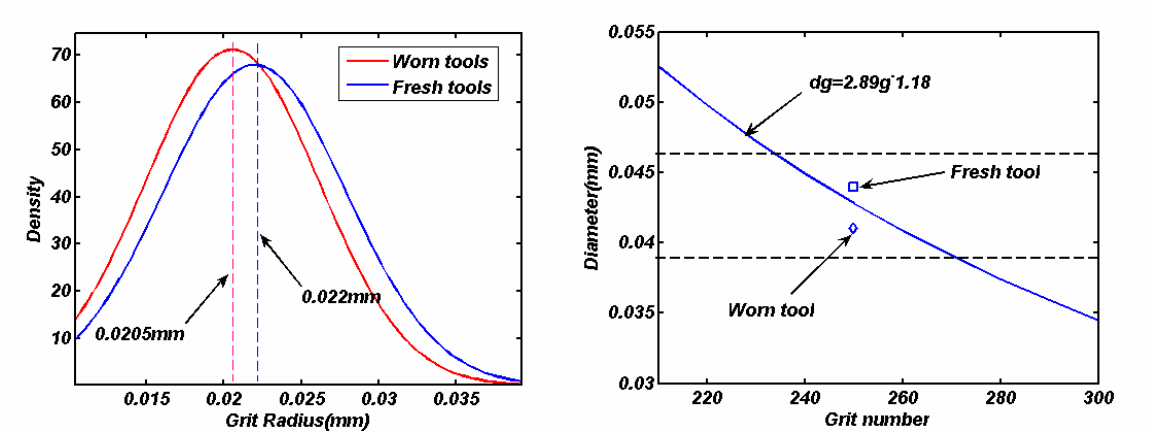

(a) (b)

Figure 4-10: (a) Fitted normal distributions of new and worn micro-grinding wheels and (b) Plot of the mean grit diameter versus the grit number

The grit size distribution from these experiments is shown in Figure 4-10(a). Based on these experimental results, it seems that the distribution of the grit is well matched with a normal distribution suggested by Hou and Komanduri[96]. The mean and standard deviation of experiment data are summarized in Table 4-2.

Hou and Komanduri[96] proposed a relationship between the grit number and size, which is given by

$$d_g = 28.9 g^{-1.18} \tag{4.6}$$

where d_g is the grit size and g is the grit number

Typical values of the grit size for a grinding wheel in the range of 230-270 falls in the range 39 to 47μm from Equation(4.6). Comparison between experiment data and Equation (4.6) shows that experimental results fall within the approximate range of the above equations.

Table 4-2: Estimation of the size of grits for fresh and worn tools

	Fresh tool	Worn tool
Mean (radius)	0.022mm	0.0205mm
Standard Deviation	0.0056mm	0.0059mm

4.4 Comparison between optical and direct methods

The type of experimental data obtained from the direct method is different from those obtained in the optical method. Two-dimensional data of the direct method have to be transformed to make possible a comparison between two methods.

To transform the experiment data of a direct method, the width of two dimensional profiles has to be decided. So, based on the assumption that the grit is spherical in shape, the width can be approximated to be equal to the maximum size of grits in the profile cross section line because the extracted grit profile in the images is the cross section of the spherical grits.

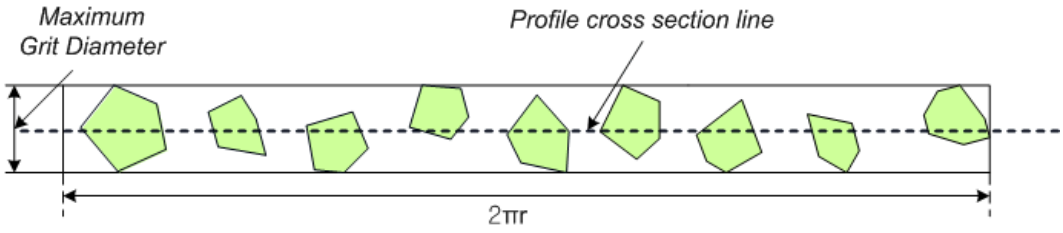

Figure 4-11: Schematic illustration of extension for the extracted profile data

On the basis of this concept, the static cutting edge density, which is the number of active grits per unit area of the micro-grinding wheel surface, can be determined using the direct method. In the case of the optical method, their experiment data are already

three dimensional profiles having a specific area. In MATLAB software, the static cutting density can be obtained.

For both methods, since the experimental data is very widely scattered, the process smoothing experiment data obtained is necessary prior to the regression analysis. A moving averaging method is used to smooth the experimental data, which is equivalent to low pass filtering. This method smoothes raw experiment data by replacing these data with the average value of the neighboring data points with the defined span. Equation (4.7) by Hacker[51] can be adopted to represent the static cutting edge density

$$C_s = A_s Z^{k_s} \tag{4.7}$$

On the basis of these smoothed data, a non-linear regression analysis is performed within the range of the grit radius. The computation results are summarized in Table 4-3.

Table 4-3: Summary of computations for static cutting density

Cases		A_s	k_s	R_a
Direct method	Fresh tool	2.355	0.922	0.984
	Worn tool	2.211	0.8527	0.961
Optical method for fresh tool		1.609	0.9019	0.887

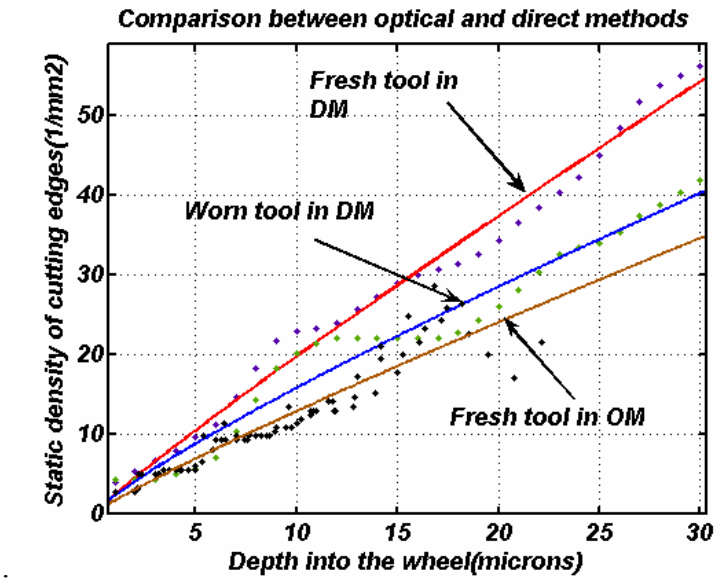

Figure 4-12: Comparison between the optical and direct methods

A comparison between the two methods shows that a static cutting edge density of the direct method for fresh and worn tools is higher than that of the optical method for a fresh tool. In the case of the optical method, as mentioned earlier, there are several issues in the imprinting technique such as trapped grits inside wheel and merging adjacent grits, which have an influence on the static cutting edge density. As depths of cut increase, these effects become greater in the optical method. So the difference between the two methods increases, which is shown in Figure 4-12. In a comparison between fresh and worn tools using the direct method, the fresh grinding wheel has a higher static cutting edge density than the worn grinding wheel. Although there is a slight difference in the grit sizes, the main reason for this is that some CBN grits are taken off from the base material during micro-grinding. So, in the following section, information obtained from the direct method is used to compute the dynamic cutting edge density.

4.5 Dynamic cutting edge density

Cutting edges on the micro-grinding wheel are not equally spaced and uniformly involved on the micro-grinding process. Thus, the small percentage of static cutting edges, which is the dynamic cutting edge, is engaged to remove the workpiece in micro-grinding. It depends on the kinematics of the micro-grinding process and the static cutting edge density. The formulation proposed by Verkerk et al.[46] is

$$C_d = C_s \left(\frac{V_w}{V_s} \right)^{C_g} \left(\theta_{\text{infeed}} \right)^{C_g} \tag{4.8}$$

where V_s is the wheel speed, V_w is the workpiece speed, θ_{infeed} is the infeed angle, and C_g is a constant of the dynamic effect for a specific wheel.

On the basis of the geometric relationship, the profile of grits obtained from the direct method can be stretched into the line by subtracting the curvature from the original data as shown in Figure 4-13(a). Due to the infeed angle related to the dynamics of micro-grinding, the preceding cutting edge kinematically hides the next incoming small cutting edges, which makes a small portion of the cutting edges contact with the workpiece during grinding. These effects provide the difference between the static and dynamic cutting edge density.

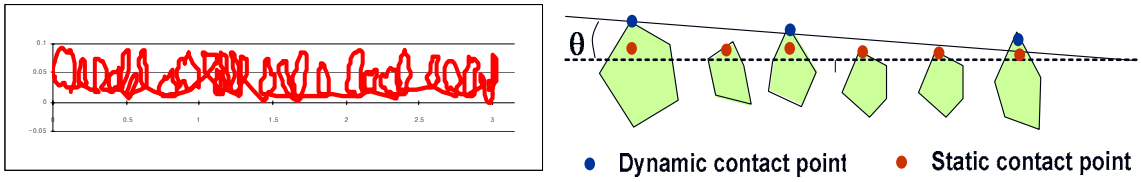

(a) (b)

Figure 4-13: (a) Tracing and (b) illustration of dynamic cutting edges

This infeed angle is represented from the geometrical and kinematical relationship according to the following equation:

$$\theta_{\text{infeed}} = \tan^{-1}\left(\frac{V_w}{V_s}\sqrt{\frac{t_0}{d_e}}\right) \tag{4.9}$$

where t_0 is the depth of cut and d_e is the diameter of the micro-grinding wheel.

The above equation shows that as the workpiece speed and the depth of cut increase, the infeed angle increases so that the number of engaged grits in micro-grinding increases. From the experimental data of the direct method, the dynamic effect can be estimated according to varying workpiece speeds, and the constant of dynamic effect for this micro-grinding wheel is obtained from the mathematical computation on the basis of the above equation.

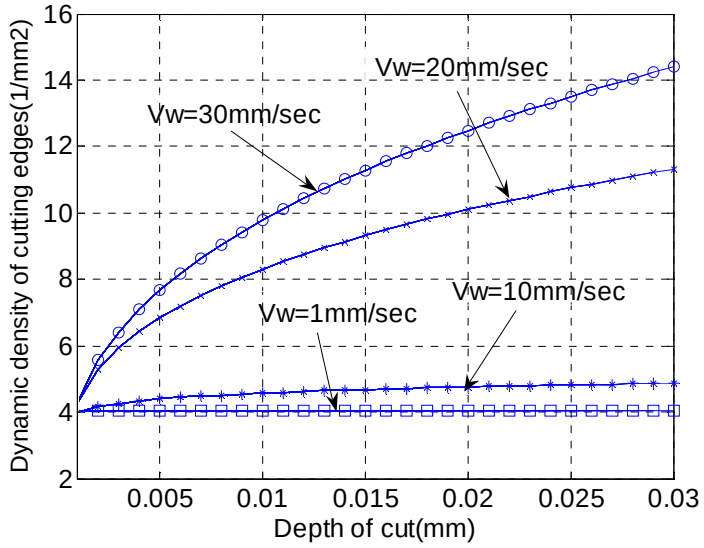

Figure 4-14: Dynamic density of cutting edges for $V_w = 1mm/\sec$, $V_w = 10mm/\sec$, $V_w = 20mm/\sec$, and $V_w = 30mm/\sec$ in the direct method

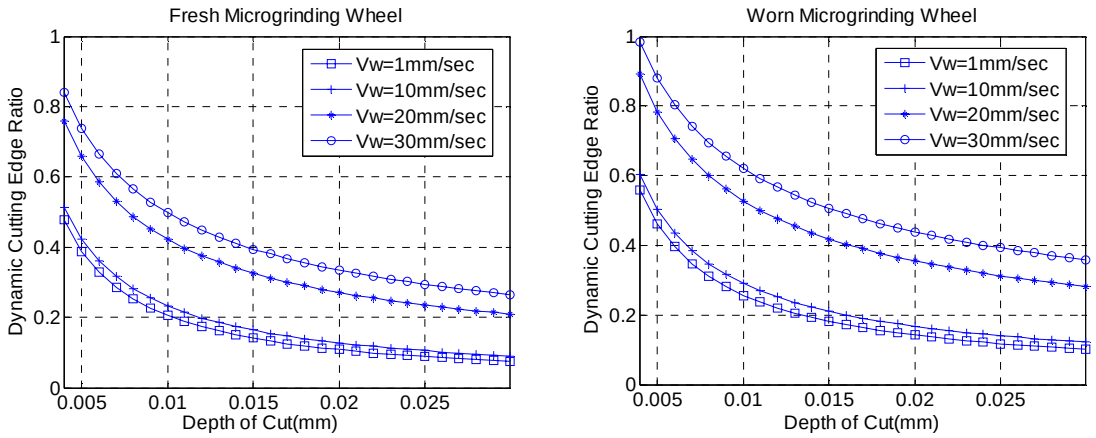

(a) (b)

Figure 4-15: Ratio variation of dynamic cutting edge density to static cutting edge density for varying workpiece speed in direct method

It is found that as the workpiece speed increases, the dynamic cutting density increases due to an increase in the infeed angle shown in Figure 4-14. The dynamic effect is small at low depths of cut. So, the dynamic cutting edge density is close to the static

cutting edge density. But, as the depth of cut increases, these effects become more significant. Around 10~30% of the static cutting edges are engaged in grinding. The dynamic cutting edge density can be represented by Equation(4.7). The computational results are summarized in Table 4-4.

Table 4-4: Regression results of dynamic cutting edge density

Workpiece speed (V_w)	A_s	k_s
$1mm/\sec$	4.035	0
$10mm/\sec$	5.961	0.05745
$20mm/\sec$	30.35	0.2812
$30mm/\sec$	49.33	0.3512

These computational results are used to predict the overall micro-grinding forces in Chapter 5.

4.6 Summary

In this chapter, a methodology to characterize micro-grinding wheel topography was discussed. Since there are difficulties in directly measuring wheel topography, two methods were adopted to derive the static and dynamic grit density, which are the optical method and the direct method. From these computations, important parameters were obtained. These parameters are the sizes of the micro-grinding wheel and grits on the grinding wheel, the static and dynamic cutting edge density.

In the case of the size of the micro-grinding wheel, it is found that there is 10% difference between a fresh and a worn grinding wheel. Experiments to determine the size of grit also show 2μm difference of mean value between them, and the distribution of the grit size is close to the normal distribution as was the case in the assumption proposed by Hou and Komanduri[96].

The computational results based on two methods for static cutting edge show that the static cutting edge density obtained from the direct method is higher than that of the optical method. As the depth of cut increases, the differences between both methods increase around 12.5% for worn wheels and 36% for fresh CBN electroplated grinding wheels.

Computations of the dynamic cutting edge showed that 10~30% of the static cutting edges are engaged in grinding at high depths of cut. In the case of micro-grinding wheels, their diameters are smaller than those of conventional grinding wheels, which is related to an increase in the infeed angle. Due to this increase of the infeed angle, the results computed are higher than 2%~12% of Younis et al.[47].

CHAPTER 5

COMPARISON BETWEEN THEORETICAL AND EXPERIMENTAL COMPUTATIONS

5.1 Introduction

Micro-grinding is a process which can be used to produce a good quality product. In considering the characteristics of the micro-grinding process, prediction of micro-grinding forces is a prerequisite to estimation of other factors such as tool life prediction, process planning of micro-grinding and chatter analysis.

In this chapter, a model to predict micro-grinding forces is discussed and compared with experimental data for micro-grinding an aluminum alloy (Al 6061-T6). Based on modeling techniques of thermal and mechanical deformation on the micro-grinding zone that were presented in Chapter 3, a model was developed to predict micro-grinding forces, incorporating material properties as functions of strain, strain rate, and temperature, characterization of micro-grinding wheel topography that were obtained in Chapter 4, and the kinematics of the micro-grinding process.

Consequently, the experimental determination of the grain size of the micro-structure is discussed in this chapter. Side micro-grinding tests over a wide range of grinding speeds and depths of cut were conducted to validate the proposed micro-grinding model. The effects of rising temperature on a micro-grinding zone were estimated using the model in Chapter 3. A comparison between experimental data and

predictions is made by combining the results from the micro-grinding force and temperature models.

5.2 Comprehensive model of micro-grinding forces

The overall scheme of the predictive model of micro-grinding forces is shown in Figure 5-1. The analytical modeling of micro-grinding starts from the individual grit interaction discussed in Chapter 3 and then is commonly extrapolated into a whole grinding wheel surface similar to the conventional grinding process based on the characterization of the micro-grinding topography in Chapter 4. The inputs of this proposed model are material properties based on the Johnson-Cook model and dislocation theory including the microstructure effect, geometric parameters of the micro-grinding wheel including the size of grits and the micro-grinding wheel, and process parameters including the cutting speed, depth of cut, the workpiece speed, etc.

The first step of the predictions based on this model is the computation of the single grit forces including the chip formation forces and ploughing forces using Equations (3,10-11) and (3.16-17). Then, the temperature and contact length are computed from Equations (3.37) and (3.40). The single grit forces computed are extrapolated in the micro-grinding wheel using the extracted micro-grinding topography. A comparison between the predictions and experimental data is performed in this study.

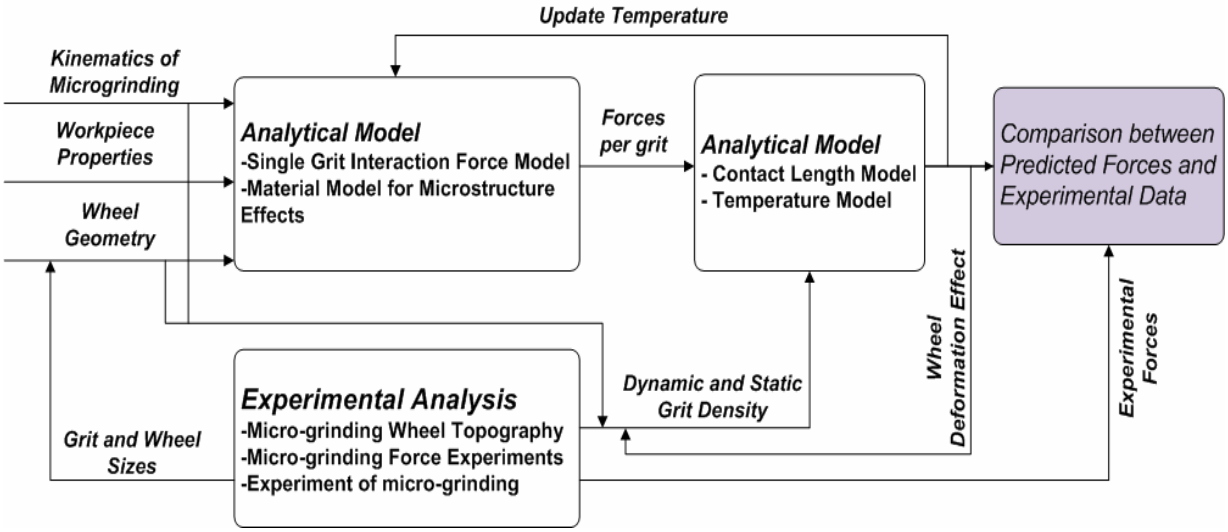

Figure 5-1: Illustration of the predictive model of the micro-grinding forces

5.2.1 Sensitivity analysis of a comprehensive model

A sensitivity analysis of model parameters on micro-grinding forces was performed to investigate the effects of parameters for the variation of force outputs. Four model inputs chosen in this sensitivity analysis are the micro-grinding wheel size, the size of the grain, percentage of ploughing effect, and spindle RPM. The Taguchi method with three levels is adopted to determine the effects of the factors chosen. The levels for each factor are listed in Table 5-1.

Table 5-1: Input factor levels for sensitivity analysis

Factors	Low	Medium	High
Grinding wheel size(mm)	0.75 mm	1.00 mm	1.25 mm
Grit size(μm)	30 μm	40 μm	50 μm
Ploughing effect ratio(%)	12%	15%	18%
RPM	40000rpm	50000rpm	60000rpm
Responses	Normal (F_y) and tangential(F_x) forces		

The plots of the main effects for normal (Fy) and tangential (Fx) forces are shown in Figure 5-2(a) and (b). The results show that the predictions of micro-grinding forces in this model are strongly influenced by the size of grits in the range of inputs for both forces. The ploughing effect ratio and the size of the micro-grinding wheel also affect the predictions of these forces.

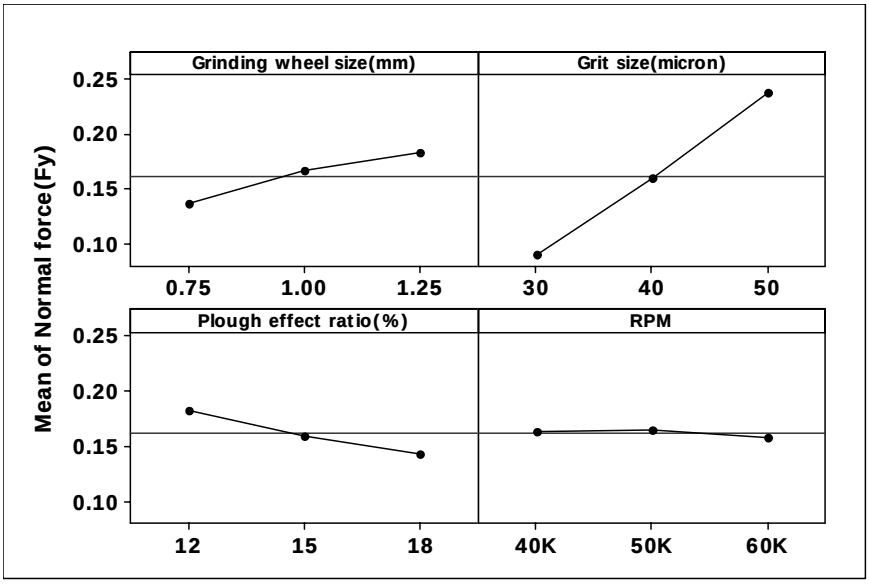

(a)

Figure 5-2: Main effect plots of (a) Fy and (b) Fx

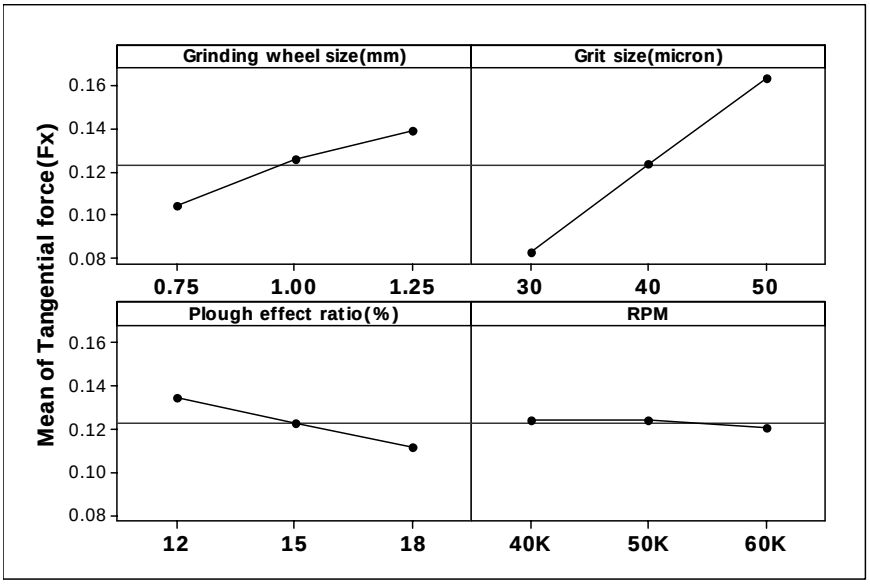

(b)

Figure 5-2: Continued

The reason is that the predictions of both forces are based on the single interaction model in discussed in Chapter 3.

5.3. Experiment of micro-structure characterization

5.3.1 Experiment for measuring the grain size

Metals such as steel and aluminum consist of three dimensional aggregations of different size and shape grains. As the depth of cut decreases during machining, understanding the microstructure is vital to any prediction of a material's response under given process conditions. In this study, the microstructure of Al 6061 T6 is investigated to validate the proposed model. The samples for this experiment were prepared using traditional mounting methods in Figure 5-3 and polished with different size sand papers.

These samples are finally polished using NANOCLOTH paper and 0.05µm alumina. Based on the literature survey[97], these samples are electrolytically etched using the modified barker's reagent: 108 ml of distilled H_2O, 3.75 HBF_4, and 37.5 of H_2O_2 to remove the grain boundaries of the samples.

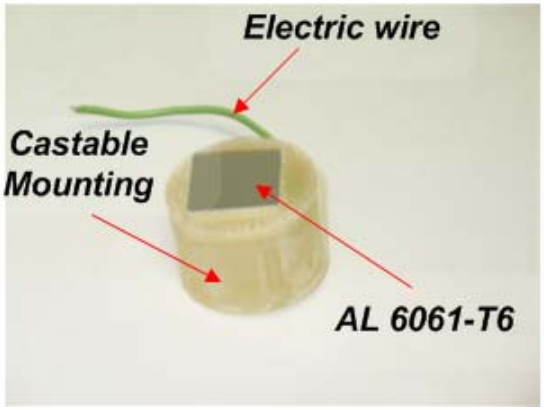

Figure 5-3: Scheme of the prepared Al 6061-T6 sample

The images of the etched sample were taken using an optical microscope with a polarized light in Figure 5-4(a) and (b). Based on the obtained images, the shape of grains is analyzed using the optical software.

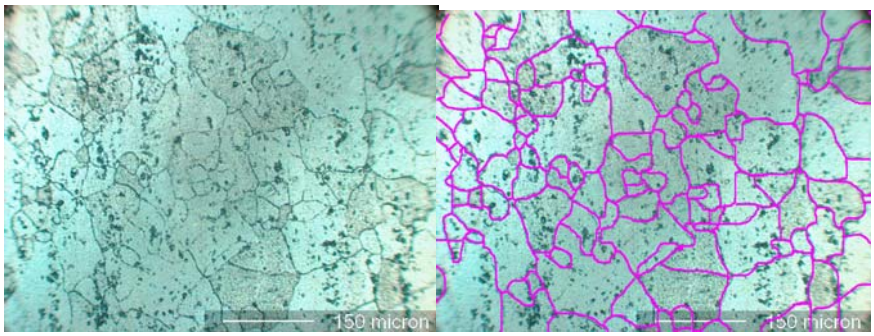

(a) (b)

Figure 5-4: Processed images in (a) sample position 1, (b) sample position 2, (c) sample position 3, and (d) sample position 4

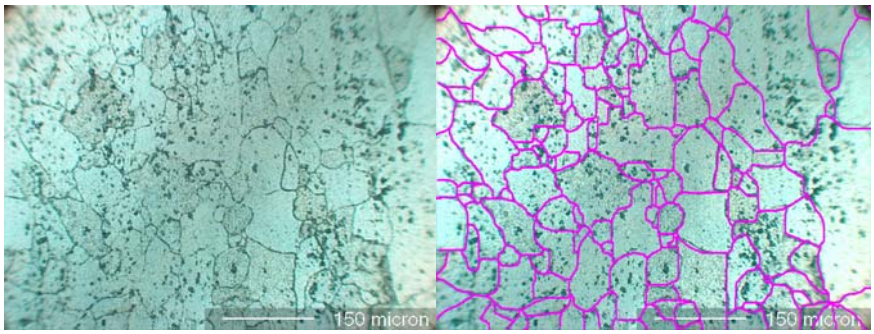

(c) (d)

Figure 5-4: Continued

Generally, there are two popular methods to determine the size of grains: (i) the caliper diameter method and (ii) the line interaction method. In the caliper diameter method, grain size is estimated or measured on the cross section of an aggregate of these individual grains. Due to the number of grains on the samples, in this study, the average size of the grains is estimated from the line intercept method as shown in Figure 5-5.

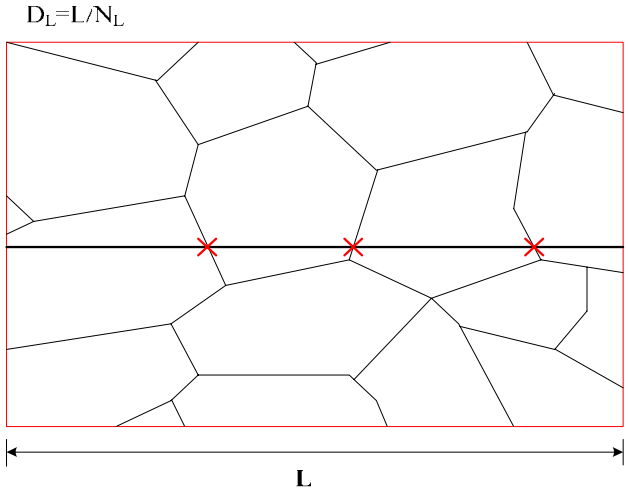

Figure 5-5: Illustration of the line intercept method for measuring the size of grains

In this method, the number of intercepts per unit length is related to the average size of grains in the obtained images; the average size of grains will be given by

$$D_d = \frac{L}{N_L} \tag{5.1}$$

where N_L is the number of line intercepts with grain boundaries

This calculation of the number of intercepts of the Al 6061 T6 sample is carried out using Microstructure Characterizer software developed by TCR engineering. The computational results of the samples are shown in Figure 5-6.

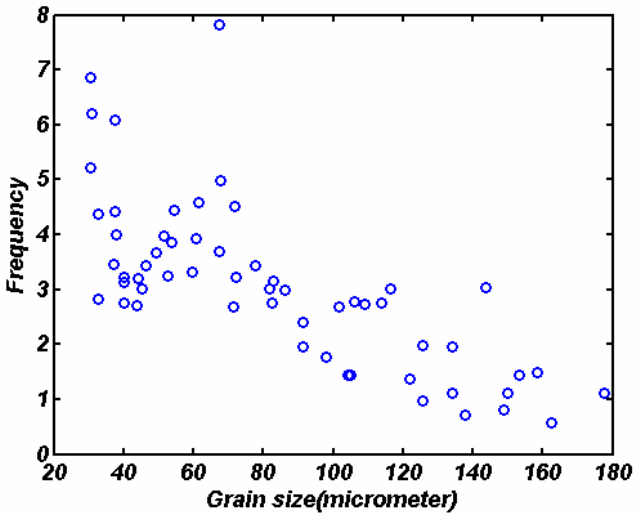

Figure 5-6: Experimental data of the average grain size

To extract the mean and standard deviation of the experimental data, mathematical computation is necessary. The expected value or expectation of discrete variables with a probability mass function can be given by

$$E(X) = \sum_i p_i x_i \tag{5.2}$$

where p_i is the probability and x_i is the frequency

The computed expectation provides a summary of the average value of the discrete values experimentally measured. Another stochastic value is the variance of discrete variables of experimental results. The variance is given by

$$Var(X) = E(X^2) - (E(X))^2 \tag{5.3}$$

On the basis of the above equations, the values of expectation and variance obtained from the experimental data for Al 6061-T6 are E(X)=67.427 and Var(X)=1003.615. Generally, the distribution of the grain size is represented by a log-normal distribution to avoid laborious specimen handling. A log-normal distribution is given by

$$f(x;\mu,\sigma) = \frac{1}{x\sigma\sqrt{2\pi}} e^{-\frac{(\ln x-\mu)^2}{2\sigma^2}} \tag{5.4}$$

where μ and σ are mean and standard deviation.

Mean (μ) and standard deviation (σ) of the log-normal distribution established by Brown and Aitchison [98] based on the obtained expectation and variance can be calculated by

$$\mu = \ln(E(X)) - \frac{1}{2}\ln\left(1+\frac{Var(X)}{E(X)^2}\right) \tag{5.5}$$

$$\sigma^2 = \ln\left(1+\frac{Var(X)}{E(X)^2}\right) \tag{5.6}$$

The values of mean and standard deviation for Al 6061 T6 are 4.11 and 0.4467. The log-normal distribution of Al 6061 T6 engaged in this experiment is given by

$$f(x;4.11,0.4467)=\frac{1}{0.4467\sqrt{2\pi}x}e^{-\frac{(\ln x-4.11)^2}{0.399}} \tag{5.7}$$

The obtained log-normal distribution is shown in Figure 5-7.

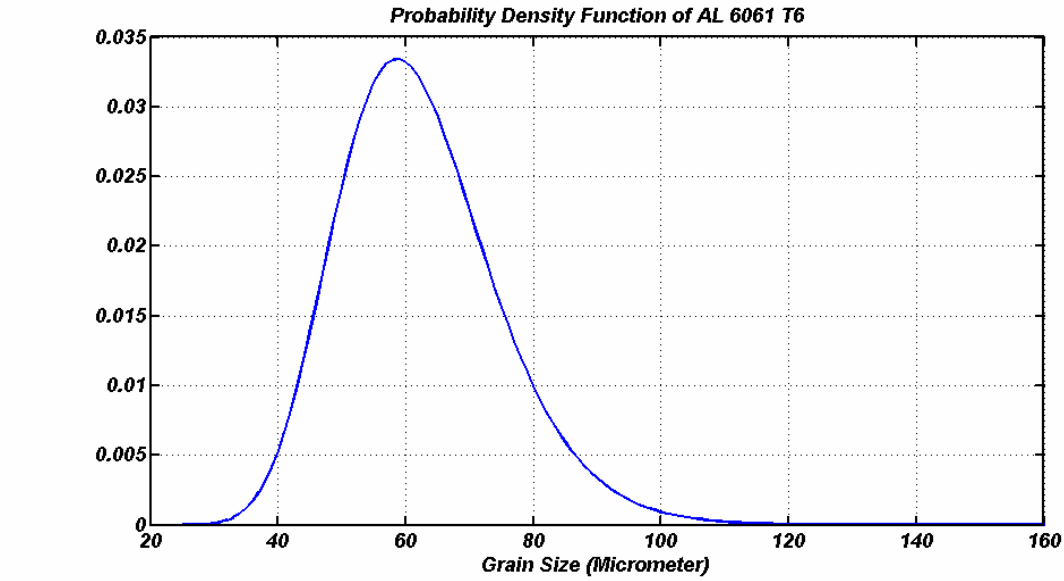

Figure 5-7: Extracted log-normal distribution of Al 6061 T6

5.3.2 Grain boundary misorientation of Al 6061 T6

The angle of misorientation represents a minimum angle relationship among adjacent crystallites. In the case of misorientation, Mackenzie[99] derived the analytical distribution of misorientation on the cubic structure, which gives an upper limitation of the misorientation angle as 62.8º in Figure 5-8.

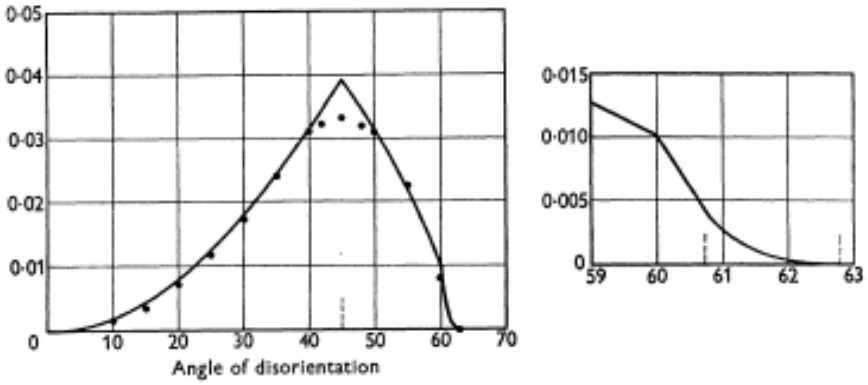

Figure 5-8: The density function for the angle of misorientation

Generally, an EBSD-inspired method has been used to capture the misorientation between the two crystals. Kang et al.[91] extracted the distribution of misorientation for Al 6061 T6 using EBSD. The values of misorientations are plotted as absolute values in Figure 5-9.

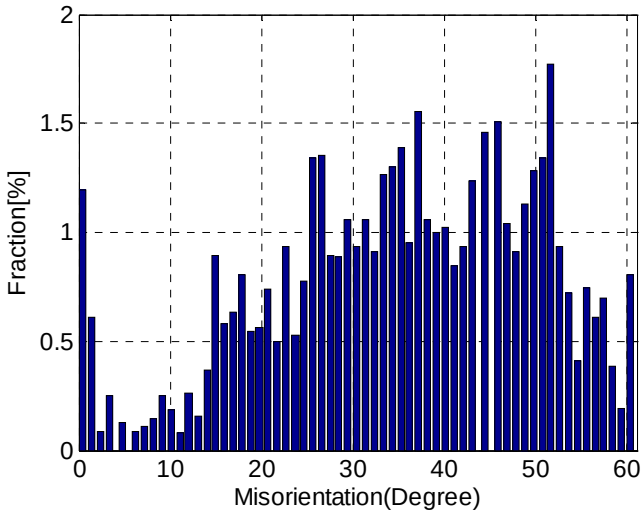

Figure 5-9: Grain boundary misorientation of AL 6061-T6 by Kang et al.[91]

The density function of misorientations is rescaled and becomes identical as the following:

$$\int_0^{\infty} p(\theta_{mis})d\theta = 1 \tag{5.8}$$

where θ_{mis} is the misorientation

So, the average misorientation angle, θ_{mis_av}, is approximated as

$$\theta_{mis\_av} = \int_0^{\infty} \theta_{mi}\, p(\theta_{mi})d\theta \tag{5.9}$$

Based on the above equations, the average angle of misorientation is 35.13º.

5.3.3 Contribution of the effects of microstructure

The material model representing the effects of microstructure is discussed in Chapter 3. Based on the key properties of Al 6061-T6 listed in Table 3-4 and the values of the average grain size and angle of misorientations, the contributions of the effects of microstructure are investigated. The breakdowns of the predictions of the overall forces based on the material model including the crystallographic effects are shown in Figure 5-10(a) and (b).

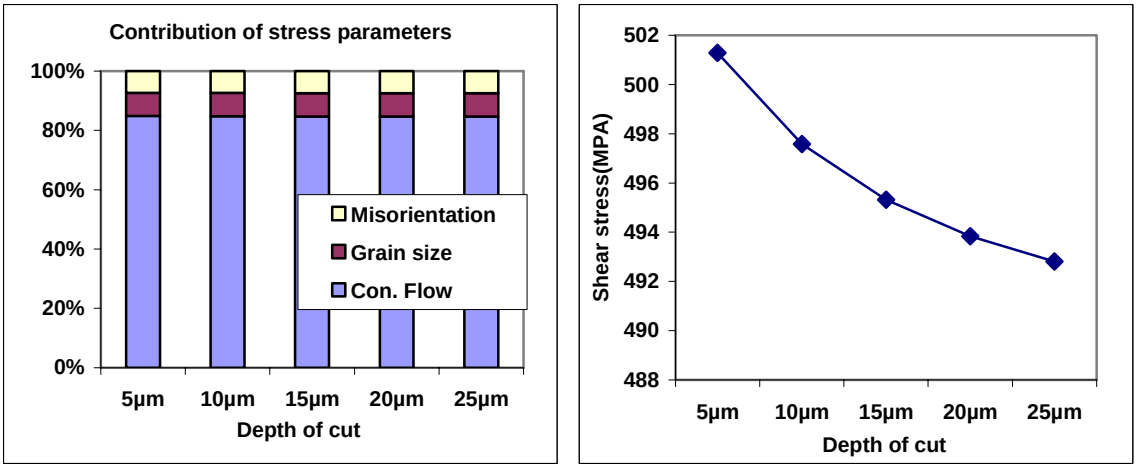

(a) (b)

Figure 5-10: (a) The breakdowns of shear stresses computed and (b) shear stress along depths of cut for $V_w = 1mm$, grit size=43µm, and $RPM = 60000rpm$

The values of constants used to compute the shear stresses are $k_m = 2$, $\alpha = 0.2$, $M = 3.0$, and $k_h = 32.5Hv\sqrt{\mu m}$ which are listed in Table 3-3. The computed results show that the computed-variation of the shear stress is around 15% of the overall shear stresses along depths of cut. The trend of the model behavior corresponding to the grain size is shown in Figure 5-11.

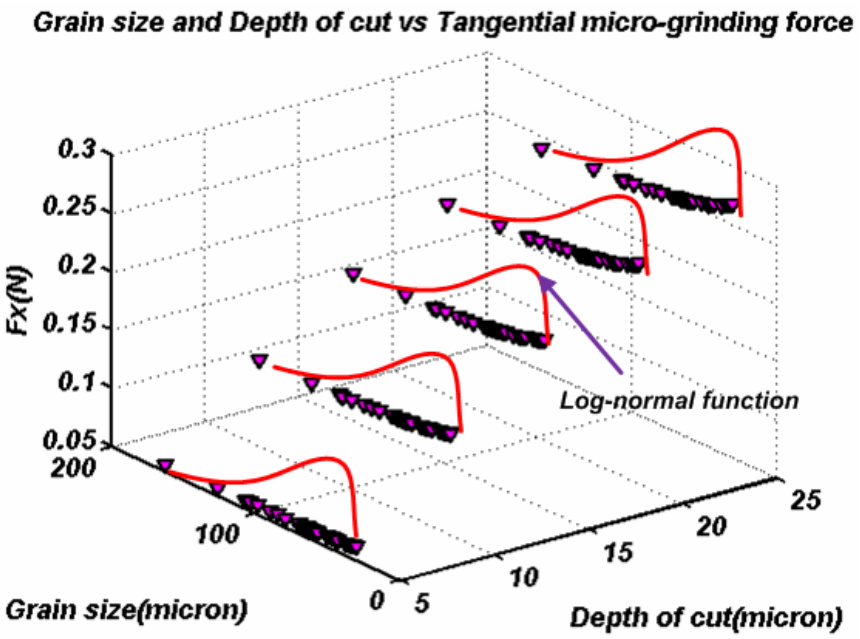

Figure 5-11: The trend of the model output for varying depths of cut and grain sizes

5.4 Experiment set-up of micro-grinding

The micro-grinding experiments were performed using a miniaturized machine tool shown in Figure 5-12(a). This miniaturized machine tool consists of five main subparts: a spindle, cutting tool, positioning stage, frame, and inspection device. The dimensions of this machine tool are $320\,x\,260\,x\,130mm$.

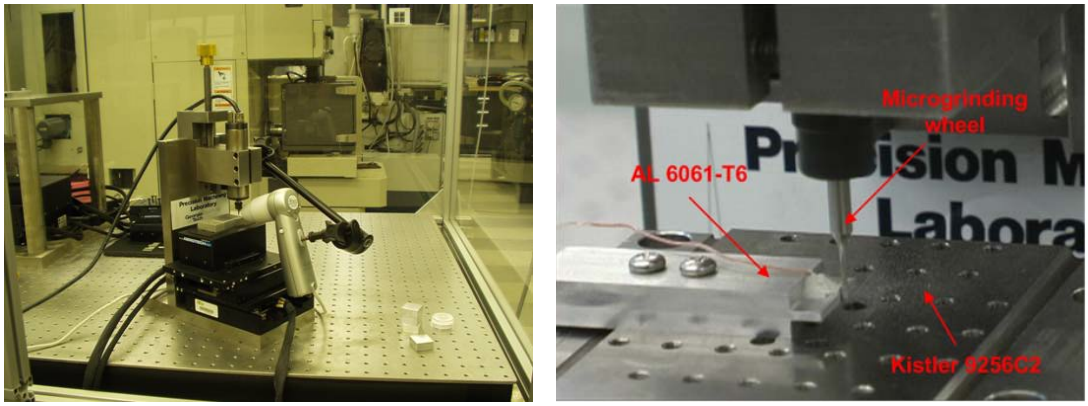

(a) (b)

Figure 5-12: Schematic of (a) a miniaturized machine tool and (b) Illustration of experiment configuration

The configuration of the micro-grinding experiment is shown in Figure 5-12(b). The main goal of this setup is to validate the comprehensive model discussed in Section 5.2.

In the experiments, to measure the forces created by micro-grinding, the Kistler 9256C2 MiniDyn is adopted because its weight is less than 4kg and its size is relatively small. That device is mounted between the workpiece and the positioning table. The model validation was conducted on the basis of comparing overall micro-grinding forces for different Electroplated CBN grinding wheels such as 85001-BM, 85002-BM, and 85003-BM. The detail view of the experimental setup for surface grinding is illustrated in Figure 5-13.

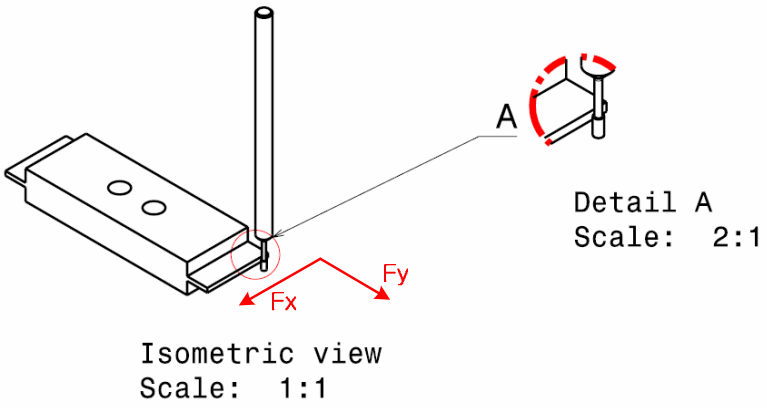

Figure 5-13: Detail schematic of surface micro-grinding

On the preliminary experiment, the micro-grinding forces were measured using the above mini-dynamometer. A pure output signal of the micro-grinding fluctuates widely due to the vibration of the spindle. FFT analysis of sections 1 and 2 is performed to identify the frequency range of the force signals created by micro-grinding because the vibration of a spindle rotating with high rpm produces noise in the force signal in Figure 5-15(a) and (b). The results show that the vibration of the spindle rotating with 60,000rpm has 1000 Hz, and the frequency of the micro-grinding force signal is below 200 Hz.

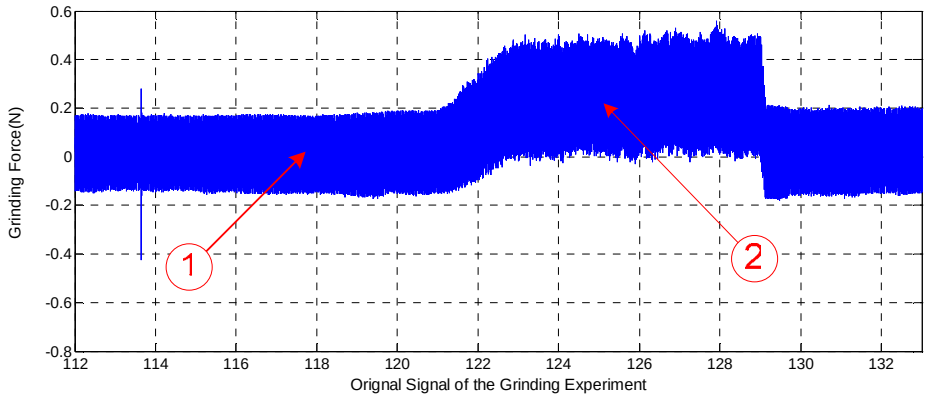

Figure 5-14: Pure force signal for 20µm depth of cut and spindle RPM 60000rpm

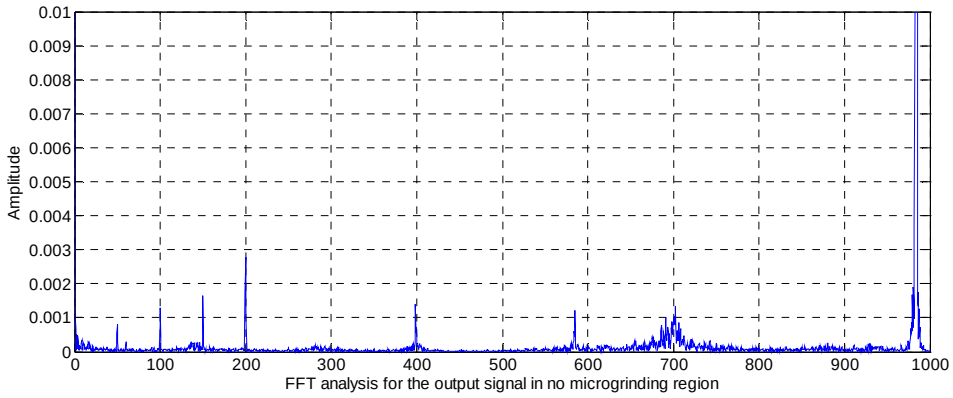

(a)

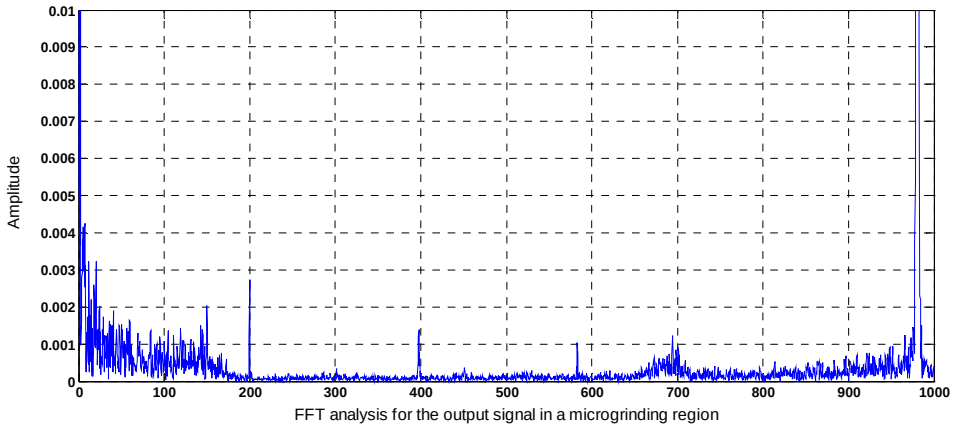

(b)

Figure 5-15: FFT analysis of (a) section 1 and (b) section 2 in Figure 5-14

Based on the preliminary experiment, all the measurements were filtered with a low-pass filter that blocked the noise of the spindle's high rotational speed. The signals filtered are shown in Figure 5-16.

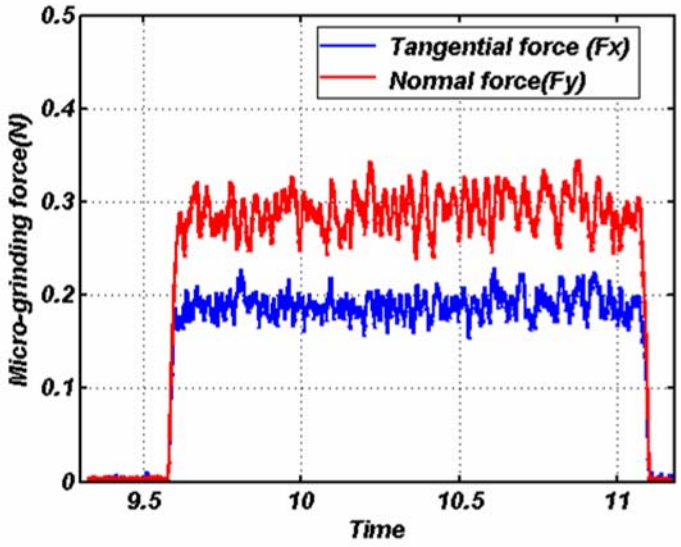

Figure 5-16: Experimental data of the micro-grinding forces at 60000rpm and 20µm depth of cut

5.5 Sensitivity analysis of experimental data

A sensitivity analysis of micro-grinding process parameters is performed to investigate the effects of process parameters on the variation of experiment outputs. Three model inputs chosen in this sensitivity analysis are the micro-grinding wheel size, feedrate and spindle RPM. The Taguchi method with a three level is adopted to determine the effects of the factors chosen. The levels for each factor are listed in Table 5-2. Through the experiment, depth of cut is held constant at 15µm. The experiment results of cases1-9 are shown in Figure 5-17.

Table 5-2: L9 orthogonal matrix of the Taguchi method

	Wheel size(mm)	RPM	Feedrate(mm/min)
case1	0.75	40000	300
case2	0.75	50000	400
case3	0.75	60000	500
case4	1	40000	400
case5	1	50000	500
case6	1	60000	300
case7	1.25	40000	500
case8	1.25	50000	300
case9	1.25	60000	400

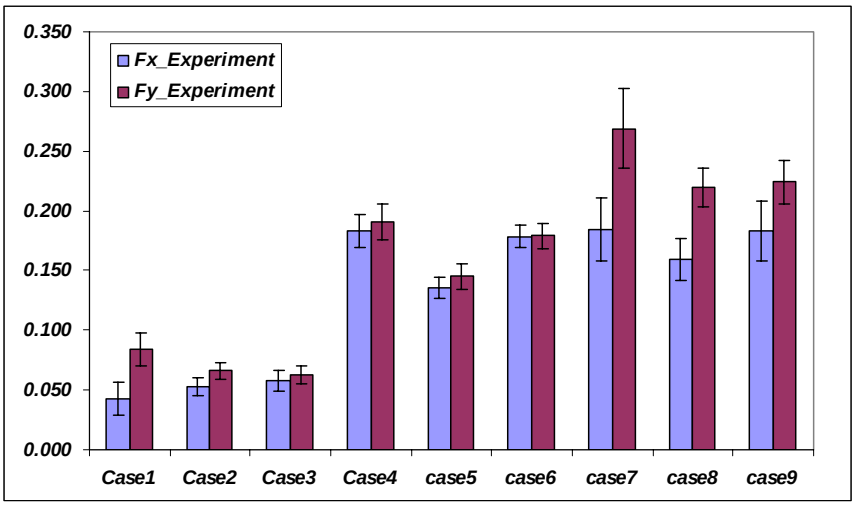

Figure 5-17: Normal and tangential forces for cases1-9

The plots of the main effects for normal (Fy) and tangential (Fx) forces are shown in Figure 5-2(a) and (b). The results show that the predictions of micro-grinding forces in this model are strongly influenced by the grinding wheel size in the range of inputs for both forces. The spindle rpm also affects the predictions of these forces. But, the feedrate shows a minor effect compared to other parameters because the range of inputs is small.

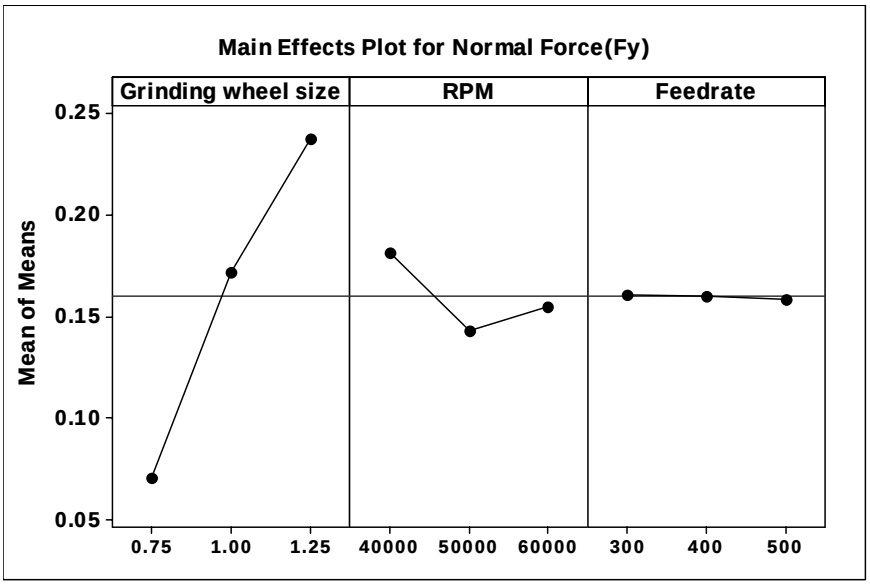

(a)

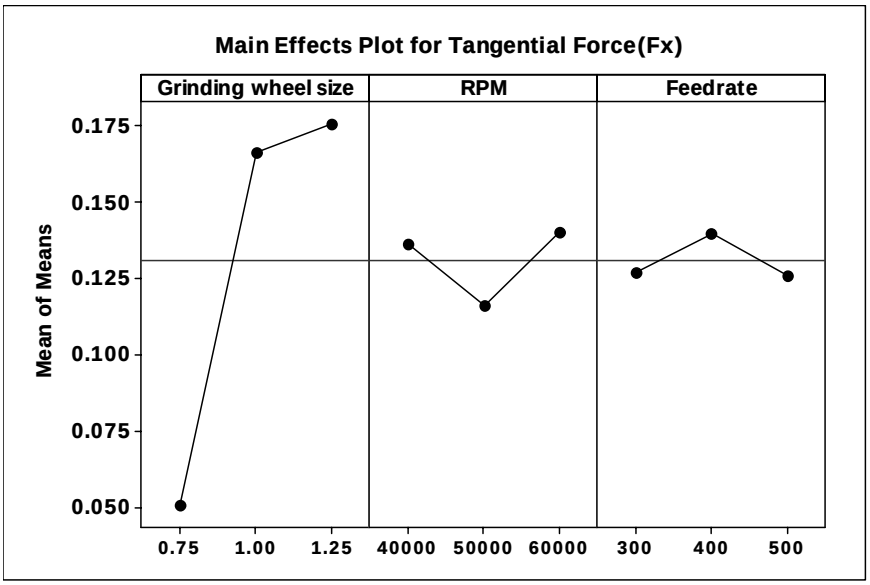

(b)

Figure 5-18: Main effect plot of (a) normal forces and (b) tangential forces

5.6 Model validation

The new analytical model of the individual grit interaction can be extrapolated to all grits on the grinding wheel surface. The average values of the grit size for the micro-grinding wheel engaged in the experiments are 41μm for the worn tool and 44μm for the fresh tool, as discussed in Chapter 4. In this study, the active grit density for the electroplated CBN grinding wheel for different feedrates is experimentally obtained from the direct method in Chapter 4. The regression results of the dynamic cutting edge density are listed in Table 4-3.

Based on the experimental configuration, experimental data for micro-grinding were collected for varying depths of cut, feedrates, and three different micro-grinding wheels. A sample of the experimental results is shown in Figure 5-19. Two experiments for each depth of cut for given conditions were performed and averaged linearly.

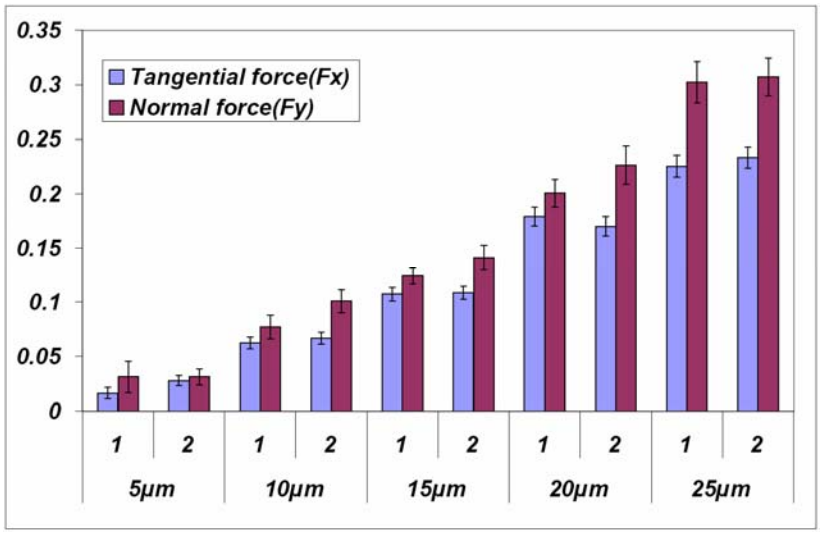

Figure 5-19: Micro-grinding forces for varying depths of cut for $V_w = 1mm/\sec$

5.6.1 Identification of parameter effects

The comparisons of normal and tangential forces for varying feedrates are shown in Figure 5-20(a) and (b). The results show that the magnitudes of the forces in $V_w = 10mm/\text{sec}$ and $V_w = 30mm/\text{sec}$ are higher than those seen in Vw=1 mm/sec. The differences between the results obtained at these speeds are around 50% for tangential forces and 50~80% for normal forces. The gap between the results obtained at these speeds increases at high depths of cut. But, deviation between results obtained at higher feedrates such as $V_w = 10mm/\text{sec}$ and $V_w = 30mm/\text{sec}$ is around 2-3% at low depths of cut. As the depth of cut increase, that gap increases to around 12%.

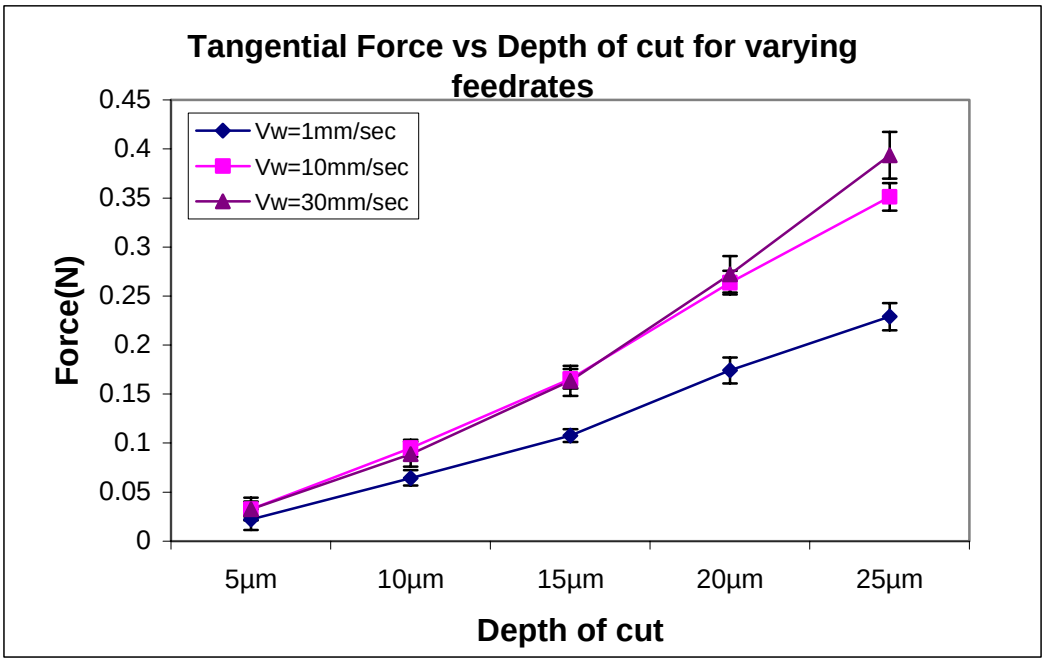

(a)

Figure 5-20: Comparisons of (a) tangential and (b) normal forces for varying feedrates

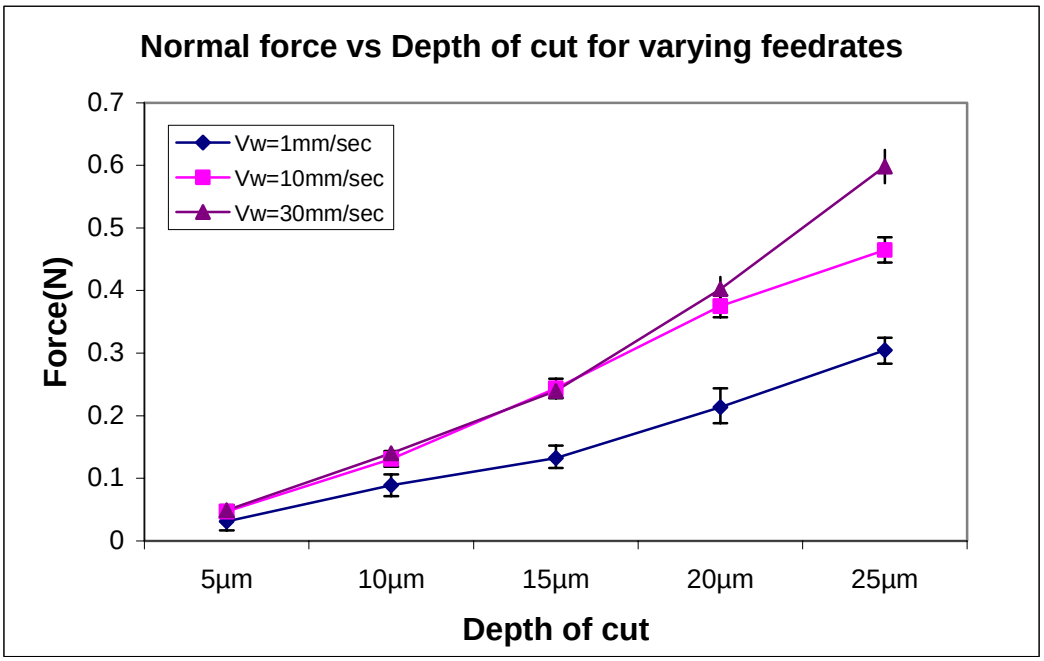

(b)

Figure 5-20: Continued

The comparisons of normal and tangential forces for different micro-grinding wheels are shown in Figure 5-21(a) and (b).The results show that as the size of the micro-grinding wheel increases, the normal and tangential forces of micro-grinding increase.

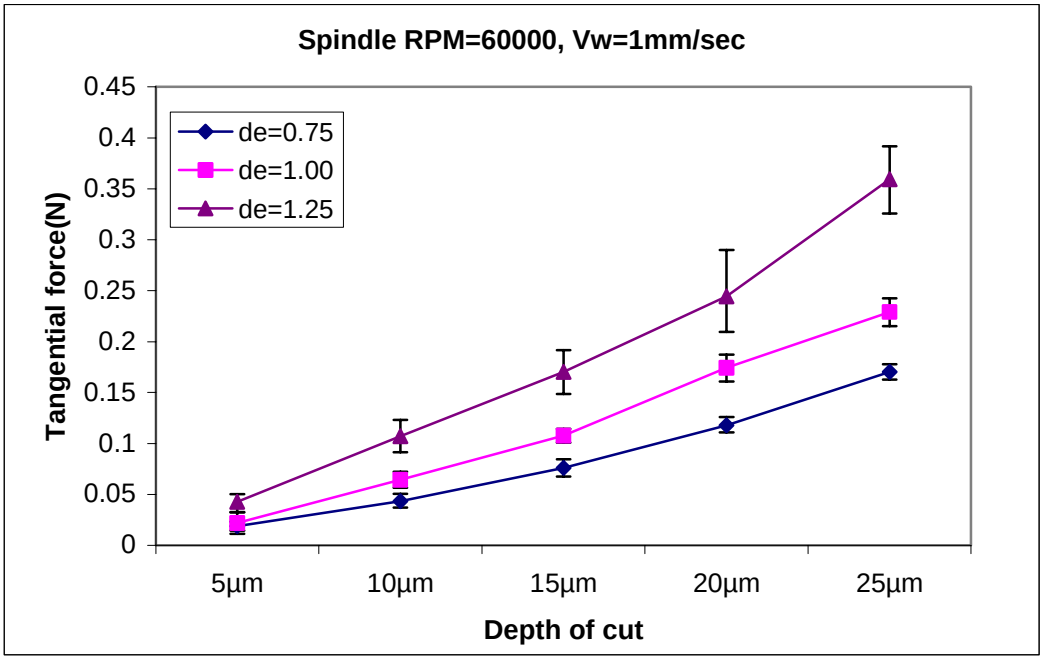

(a)

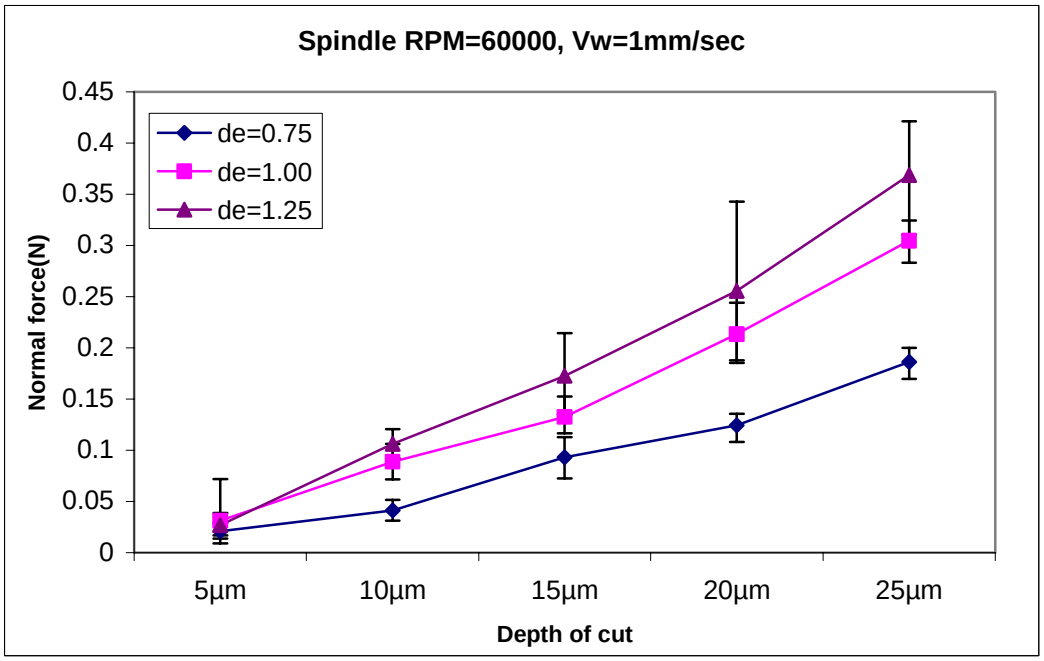

(b)

Figure 5-21: Comparisons of (a) tangential and (b) normal forces for different sizes of the micro-grinding wheel

The increase of normal and tangential forces is more pronounced at higher depths of cut. It seems that the increase of the size of the micro-grinding wheel leads to increases in the geometry contact length and cutting speed as well as the static stiffness of the micro-grinding wheel. It is also observed that the increasing trend of force components is changed. For example, in the case of $d_e = 1.00mm$, the normal and tangential forces increase by15~30% and 30~50% with respect to $d_e = 0.75mm$. For $d_e = 1.25mm$, the normal and tangential forces increase by30~50% and 16-24% with respect to $d_e = 1.00mm$.

5.6.2 Comparisons between experiment data and predictions

The predictions of the micro-grinding forces were performed on the basis of the comprehensive model described in section 5.2. The parameters used in these predictions are obtained in Chapters 4 and 5 and listed in Chapter 3. In these computations, two methods:(1)the Oxley's model[82] and (2)Manjunathaiah and Endres model[83] are used to compute strains and strain rates of the proposed material model in Chapter 3 and compared with experimental data.

The comparisons of normal and tangential forces obtained using different size micro-grinding wheel are shown in Figure 5-20 and Figure 5-21.

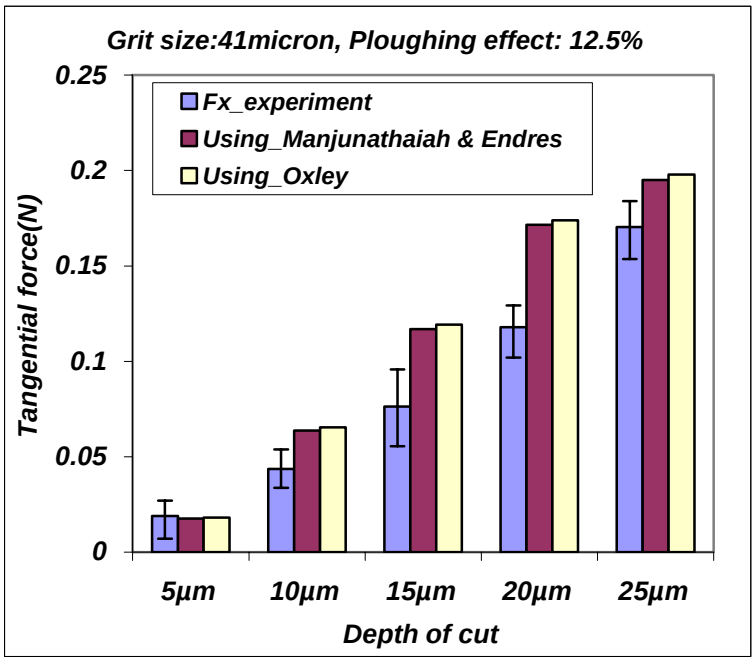

(a)

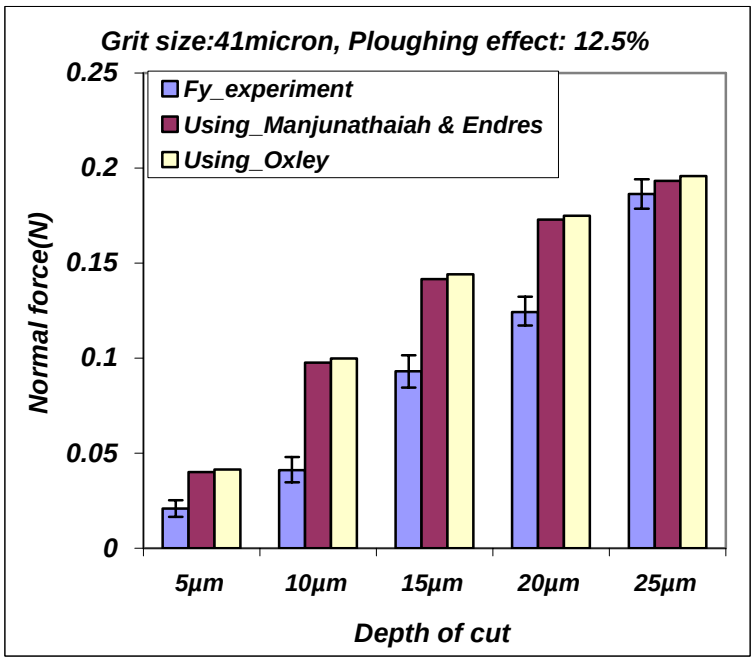

(b)

Figure 5-22: Comparison between experimental data and predictions for (a) tangential (Fx) and (b) normal forces (Fy) of 85001-BM ($d_e \approx 0.75mm$) for $V_w = 1mm/\sec$

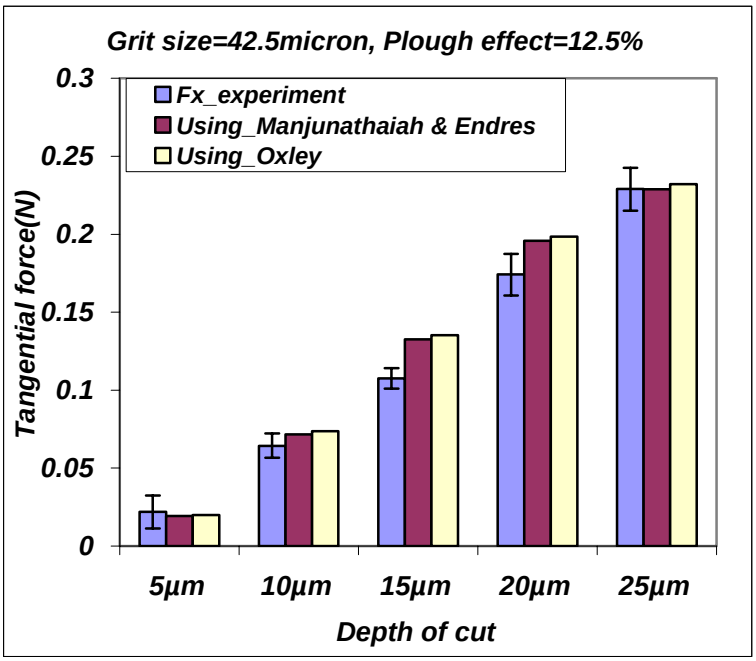

(a)

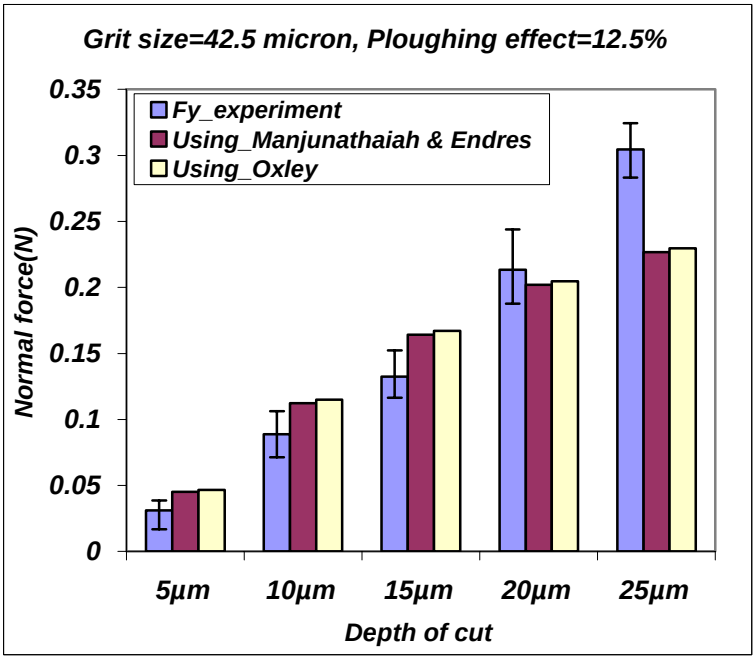

(b)

Figure 5-23: Comparison between experimental data and predictions for (a) tangential (Fx) and (b) normal forces (Fy) of 85002-BM ($d_e \approx 1.00mm$) for $V_w = 1mm/\sec$

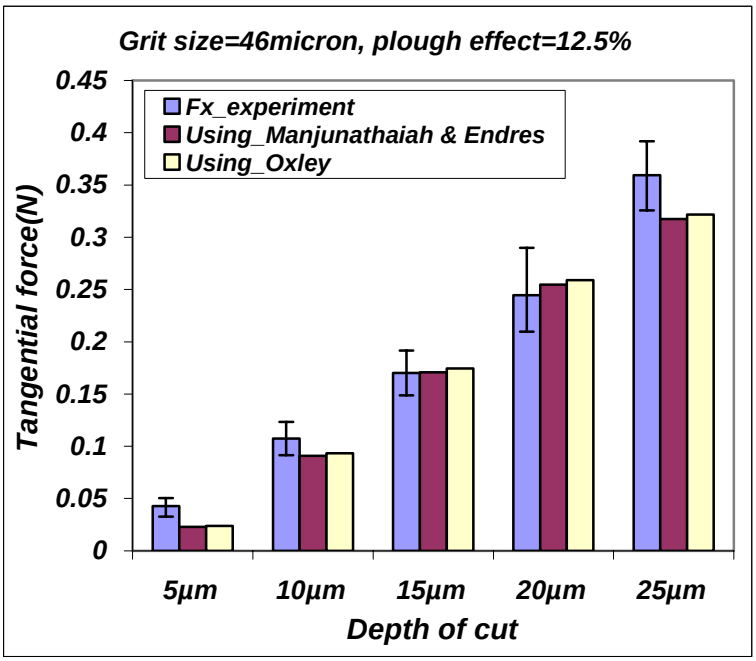

(a)

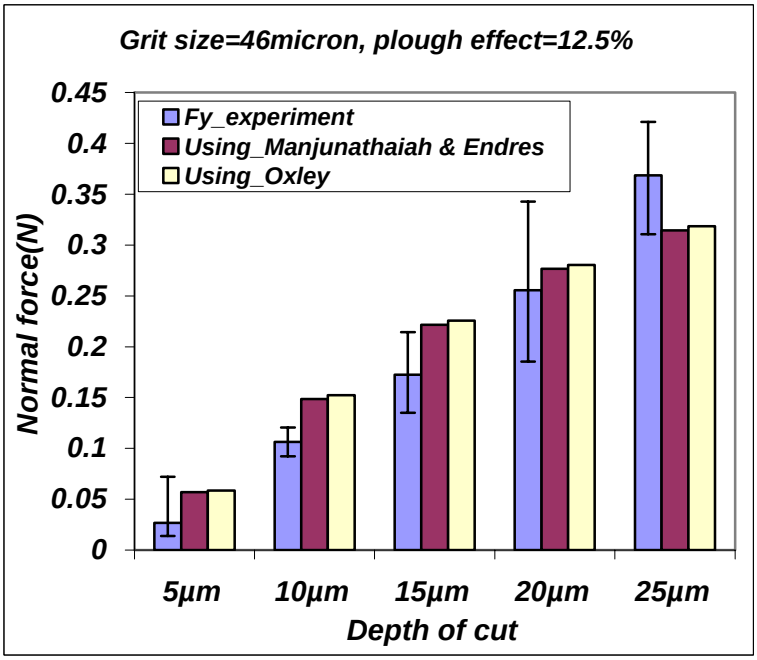

(b)

Figure 5-24: Comparison between experimental data and predictions for (a) tangential (Fx) and (b) normal forces (Fy) of 85003-BM ($d_e \approx 1.25mm$) for $V_w = 1mm/\text{sec}$

It is observed that many predictions along varying depths of cut are larger than the experimental data of micro-grinding. The predicted micro-grinding forces in the x-direction for 85002-BM show good agreement with experimental data in Figure 5-23(a). The maximum deviation between the measured forces and predictions is less than 23%. In the case of 85001-BM and 85003-B, the predictions show reasonable agreement with experimental data. The results also show that the maximum deviation between these two methods computing strain and strain rate is less than 3%.

But, in the y direction, the predictions capture the trend of increasing forces for increasing depth of cut. But, most predictions of this model are higher than those obtained in experiments. In other view, the amount of error decrease as depth of cut increases in both cases. Based on the comparison, the average deviations which the model provides are around 33% for 85001-BM, 12% for 85002-BM, and 16% for 85003-BM in the tangential force direction and around 65% for 85001-BM, 25% for 85002-BM, and 41% for 85003-BM in the normal force direction. Since the magnitude of the measured forces is less than 1N, the percentage of the errors is relatively high.

The comparisons of predictions and measured forces under high feedrates are shown in Figure 5-25 and Figure 5-26. In the case of $V_w = 10mm/\sec$, the predictions of the tangential force and the experimental data are close except for the case of 5μm depth of cut in the tangential direction. But, although the predictions of the normal force capture the trend of increasing forces for increasing depth of cut, the predictions are underestimated at low depths of cut.

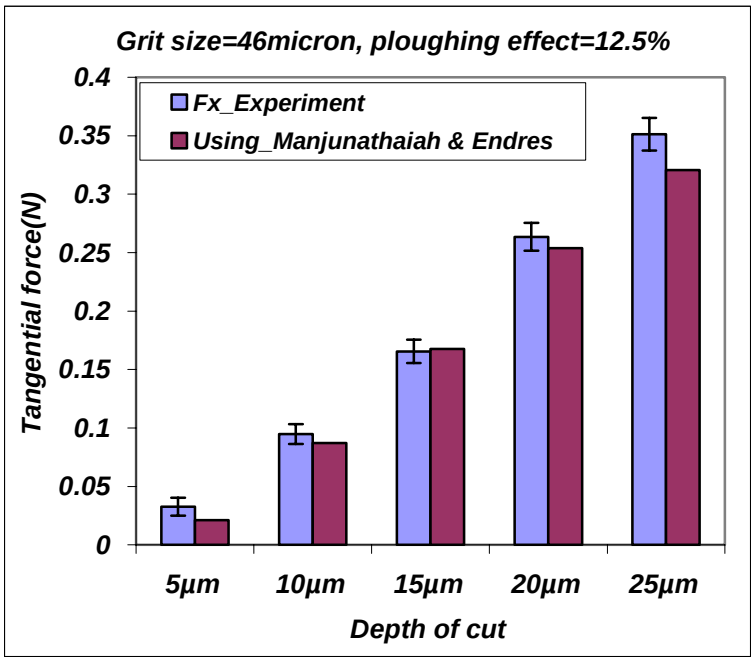

(a)

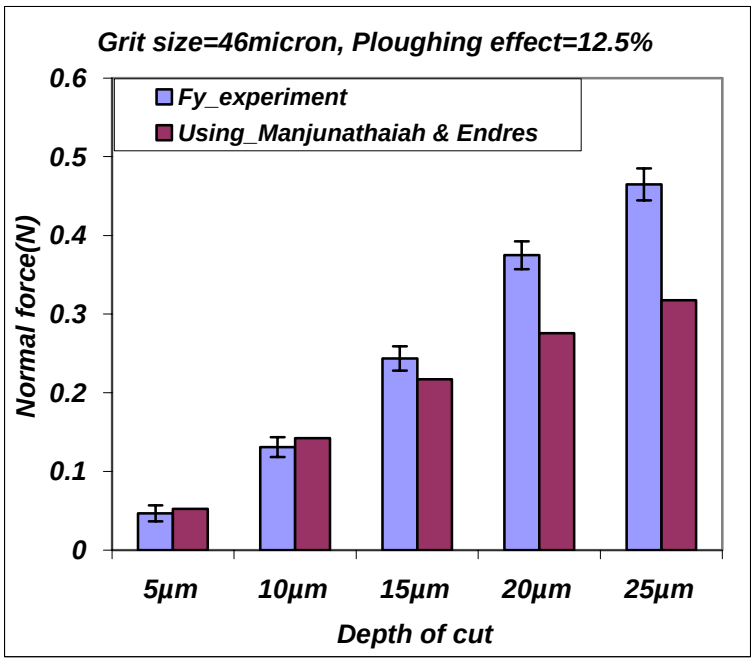

(b)

Figure 5-25: Comparison between experimental data and predictions for (a) tangential (Fx) and (b) normal forces (Fy) of 85002-BM ($d_e \approx 1.00mm$) for $V_w = 10mm/\text{sec}$

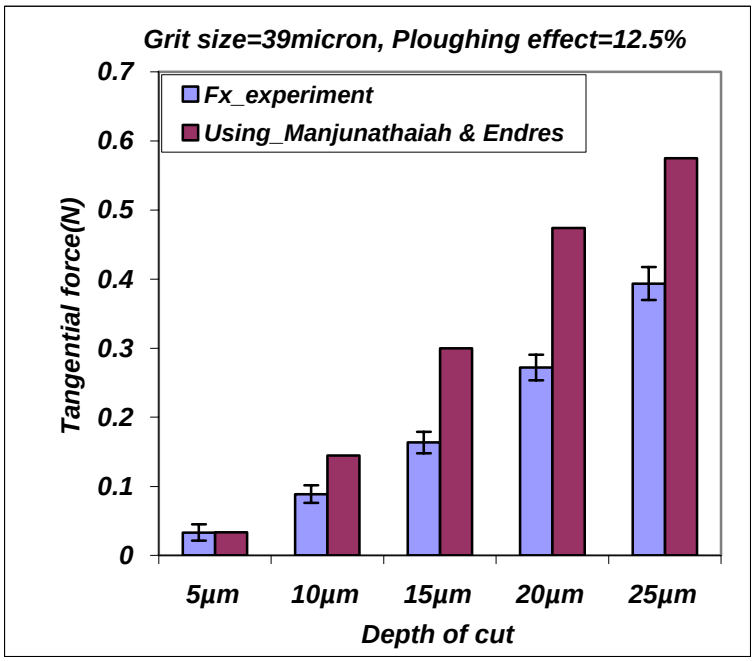

(a)

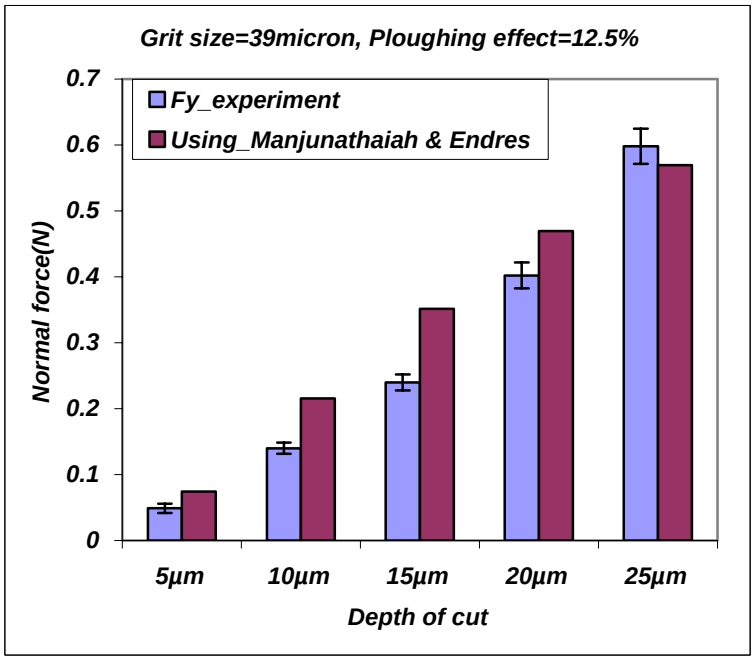

(b)

Figure 5-26: Comparison between experimental data and predictions for (a) tangential (Fx) and (b) normal forces (Fy) of 85002-BM ($d_e \approx 1.00mm$) for $V_w = 30mm/\text{sec}$

The experimental results of $V_w = 30mm/\text{sec}$ show the opposite trend compared to $V_w = 10mm/\text{sec}$ in Figure 5-26. It is found that experimental data and predictions in the normal direction are close at higher depth of cut. But, the overall predictions in both directions are overestimated compared to the values obtained for low feedrates.

The errors in these comparisons may come from the following: (i) the effect of the trapped chips and (ii) the rigidity of the micro-grinding wheel. During micro-grinding, some chips created are trapped within the space between grits. These trapped chips can prevent the engagement of other grits in micro-grinding. Otherwise, these chips can be involved in micro-grinding. So, the dynamic cutting edge density may be different from the results obtained in Chapter 4. The other source of the errors is the stiffness of the micro-grinding wheel. Since the size of the micro-grinding tool is small, there is elastic deflection during micro-grinding. Due to this deflection, vertical grinding may not be ensured during the experiments.

5.6.3 Assessment of the effects of temperature

Figure 5-27 shows the temperature rise with respect to the depth of cut. This temperature rise on the shear band is estimated from the predicted micro-grinding forces. It is observed that the temperature rise is not significantly greater than that observed during the conventional grinding process. In micro-grinding, the magnitude of forces is generally below 1N so that the generated heat source is small. Besides this effect, the workpiece (Al 6061-T6) has a large heat conductivity compared to other materials. So, these phenomena are attributed to the lower temperature rise. But, for hard materials, the temperature rise becomes more significant.

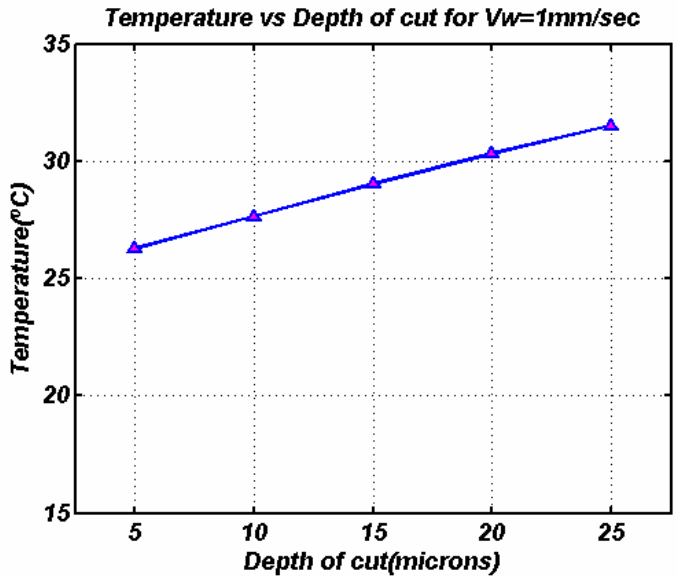

Figure 5-27: Temperature rise on the shear plane accord to the depth of cut for 60000rpm and $V_w = 1mm/\sec$

5.7 Summary

In this chapter, a comprehensive model for the prediction of micro-grinding forces was presented. The single grit interaction and temperature models in Chapter 3 and the micro-grinding wheel topography in Chapter 4 are integrated in this comprehensive model.

To proceed to computations, the average grain size was experimentally obtained and the contribution of the microstructure to the overall shear strength was presented. A sensitivity analysis of the model behavior for changing parameters was performed using the Taguchi method. The results show that the size of grits strongly influences the outputs of this model. The size of the micro-grinding wheel and the ploughing effect also

influence the results. A sensitivity analysis of experimental outputs shows that the size of the micro-grinding highly influences the variation of outputs

This model was validated by comparing the predictions of the micro-grinding forces with the experimental data for different micro-grinding conditions. The comparisons between them show that the predictions driven by this model capture the trend of the experimental data. For $V_w = 1mm/\text{sec}$ and 85002-BM, the model provides good agreement with the experiments, as it has a maximum deviation of 25%. In addition, the temperatures predicted in this model were reasonable for input conditions used in this analysis.

CHAPTER 6

MULTI-OBJECTIVE OPTIMIZATION OF MICROSCALE MACHINE TOOLS

6.1 Introduction

The inherent technical and economical advantages of the above research have motivated the development of various prototypes of miniaturized machine tools[4, 5, 9, 100, 101, 102]. These tool prototypes' ability is successfully to fabricate microscale parts. However, there have not been enough studies for design of miniaturized machine tools and as a result, little design knowledge and experience base concerning miniaturization of these systems has been accumulated. Several attempts to optimize systematically miniaturized machine tools have been unsuccessful. In order to provide guidance for further development, studies of a systematic design of these systems are necessary.

In design of traditional and miniaturized machine tools, a conceptual design stage for all major elements is important. This step defines the basic features and capabilities of traditional and miniaturized machine tools. In the case of miniaturized machine tools, this design stage acquires more importance because the ratio of the overall size of a miniaturized machine tool to its target products is significantly smaller than that of traditional machine tools. The conceptual design for miniaturized machine tools has to be accompanied with comprehensive analyses of possible effective factors such as static, dynamic, and thermal stiffness, machine accuracy, and machine working volume.

This chapter presents the work for optimization of a machine structure size according to varying sizes of the miniaturized machine tool. In this study, theoretical and

FEM modeling and experimental analysis of possible design parameters for use in development of miniaturized machine tools is pursued, supplemented by experimental analysis based on a hammer impact test. Three different sizes of machine tool structures are studied in order to identify the variation trend of design parameters as a function of a miniaturized machine tool size. As an indicator of the dynamic characteristics, the 1st natural frequency and the damping ratio are experimentally measured to model the dynamic properties of the joints within the miniaturized machine tool. As a result, the trend of the dynamic behavior of the miniaturized machine tool can be theoretically modeled, which provides the basis for optimal dimensioning of minimized manufacturing equipments at the design stage. Finally, the proposed design model in Figure 6-1 is applied to optimization of the miniaturized milling machine in Figure 6-4.

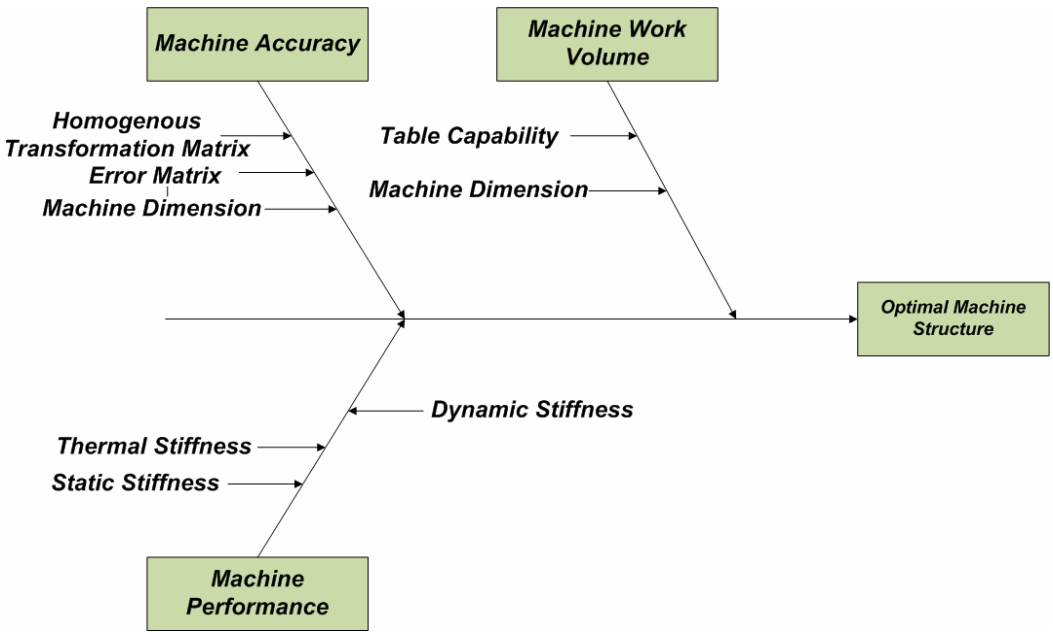

Figure 6-1: Proposed design strategy

The following sections provide the theoretical and FEM evaluation of the miniaturized machine tool's structural performance in terms of static, thermal, and dynamic stiffness. This is followed by computations of volumetric error and machine work volume according to different machine sizes. Finally, optimization for the developed miniaturized milling machine is carried out and a comparison between analytical and FEM computation is performed.

6.2 Structural performance evaluation

Machine tool's structure consists of stationary and moving parts. The design of a machine structure is an important decision step; it requires consideration of many aspects of various products because the structure provides the means by which all components such as spindles and positioning table are brought together. It is challenging because existing sources of uncertainty, such as errors due to geometric configuration, thermal deformation errors, and errors induced by load, affect a machine's final performance. In order to provide more reliable machine performance and better product quality, some key factors such as static, thermal, and dynamic stiffness, machine accuracy, and machine working volume have to be considered at a conceptual design stage.

6.2.1 Static stiffness evaluation

The structure of a miniaturized machine tool experiences external force during machine operation and these forces can create the deflection of the machine structure.

This deformation affects the machine's accuracy. In this study, the complex miniaturized machine tool is simplified into a cantilever beam with an intermediate load and moment in Figure 6-2 because the overall configuration of miniaturized machine tools is relatively simple compared to conventional machine tools. The model studied here includes a sliding constraint in the joint of the computed model, which induces the loss of moment transmission at the joint.

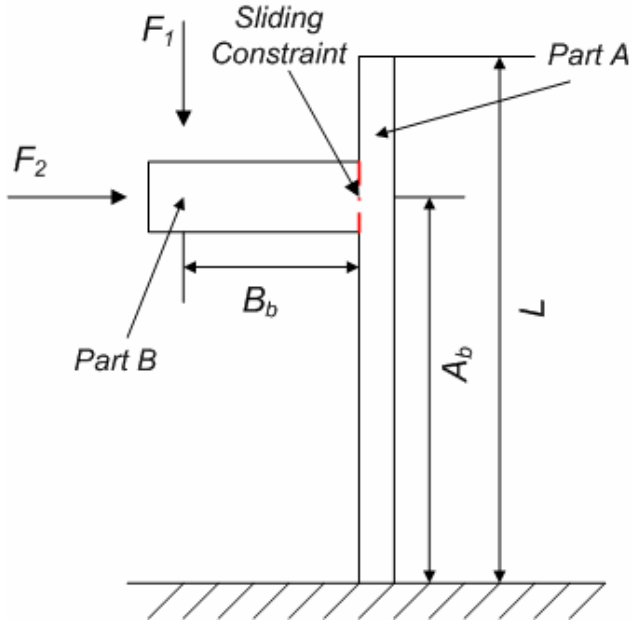

Figure 6-2: Simplified machine structure model

Assuming that the magnitudes of F_1 and F_2 are equal, the static stiffness of the miniaturized machine can be expressed as:

$$K_{static\_stiff} = \frac{6EI}{A_b^2(2A_b - 3C_{loss}B_b)} \tag{6.1}$$

where A_b and B_b are machine dimensions, C_{loss} the moment loss, E the modulus of elasticity, and I the moment of inertia.

The computed results of static stiffness for this miniaturized machine tool are shown in Figure 6-3(a).

6.2.2 Thermal stiffness evaluation

In miniaturized machine tools, if the ambient temperature is stable, the main heat source is the operating spindle with a high RPM. The temperature variation of the miniaturized milling machine is observed to be around 12º during machine operation using thermal couple data collected at different locations. The spindle is assembled at part B in Figure 6-2. So, with the assumption that the temperature rise is equally distributed, thermal stiffness that is related to the change in a machine linear dimension can be obtained as:

$$K_{thermal} = \frac{1}{\alpha_t B_b} \tag{6.2}$$

where α_t is the thermal expansion coefficient.

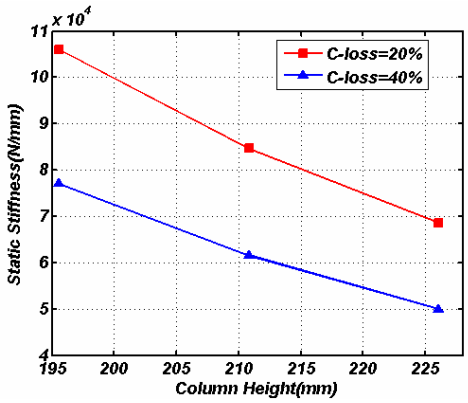

(a)

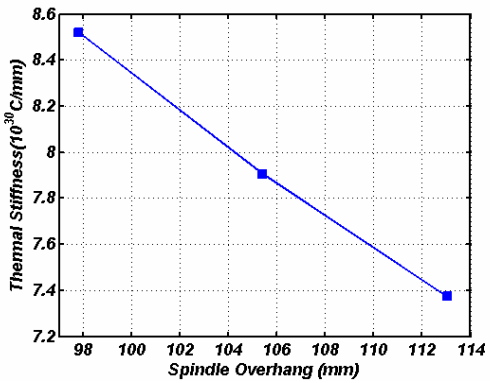

(b)

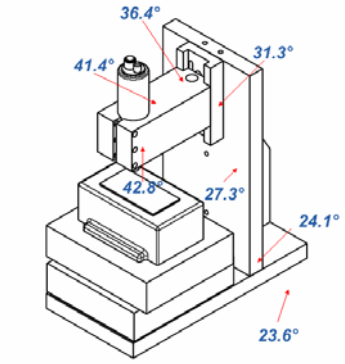

(c)

Figure 6-3: (a) Static and (b) Thermal Stiffness of the miniaturized milling machine, and (c) temperature distribution during machine operation

The material selected in this study is Invar 36 steel alloy with the thermal expansion coefficient of $1.2\times10^{-6}/^{o}C$. On the basis of the above equation, the results of thermal stiffness according to a machine size are shown in Figure 6-3(b).

6.2.3 Dynamic characteristic evaluation

In the case of miniaturized machine tools, the high speed spindle rotation with high speeds causes severe vibrations that decrease machine accuracy and affect product quality. Computations of the structural dynamic behavior of miniaturized machine tools are necessary to ensure their stable operation with proper relative displacement between the tool and the workpiece. General methods for characterizing the dynamic behavior of machine tools are the lumped parameter method and the finite element analysis of modules. In view of the enumeration of various machine sizes, a lumped parameter model is preferred, as is relatively simple with respect to FEM analysis.

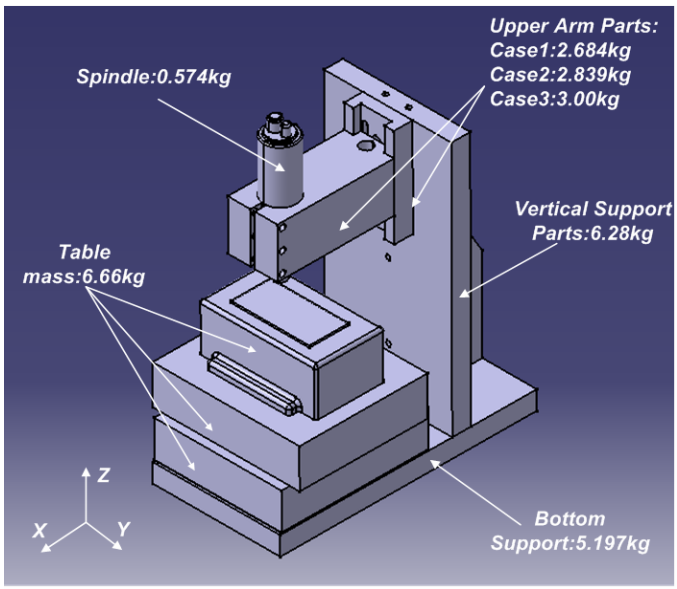

Figure 6-4: Machine configuration and masses of machine components

In the lumped parameter model, a miniaturized machine is assumed as an assembly of modules connected by joints which are modeled as springs and dampers. In this study, although the miniaturized milling machine consists of many components, it is assumed as a three degree of freedom mass system for the purpose of simple modeling in Figure 6-5. The masses of the main machine components used in this model are measured and shown in Figure 6-4. The governing equation describing the motion of a multi-degree of freedom system with viscous damping is given by:

$$[M]\{\ddot{x}\}+[C]\{\dot{x}\}+[K]\{x\}=\{f\} \tag{6.3}$$

where $[M]$ is the mass matrix, $[C]$ is the damping matrix, and $[K]$ is the joint stiffness matrix.

Assuming that a solution of the displacement is the harmonic motion, the receptance matrix, with substitution of this assumed displacement into the above equation, will be:

$$[G(w)]=\frac{1}{[K]-\omega^2[M]-j\omega[C]} \tag{6.4}$$

where $[G(w)]$ is the receptance matrix and ω is the rotational frequency.

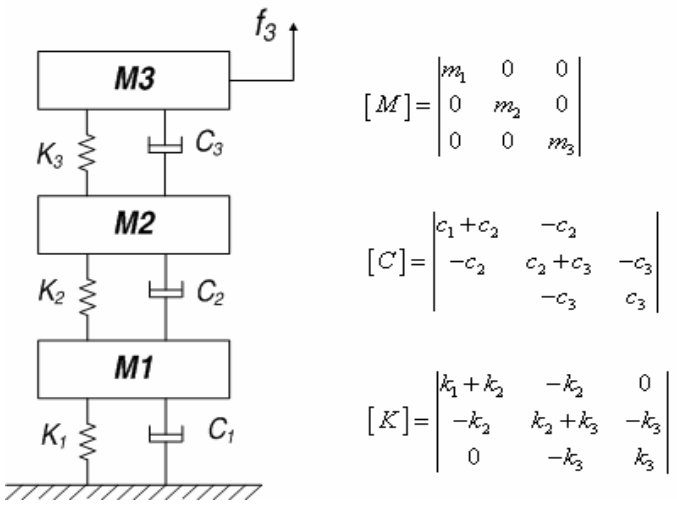

Figure 6-5: Three degree of freedom lumped parameter model

A classic approach for solving the above equation is the modal superposition. The natural frequencies of this system can be computed in this way. At the design stage, the development of the damping matrix is not straightforward because it is hard to assume certain values. In this case, the Rayleigh damping theory of Clough and Penzien[103] is used, in which it is assumed that the damping matrix is proportional to the mass and stiffness matrices. The standard Rayleigh damping model is given by

$$[C] = \alpha_R [M] + \beta_R [K] \tag{6.5}$$

where α_R and β_R are coefficients for the mass and stiffness.

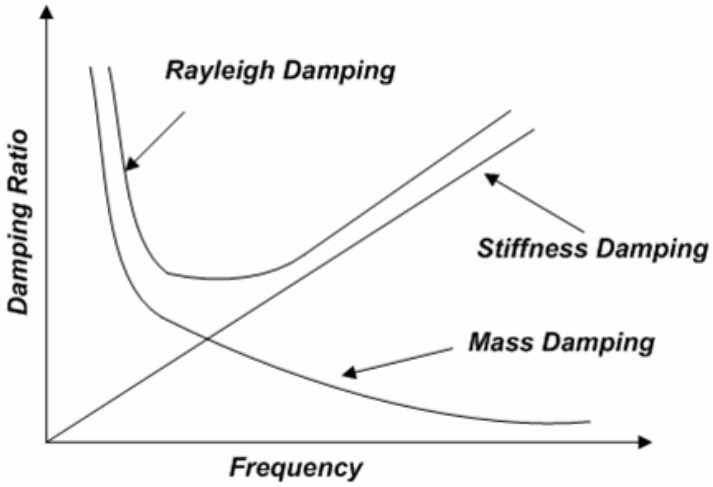

Figure 6-6: Contribution of Rayleigh damping parameters

Based on this theory, the damping coefficient in mode i can be expressed as:

$$\xi_i = \frac{\alpha_R}{2\omega_{ni}} + \frac{\beta_R \omega_{ni}}{2} \tag{6.6}$$

where ξ_i is the damping ratio and ω_{ni} is the rotational frequency in mode i.

However, the parameters of the springs and the coefficients of this damping model need to be identified. Therefore, the analytical computation of a lumped parameter model has to be supplemented by experimental analysis such as a hammer impact test.

6.3 Experimental analysis

The machine configuration studied here is the knee and column type vertical milling machine shown in Figure 6-7 where A_b is the column height, B_b the spindle overhang, C_b the spindle protrusion. In order to identify the above described parameters of this machine configuration, a classic hammer impact test is engaged to investigate the

machine's structural dynamic behavior experimentally for the three different dimensions that are listed in Table 6-1.

Table 6-1: Dimensions of the miniaturized milling machine

	A_b(inch(mm))	B_b(inch(mm))	C_b(inch(mm))
Case 1	7.7(195.8)	3.85(97.91)	3(76.2)
Case 2	8.3(211.1)	4.15(105.5)	3(76.2)
Case 3	8.9(226.3)	4.45(113.2)	3(76.2)

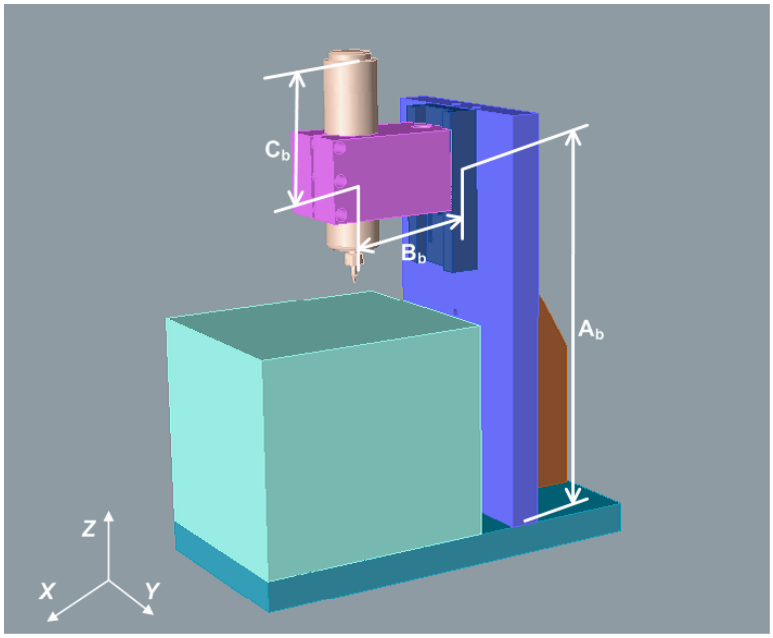

Figure 6-7: Illustration of the miniaturized milling machine with variable dimensions

On the preliminary test, when the spindle rotates with a maximum spindle RPM (60,000rpm), the dynamic properties of the machine structure are observed without machining. In the experiment, light weight accelerometers (Kistler 8630C50) having a 6 kHz frequency range are attached at the locations shown in Figure 6-9(a). Since the mass

of this accelerometer is much smaller than that of the miniaturized machine tool, the mass effect of these sensors can be neglected in the analysis of experiment data.

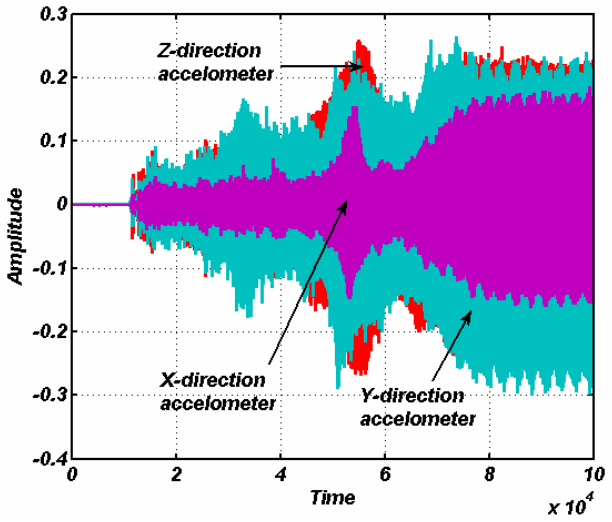

(a)

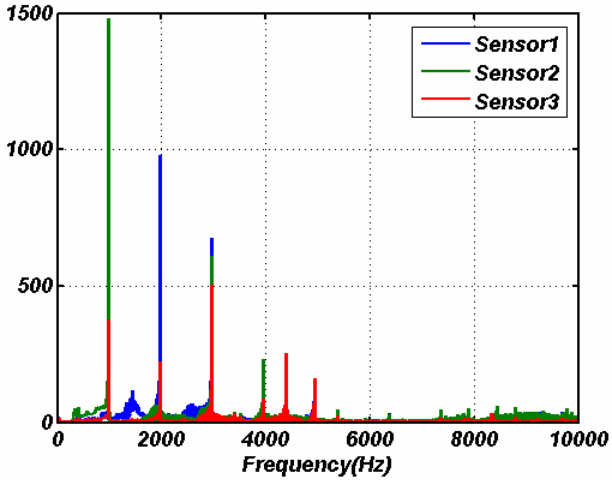

(b)

Figure 6-8: (a) Original shape and (b) FFT analysis of output signals from accelerometer sensors in case 1

It is observed that the magnitude of the output signal in the Y direction is largest among output signals in Figure 6-8(a). As in Figure 6-8(b), the major peaks in the fast fourier transform (FFT) analysis of these measured signals are around 1000Hz, 2000Hz, and 3000Hz, which are related with the spindle rotation speed. Therefore, the dynamic characteristic of the miniaturized machine tool in the Y direction is more important compared to other directions.

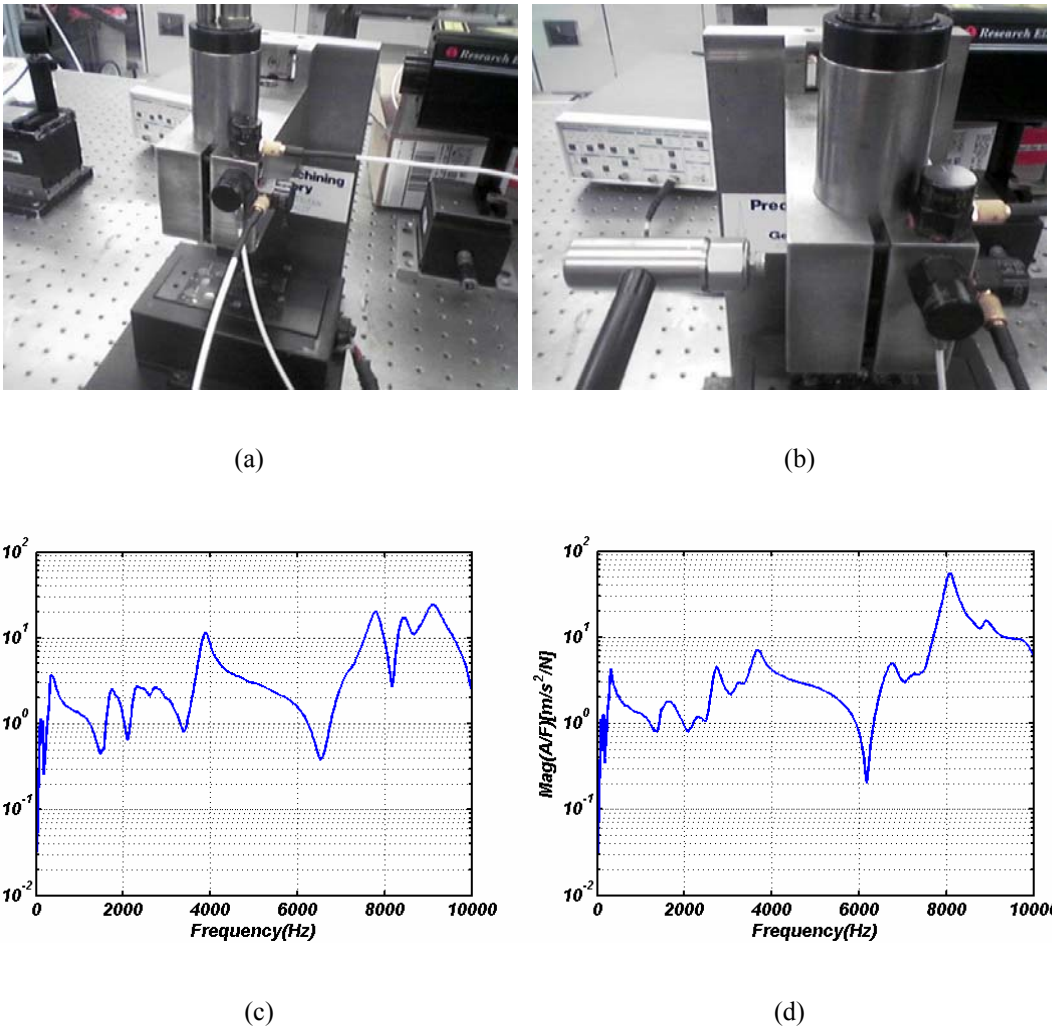

Figure 6-9: (a) Illustration of sensor positions, (b) the hammer impact, (c) the FRF of the case 1 and (d) the case 2 in the y direction

In this experiment, a hammer impact test is adopted as a tool for inspection of the dynamic behavior of miniaturized machine tools. Basically, the vibration of a machine tool is excited by an impulse force, referred to as a hammer impact, and a response of excited vibration is recorded by accelerometers. From the time histories recorded during these tests, frequency response functions (FRFs) can be obtained as shown in Figure 6-9(c) and (d).

The impact hammer used in this study is a medium impact hammer with a metal tip (Kistler type 9722A), and 20 impacts were recorded and averaged linearly. The obtained results for three different sizes are listed in Table 6-3.

6.3.1 Identification of dynamic parameters

Based on these experimental results, the objective functions must be optimized in order to identify the values of springs and damping coefficients at joints. The objective functions for computations of joint stiffness and damping coefficients are obtained from comparisons between experimental and computed results. The forms used in this work are:

$$f = \min\left(abs\left(\sum_{i=1}^{3} \omega_{ni}\left(k_1, k_2, k_3\right) - \omega_{\exp,ni} \right) \right) \tag{6.7}$$

and

$$f = \min\left(abs\left(\sum_{i=1}^{3} \left[\xi_i\left(\alpha_R, \beta_R\right) - \xi_{\exp,i} \right] \right) \right) \tag{6.8}$$

The optimizations of these objective functions are performed using the embedded function 'fminsearch' in MATLAB® based on the Simplex method. This method is generally a robust and simple algorithm that can be applied to many different problems. However, the solutions of this method depend on initial guesses. Based on the aforementioned method, the following values in Table 6-2 are selected to model the dynamic properties of the joints.

Table 6-2: Values of spring and damping parameters

Joint Stiffness			Rayleigh damping	
k_1	k_2	K_3	α_R	β_R
8.81×10^{7}	5.22×10^{9}	5.17×10^{8}	121.79	1×10^{-4}

The computation results obtained for the dynamic properties of this miniaturized machine tool using the above values of spring and damping parameters are compared with experimental data in Figure 6-10.

Table 6-3: Natural frequencies and damping ratios of experimental analysis and modeling

	1^{st} Natural frequency		Damping ratio	
	Experiment	Modeling	Experiment	Modeling
Case1	349.8	321.78	0.202	0.1321
Case2	309.8	320.56	0.1081	0.1309
Case3	299.9	319.3	0.1031	0.1307

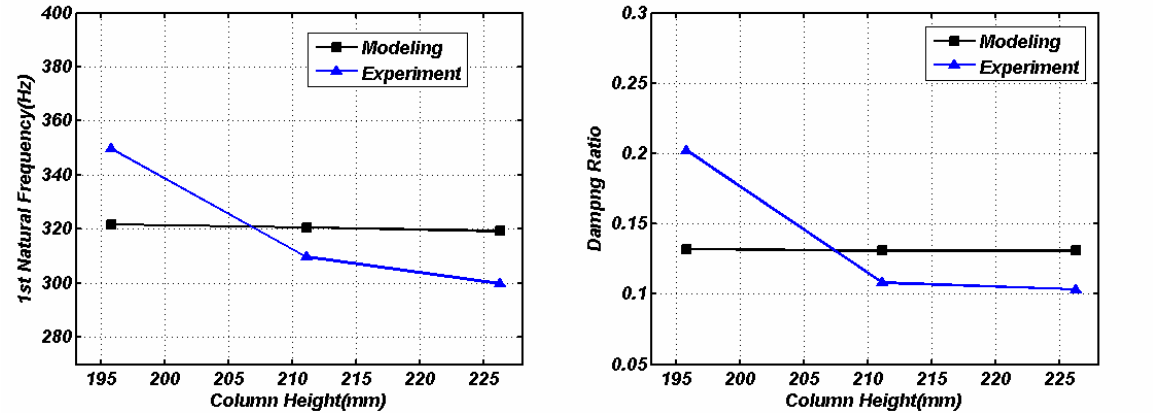

(a) (b)

Figure 6-10: Comparisons between experimental data and modeling values in terms of (a) 1st natural frequency and (b) damping ratio

6.4 Evaluation of machine performance using FEM

In this study, to characterize the performance of a miniaturized machine structure without constructing prototype machines, the trends of the static, thermal, and dynamic stiffness with respect to changing dimensions of the miniaturized machine tools are evaluated through numerical computations based on finite element analysis (FEA) using ANSYS and ABAQUS. This study focuses on the quantitative assessment of the performance effects of the machine tool frame size based on the assumption that the machining table and spindle maintain their performance relative to the variation in the overall size of the machine. In the study, discrete FEM computations of three dimensional nonlinear problems have been performed to obtain the responses of static, thermal, and dynamic deformation with respect to the given constraints. Invar 36 steel alloy was the choice of machine frame material in view of its popularity, stemming from

low thermal expansion and reasonable modulus. It has elastic modulus of 141 GPa, density of 8050 kg/m^3, and thermal expansion coefficient of 1.2×10^{-6}/°C. In the finite element simulations, tetrahedron-type elements defined by twenty nodes, suitable for irregular geometry meshing, are used to mesh a virtual microscale machine structure. During these computations, the bottom surface of the three dimensional structure is constrained.

The results of FEM computations of static and thermal deformation are shown in Figure 6-11(a) and (b).

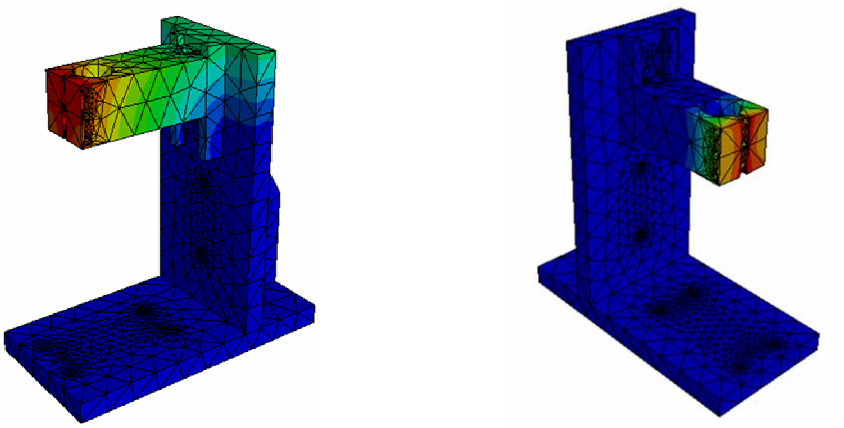

(a) (b)

Figure 6-11: FEM analysis of (a) static and (b) thermal deformation

A comparison between analytical and FEM models shows that the static stiffness of analytical computation is 20%~50% higher than the FEM results in Figure 6-12(a). The reason for this discrepancy is that the deformation caused by a mechanical load isn't evenly distributed on the overhang of the structure. But, in the case of the thermal stiffness, the FEM results are 40% higher than the analytical computational results

because the thermal deformation is concentrated on the tip region of a structure overhang in Figure 6-11(b).

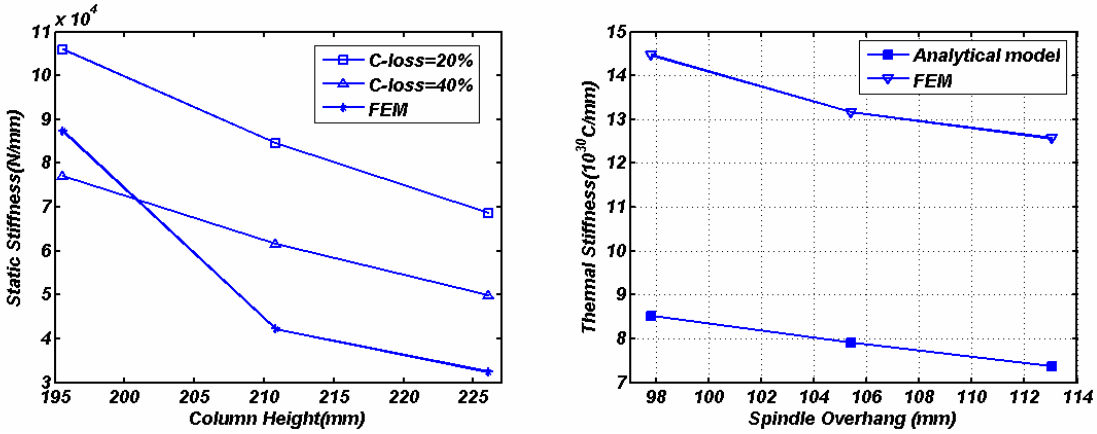

(a) (b)

Figure 6-12: comparisons of (a) static and (b) thermal stiffness

In the context of dynamic rigidity and stability, the important parameters are 1st natural frequency and the damping characteristics. FEM-based model analysis for three different sizes has been performed to identify the dynamic characteristics of the machine structure in Figure 6-13(a), (b), (c), and (d). The results of the modal analysis are summarized in Table 6-4.

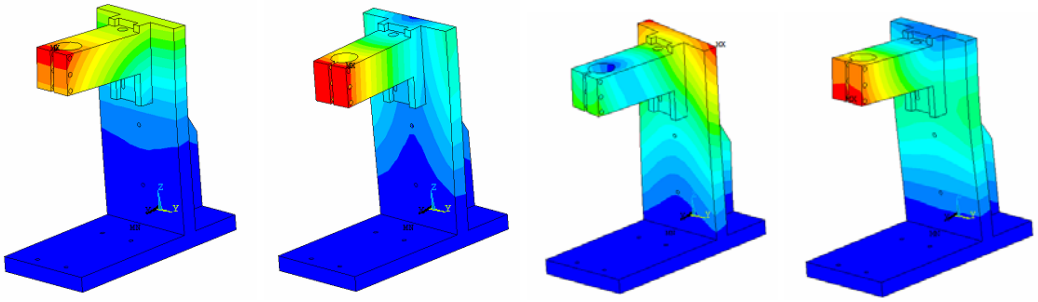

(a) (b) (c) (d)

Figure 6-13: (a)1st, (b)2nd ,(c) 3rd , and (d) 4th modes of machine tool structure

Table 6-4: Summary of structure modes

	1st mode	2nd mode	3rd mode	4th mode
Case1	417.44	438.32	920.79	1096.23
Case2	376.09	393.57	907.30	1025.8
Case3	335.54	349.23	889.72	945.96

The trend of the vibration modes is that there are two modes between 300 and 400 Hz. The results of FEM modal analysis are higher than those of analytical method and experimental data. The damping ratio is calculated using Equation (6.6) and the results of these computations also show higher values than others.

Table 6-5: Natural frequencies and damping ratios of experimentaldata and FEM analysis

	1st Natural frequency		Damping ratio	
	Experiment	FEM	Experiment	FEM
Case1	349.8	417.44	0.202	0.15436
Case2	309.8	376.09	0.1081	0.1439
Case3	299.9	335.54	0.1031	0.1343

Finite element analysis on static rigidity, thermal resistance, and dynamic stiffness shows that miniaturization of machine tools increases the machine's precision. In terms of static stiffness, as the machine's linear dimension decreases, its static stiffness increases. This increase of the static stiffness is a result of the reduction of the frame cantilever lengths in their absolute scales. It is shown that the size reduction of a machine tool decreases its thermal expansion in response to environmental temperature variation since the total volume involved in the expansion is reduced. The dynamic stiffness shows the same trend with other stiffness.

6.5 Volumetric error evaluation

In this study, a kinematic chain representation model, referred to as the form shaping theory [104], is used to estimate the volumetric error of a miniaturized machine tool according to its size. In this method, coordinate transformation, which uses homogenous transform matrix (HTM), is applied to represent the relative displacement between a workpiece and a machine tool as a chain of directly linked rigid components. The mathematical form for computing the result of transformation matrices between a workpiece and a tool is:

$$r_{ideal} = [HTM]_{p_z} \times [HTM]_{p_y} \cdots [HTM]_{B} \times [HTM]_{L_t} \tag{6.9}$$

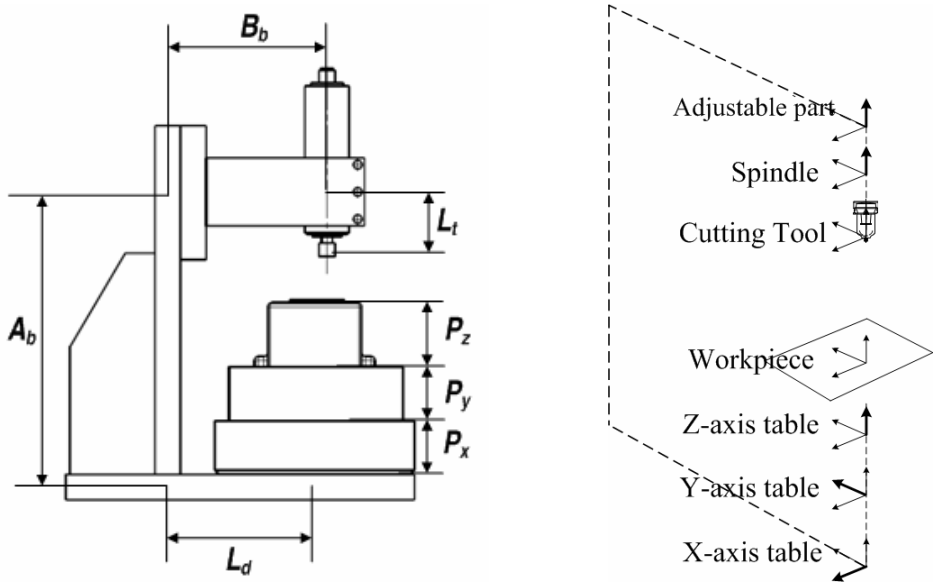

(a) (b)

Figure 6-14: Schematic diagram of (a) the miniaturized machine tool and (b) chain representation

There are many error sources such as alignment errors and geometric errors in actual machine tools. These errors can be considered as errors in transformations between components with an error HTM. The basic form of this matrix is:

$$[HTM]_{error_i} = \begin{vmatrix} 1 & -\gamma_{ei} & \beta_{ei} & \delta_{xei} \\ \gamma_{ei} & 1 & -\alpha_{ei} & \delta_{yei} \\ \beta_{ei} & \alpha_{ei} & 1 & \delta_{zei} \\ 0 & 0 & 0 & 1 \end{vmatrix} \tag{6.10}$$

where α_{ei}, β_{ei}, and γ_{ei} are rotation errors and δ_{xei}, δ_{yei}, and δ_{zei} are translational errors.

Estimation of the resultant assembly volumetric error, which includes the errors between moving components, can be obtained by implementing error HTMs between two ideal HTMs. In this study, the assumptions used to simplify the numerical calculation in miniaturized machine tool accuracy are the following: (i) rigid body motion and (ii) small

errors approximation. With these assumptions, the second, third, and forth orders error terms can be cancelled during the matrix multiplications. After this computation, the relative error between a tool and a workpiece can be obtained as the following:

$$\Delta r = r_{error} - r_{ideal} \tag{6.11}$$

On the basis of the miniaturized milling machine structural drawing in Figure 6-14, the amount of error in each direction, including error terms and machine's dimensions can be obtained as the following:

$$\begin{vmatrix} \Delta x \\ \Delta y \\ \Delta z \end{vmatrix} = \begin{vmatrix} \delta_{x1}+\delta_{x2}+\delta_{x3}+\delta_{x4}+(\beta_1+\beta_2+\beta_2)A_b-\beta_1 P_y-(\beta_1+\beta_2)P_x \\ +(\gamma_{e1}+\gamma_{e2}+\gamma_{e3}+\gamma_{e4})B_b+(\beta_{e1}+\beta_{e2}+\beta_{e3}+\beta_{e4})L_t-\gamma_{e1}W \\ \delta_{ye1}+\delta_{ye2}+\delta_{ye3}+\delta_{y4}+(\gamma_{e1}+\gamma_{e2}+\gamma_{e3})L_d-(\alpha_{e1}+\alpha_{e2}+\alpha_{e3})A_b \\ +(\gamma_{e1}+\gamma_{e2})V+(\alpha_{e1}+\alpha_{e2})P_x+(\alpha_{e1}+\alpha_{e2}+\alpha_{e3}+\alpha_{e4})L_t+\alpha_{e1}P_y \\ \delta_{ze1}+\delta_{ze2}+\delta_{ze3}+\delta_{ze4}-(\alpha_{e1}+\alpha_{e2}+\alpha_{e3}+\alpha_{e4})B_b-(\beta_{e1}+\beta_{e2})V \\ -(\beta_{e1}+\beta_{e2}+\beta_{e3})L_d+\alpha_{e1}W \end{vmatrix} \tag{6.12}$$

where V and W are workpiece sizes.

On the basis of Equation(6.12), the amount of error for each direction can be estimated as Δx , Δy , and Δz . For the purpose of a simple modeling, error terms which are used to compute machine accuracy are assumed to have the amplitude of unity (1μm) for the sake of analysis. The variance of the error amounts has been used to estimate the error magnitude according to a machine size because there are different signs within the computation of error amounts in each axis, which is shown in Equation (6.13)

$$\Delta_x = \Delta x - \Delta x_{ref}, \Delta_y = \Delta y - \Delta y_{ref}, \Delta_z = \Delta z - \Delta z_{ref} \tag{6.13}$$

Then, the mathematical function to compute machine accuracy of the miniaturized milling machine can be expressed as:

$$f_{Assem\_error} = \sqrt{\Delta_x^2 + \Delta_y^2 + \Delta_z^2} \tag{6.14}$$

The volumetric error in this study is computed at the tip of a microscale tool on the basis of the above equations. The magnitudes of this volumetric error are obtained according to different dimensions. These errors are used in Equation(6.14).

6.6 Mathematical computation

Individual computations for key factors such as volumetric error, machine working space, and static, thermal, and dynamic stiffness yielded the computational penalty function. In this study, discrete computation results are translated into the continuous domain using a non-linear regression or analytical solutions to facilitate the quantitative analysis of the penalty functions. Furthermore, the machine work volume is considered as a function of positioning table capability and machine dimensions in the following:

$$f_{volume} = Travel\_X \times Travel\_Y \times (A_b - L_t + P_x + P_y + P_z) \tag{6.15}$$

Finally, the penalty function associated with the miniaturized milling machine can be formulated as the following form:

$$f_{penalty} = c_1 f_{Assem\_error} + c_2 f_{volume} + c_3 f_{static\_stiff} + c_4 f_{thermal\_stiff} + c_5 f_{natural\ frequency} + c_6 f_{damping} \tag{6.16}$$

where C_i is the weighing factor.

After constructing the penalty function, a normalization routine is implemented to identify the variation of each computing parameter. All parameters are divided into

positive effect and negative effect parameters. Generally, larger stiffness parameters, larger work volume, and smaller accuracy values are desired. Thus, considering individual effects, the penalty function is normalized as:

$$f_{Norm\_penalty} = C_1 \frac{f_{Assem\_error}}{f^{\max}_{Assem\_error}} + C_2 \frac{f^{\max}_{volume}}{f_{volume}} + C_3 \frac{f^{\max}_{static\_stiff}}{f_{static\_stiff}} + C_4 \frac{f^{\max}_{thermal\_stiff}}{f_{thermal\_stiff}} + C_5 \frac{f^{\max}_{natural\ frequency}}{f_{natural\ frequency}} + C_6 \frac{f^{\max}_{damping}}{f_{damping}} \quad (6.17)$$

During the mathematical computation, an equal weighing factor is used to find out the optimal dimensions of the miniaturized machine tools. Figure 6-15 shows that the optimal value of the mathematical calculation for analytical representation is around the column height of 220mm for an equal weighing factor. In that case, summaries of other results such as working volume, volumetric error amount, static, thermal, and dynamic stiffness are given in Table 6-6.

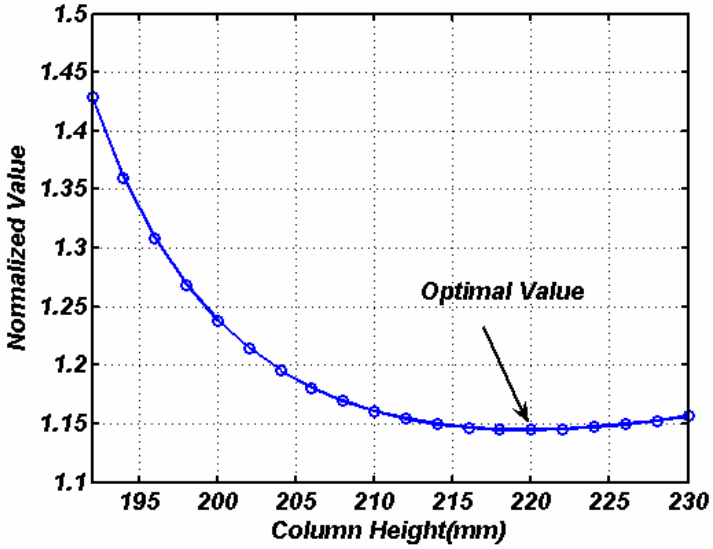

Figure 6-15: Assessment of optimal dimensions of the miniaturized milling machine

Table 6-6: Magnitudes of other parameters at the optimal point of the analytical models

	Values
Volumetric error[mm]	1.55
Working volume[mm^3]	25×25×42
Static stiffness[$\times 10^4$]	7.448
Thermal stiffness[$\times 10^3$]	7.576
1^{st} Natural frequency[Hz]	319.85
Damping ratio	0.1308

Table 6-7: Magnitudes of other parameters at the optimal point of FEM computations

FEM	Values
Volumetric error[mm]	1.4539
Working volume[mm^3]	25×25×26
Static stiffness[$\times 10^4$]	6.23
Thermal stiffness[$\times 10^3$]	13.81
1^{st} Natural frequency[Hz]	393.67[Hz]
Damping ratio	0.1485

The results of the above computation are compared with FEM analysis because FEM has been widely used in analysis for machine tool structures. FEM analysis along with different structure sizes was performed in section 6.4 and then, non-linear regression was taken to proceed to the mathematical computation to find out the optimal point. The result of this computation is summarized in Table 6-7.

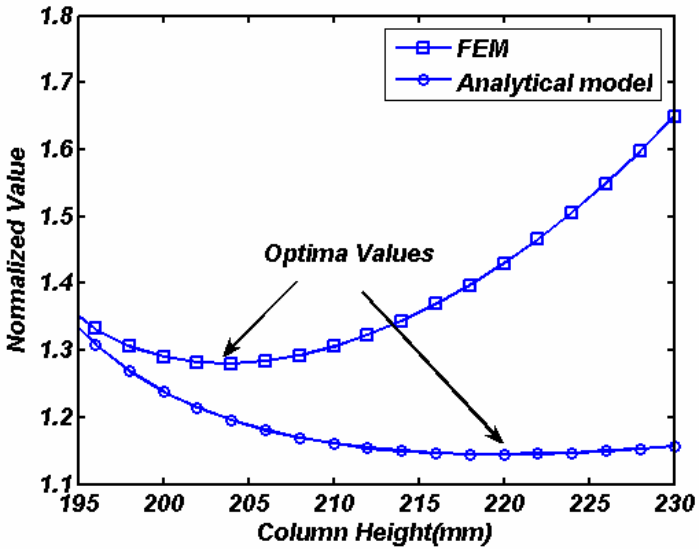

Figure 6-16: A comparison between the analytical models and FEM computations

The result of a comparison between the two methods indicates that there is around 10% difference of the optimal size of the machine tool structure. The optimal point based on FEM provides higher stiffness compared to that of the analytical method.

In the case of micro-machine tools, the ratio of a positioning error to machine work volume is an important factor, which is described in the following:

$$f_{p\_error\_ratio} = \frac{\sqrt{\Delta_{px}^2 + \Delta_{py}^2 + \Delta_{pz}^2}}{Work\ volume} \tag{6.18}$$

Based on Aerotech company's experimental data, which are summarized in Table 6-8, the volumetric positioning error is approximated as 0.464μm.

Table 6-8: Experimental data of Aerotech positioning table

Axes	X axis	Y axis	Z axis
Mean of linear error	0.2307μm	0.3755 μm	0.1460 μm

The machine work volume is computed from Equation(6.15). To implement this parameter, the penalty function is modified as the following:

$$f_{Modified\_penalty} = C_1 \frac{f_{Assem\_error}}{f_{Assem\_error}^{\max}} + C_2 \frac{f_{volume}^{\max}}{f_{volume}} + C_3 \frac{f_{static\_stiff}^{\max}}{f_{static\_stiff}} + C_4 \frac{f_{thermal\_stiff}^{\max}}{f_{thermal\_stiff}} + C_5 \frac{f_{natural\ frequency}^{\max}}{f_{natural\ frequency}} + C_6 \frac{f_{damping}^{\max}}{f_{damping}} + C_7 \frac{f_{p\_error\_ratio}}{f_{p\_error\_ratio}^{\max}} \tag{6.19}$$

The computational results of the above modified penalty function are summarized in Table 6-9. It is found that the difference between an original and modified penalty functions is small.

Table 6-9: Results of the modified penalty function

	Analytical method	FEM
Working volume[mm^3]	25×25×46	25×25×28
Static stiffness[$\times 10^4$]	7.05	5.78
Thermal stiffness[$\times 10^3$]	7.44	13.68
1st Natural frequency[Hz]	319.52	388.1
Damping ratio	0.1306	0.1429

The results of this computation will facilitate the objective decision of design of miniaturized machine tools because this computation can provide cursory technical information according to machine frame sizes. On the other hand, in order to identify the effect of weighing factors such as C_1, C_2, C_5, and C_6, computations based on the L9

matrix of the Taguchi method are carried out. In these computations, C_3 and C_4 are held as constants. The results of this sensitivity analysis of weighing factors in Figure 6-17 show that the working volume weighing factor, C_2, has the dominant effect on the optimal solution of the penalty function.

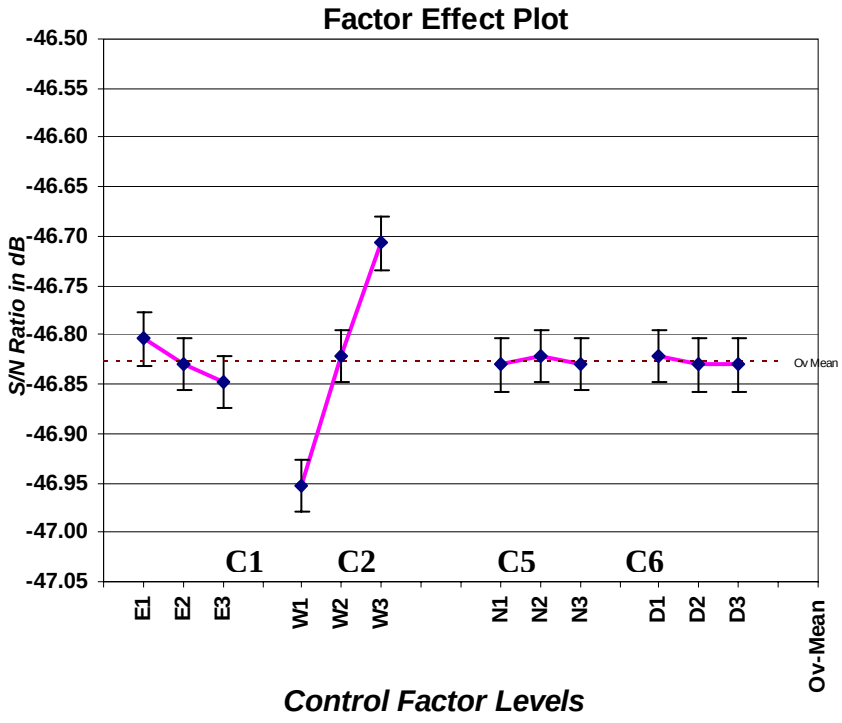

Figure 6-17: The sensitivity analysis of weighing factors

6.7 Summary

In this chapter, an effective design strategy for ensuring the good microscale machine performance and to provide the proper dimensions of the miniaturized manufacturing systems without resorting to physical prototyping was discussed. Then, the optimization of the miniaturized machine tool was performed on the basis of the

proposed design strategy. Individual mathematical modeling of key parameters such as volumetric error, machine working space, and static, thermal, and dynamic stiffness was conducted and supplemented with experimental analysis using a hammer impact test to find out the dynamic characteristics of the joints of the miniaturized machine tools. FEM simulations were carried out as well.

These computations yield the optimal size of the miniaturized machine tool with the technical information of other parameters. A comparison between the analytical method and FEM was carried out. The result of the comparison shows that there is a 10% difference in the optimal size of the machine tool structure.

In addition to this, the sensitivity of optimal machine size with respect to weighing factor of the penalty function was also discussed on the basis of the Taguchi method. It is observed that the working volume weighing factor plays an important role in determining an optimal size for a miniaturized machine tool.

CHAPTER 7

CONCLUSIONS AND RECOMMENDATIONS

7.1 Summary

This dissertation presents a methodology for predicting the micro-grinding forces under given process conditions and a method for optimal dimensioning of a machine structure size according to varying size of the miniaturized machine tools. The model for predicting the micro-grinding forces is as a function of the kinematics of the process, workpiece material properties, and micro-grinding wheel topography. This model starts from the single grit interaction model described in Chapter 3. The new model for the single grit interaction between the workpiece and an individual grit was presented. This single grit interaction model includes both chip formation and ploughing mechanisms. The model can qualitatively predict the single grit forces. To capture the effect of microstructure, the additional stress terms related to the dislocation method were presented. For the assessment of thermal effects in micro-grinding, temperate modeling was also presented. The heat partition ratio to the workpiece was calibrated by the experiment.

In Chapter 4, two methods, the optical and direct methods, to characterize micro-grinding wheel topography were presented. A comparison between them was performed. The computational results for the static cutting edge density show that the result of the direct method is higher than that of the optical method. The distribution of the grit size

was experimentally obtained. Also, the dynamic cutting edge density was obtained as well.

Chapter 5 presents a comprehensive model for predicting micro-grinding forces by integrating the single grit interaction and temperature models discussed in Chapter 3 and the micro-grinding wheel topography discussed in Chapter 4. A sensitivity analysis of this comprehensive model behavior was performed to identify the effects of these parameters. This comprehensive model for predicting the micro-grinding force was compared to experimental data for different process conditions. The computational results show that the predictions driven by this model can capture the trend of the experimental data.

The experiments discussed in Chapter 5 were performed using the miniaturized machine tool. Chapter 6 presents a method for optimization of the machine structure size. This method consists of individual mathematical modeling of key properties of the miniaturized machine tools using the analytical and FEM methods. To identify the kinematics of joints, hammer impact tests were performed. This design method can provide a rough estimation of the performance of the miniaturized machine tools. A sensitivity analysis of the weighing factors was also performed.

7.2 Contributions and Conclusions

The contribution of this dissertation is to establish a comprehensive model for predicting the micro-grinding forces by consolidating mechanical and thermal effects within the single grit interaction model. The size effect of micro-machining and the

crystallographic effect are also included in this model. Additional contributions include characterizing micro-grinding wheel topography and optimal dimensioning of a miniaturized machine structure. Without resorting to expensive and time consuming experiments and physical prototypes, the magnitude of the micro-grinding forces and the performance of the miniaturized machine tools can be quantitatively estimated.

The following conclusions and contributions from Chapter 3 can be drawn

- Developed a model to describe the single grit interaction between the workpiece and the individual grit including the chip formation and ploughing mechanisms. This model is also a function of the kinematics of the process
- Developed a model for assessing the thermal effects of micro-grinding based on the Jaeger's moving heat model
- Calibrated the heat partition ratio to the workpiece in micro-grinding based on the temperature matching and embedded thermocouple techniques. The computation result shows that the heat transfer to the workpiece is around 40%.
- Developed a material model by incorporating crystallographic effects. These effects are implemented as the additional stress term based on the dislocation theory

The following conclusions and contributions from Chapter 4 can be drawn

- Performed the characterization of micro-grinding wheel topography using the optical and direct methods. The static cutting edge density obtained from the direct method is higher than that obtained by using the optical method.
- Extracted the size of grit, the static and dynamic cutting edge density using the direct method. The average sizes of grits are 41μm for worn tools and 44μm for fresh tools. The number of grits of worn tools is less than that of fresh tools. Computations of the dynamic cutting edge shows that 10~30% of the static cutting edges are engaged in micro-grinding at high depths of cut.

The following conclusions and contributions from Chapter 5 can be drawn

- Validate the model for predicting micro-grinding forces based on side micro-grinding setup. These experiments were performed using the miniaturized machine tool. The results show that the model captures the trend of the experiments
- Performed a sensitivity analysis of the model behavior and experimental outputs. The parameters that highly influence outputs in these analysis are the size of grit for the model behavior and the size of the micro-grinding wheel for experimental outputs

- Assessed the thermal effect in micro-grinding. The temperature rise is small within the input range

The following conclusions and contributions from Chapter 6 can be drawn

- Proposed a design method based on mathematical models of key parameters such as volumetric error, machine working space, and static, thermal, and dynamic stiffness using the analytical and FEM methods.
- Performed hammer impact tests to identify the dynamic characteristics of joints
- Estimated the optimal size of a machine tool structure with assessment of the machine performance.
- Performed a sensitivity analysis of the weighing factors

7.3 Recommendations

The current research provides a physical foundation to predict the micro-grinding forces and optimize the dimensions of a miniaturized machine structure. Since these research fields are relatively new areas, there are opportunities for improvement. The recommendations for future work are described.

7.3.1 Modeling of the micro-grinding wheel wear

Micro-grinding wheel topography is a critical factor to predict the micro-grinding process and changes due to the wear mechanism. The difference of the grit size between worn tools and fresh tools was investigated in this study. There is a need to develop a wear model representing the wear mechanism of the micro-grinding wheel because experimental techniques using SEM and white interferometer require costly and time consuming experiments. The other aspect is that the micro-grinding process can be interrupted during the wear tests. The wear model for the micro-grinding wheel can be developed from the single grit interaction model described in this thesis.

7.3.2 Analysis of the space between grit behavior

Some chips created by micro-grinding are trapped within the space between neighboring grits. These trapped chips influence the micro-grinding process by preventing the engagement of other grits and polishing the workpiece. The characterization of the grit space behavior can provide better predictions of the micro-grinding process. The model has to correlate the process condition inputs with the surface roughness and micro-grinding forces.

7.3.3 Predictive modeling of surface roughness

The surface roughness is important to the value of products. For micro-grinding, the comprehensive model has to be established. Modeling of surface roughness could start from the comprehensive force model described in this thesis. But, other aspects such

as the elastic recovery and the interfacial strength have to be implemented in that comprehensive model for predicting the surface roughness.

7.3.4 Optimization of the micro-grinding process

Based on the models described and recommended in this thesis, the process conditions of micro-grinding can be optimized using numerical techniques such as multi-criteria optimization. This optimization provides improvement of the micro-grinding process capability.

7.3.5 Performance evaluation techniques of miniaturized machine tools

Due to advantages of the miniaturized machine tool, many prototypes have been developed and have shown the good capability. But, there are no test standards to evaluate their performance. Development and standardization of performance evaluation techniques for miniaturized machine tools provides a good foundation for the design of advanced miniaturized machine tools.

REFERENCES

1. Liang, S. Y., 2004, "Machining and Metrology at Micro/Nano Scale," *1st International Coference on Positioning Technology*,Act-city, Hamamatsu,Japan, pp 23-28.

2. Cox, D., Newby, G., Park, H. W., Liang, S. Y., 2004, "Performance evaluation of a miniaturized machining center for precision manufacturing," *2004 ASME International Mechanical Engineering Congress and Exposotion*,Anaheim, California USA.

3. Kussul, E. M., Rachkovskij, D. A., Baidyk, Y. N., Talayev, S. A., 1998, "Micromechanical Engineering: a Basis for the Low-cost Manufacturing of Mechanical Microdevices using Microequipment," Journal of Micromech. Microeng, **6**, pp 410-425.

4. Kitahara, T., Ishikawa, Y., Terada, T., Nakajima, N., Furuta, K., 1996, "Development of Micro-lathe," Mechanical Lab. Report, pp 50(55):117-123.

5. Lu, Z., Yoneyama, 1999, "Micro Cutting in the Micro Lathe Turning System," International Journal of Machine Tools and Manufacture, **39**(7), pp 1171-1183.

6. Mishima, N., Asida, K., Tanikawa, T., Maekawa, H., Kaneko, K., M.Tanaka, 2000, "Microfactory and a design evalution method for miniature machine tools," *Proceedings for ASPE 15th Annual Meeting*,Phoenix,AZ.

7. Vogler, M. P., Liu, X., Kapoor, S. G., DeVor, R. E., Ehmann, K. F., 2002, "Development of Meso-Scale Machine Tool (mMT) Systems," Trans of North American Manufacturing Research Instituti, pp 653-661.

8. Kapoor, S. G., DeVor, R. E., Ehmann, K. F., 2004, "Current State of Micro-Scale Machine Tool Systems and Machining Research," *Presentation at the WTEC U.S. Review Workshop on MIcro-Manufacturing*,Arlington, VA.

9. Rahman, M. A., Rahman, M., Kumar, A. S., Lim, H. S., 2005, "CNC microturning : an application to miniaturization," International Journal of Machine Tools and Manufacture, **45**, pp 631-639.

10. Kurita, T., Hattori, M., 2005, "Development of new-concept desk top size machine tool," International Journal of Machine Tools and Manufacture, **45**, pp 959-965.

11. Lee, J. H., Park, S. R., Yang, S. H., 2006, "Machining a micro/meso scale structure using a minaturized machine tool by using a conventional cutting

process," Journal of Manufacturing Science and Engineering, Transactions of the ASME, **128**(3), pp 820-825.

12. Chen, H., Mayer, T., Ni, J., 2004, "A virtual machine tool(vmt) integrated design environment and its application to meso-scale machine tool development," Transactions of NAMRI/SME, **32**, pp 327-334.

13. Okazaki, Y., Mori, T., Morita, N., 2001, "Desk-top NC milling Machine with 200 krpm Spindle," *In Proc. ASPE Annual Meeting*, pp 192-195.

14. Lin, W., Ohmori, H., Uehara, Y., Asami, M., Ohmori, M., 2004, "Development and Characteristic on the Desk-top 4-Axes Machine "TRIDER-X" for Micro-fabrication," *4th International Workshop on Microfactories (IWMF2004)*,Shanghai, China.

15. Williams, R. E., Melkote, S., Sun, W., Huang, Y., Kinsey, B., Yao, D., 2005, "Recent advances in micro/meso-scale manufacturing processes," Orlando, FL, United States **16-2**, pp 863-884.

16. Phsik Instrumente (PI) GMBH & Co., 2004, "PZT Flexure NanoPositioners and Scanner," *Physik Instrumente Nanopositioners Catalogue*.

17. Slocum, A. H., 1994, *Precision Machine Design*.

18. Lee, S. W., Mayor, R., Li, J., 2006, "Dynamic Analysis of a Mesoscale Machine Tool," Journal of Manufacturing Science and Engineering, **128**, pp 194-203.

19. Mishima, N., Ishii, K., 1999, "Robustness Evaluation of a Miniaturized Machine Tool," *25th Design Automation Conference*,Las Vegas, Nevada.

20. Mishima, N., 2003, "Design of a miniature manufacturing system for micro-fabrication," *10th ISPE International Conference on Concurrent Engineering*,Swets & Zeitlinger, Lisse, pp 1129-1135.

21. Hahn, R. S., Lindsay, L. P., 1982D, "Principles of Grinding Part4.Surface Finish,Geometry, and Integrity," Grinding: theory, techniques and trouble shooting,SME, pp 25-35.

22. Hahn, R. S., Lindsay, R. P., 1982A, "Principles of Grinding Part1.The Metal Removal Parameter," Grinding: theory, techniques and trouble shooting,SME, pp 3-10.

23. Hahn, R. S., Lindsay, R. P., 1982B, "Principles of Grinding Part2.The Metal Removal Parameter," Grinding: theory, techniques and trouble shooting,SME, pp 11-17.

24. Hahn, R. S., Lindsay, R. P., 1982C, "Principles of Grinding Part3.The Wheel Removal Parameter," Grinding: theory, techniques and trouble shooting,SME, pp 18-24.

25. Malkin, S., 1989, *Grinding Technology: Theory and Application of Machining with Abrasives*, Ellis Horwood Limited, New York.

26. Shaw, M., 1996, *Principles of Abrasive Processing*, Oxford University Press, New York.

27. Tönshoff, H., Peters, J., Inasaki, I., Paul, T., 1992, "Modeling and Simulation of Grinding Processes," Annals of CIRP, **42/2**, pp 677-688.

28. Shaw, M., 1972, "Fundamentals of Grinding," *Proceeding of the International Grinding Conference: New Developments in Grinding*, Pittsburgh, Pennsylvania, pp 221-258.

29. Maan, N., Groenou, A. B. V., 1977, "Low Speed Scratch Experiments on Steels," Wear, **42**, pp 365-390.

30. Komanduri, R., 1971, "Some aspects of machining with negative rake tools simulating grinding," Int.J.Mach. Tool Des., **11**, pp 223-233.

31. Torrance, A., 1981, "A New Approach to the Mechanics of Abrasion," Wear, **67**, pp 233-257.

32. Challen, J. M., Oxley, P. L. B., 1978, "An explanation of the different regimes of friction and wear using asperity deformation models," Wear, **53**, pp 229-243.

33. Williams, J. A., Xie, Y., 1992, "The generation of worn surfaces by the repeated interaction of parallel grooves," Wear, **164**, pp 864-872.

34. Jaeger, J. C., 1942, "Moving sources of heat and temperature at sliding contacts," Royal Society of New South Wales -- Journal and Proceedings, **76**(Part 3), pp 203-224.

35. Outwater, J. O., Shaw, M. C., 1952, "Surface temperatures in grinding," American Society of Mechanical Engineers -- Transactions, **74**(1), pp 73-81.

36. Hahn, R. S., 1962, "On the Nature of the Grinding Process," *Proceeding of the 3rd MTDR Conference*, pp 129-154.

37. Malkin, S., 1973, "Review of materials processing literature em dash 1969-1972 em dash 2. grinding," Journal of Engineering for Industry, Transactions of the ASME, **95 Ser B**(1), pp 299-306.

38. Malkin, S., 1974, "Thermal aspects of grinding em dash 2. surface temperatures and workpiece burn," Journal of Engineering for Industry, Transactions of the ASME, **96 Ser B**(4), pp 1184-1191.

39. Malkin, S., Anderson, R. B., 1974, "Thermal aspects of grinding em dash 1. energy partition," Journal of Engineering for Industry, Transactions of the ASME, **96 Ser B**(4), pp 1177-1183.

40. Ramanath, S., Shaw, M. C., 1988, "Abrasive grain temperature at the beginning of a cut in fine griding," ASME Journal of Engineering for Industry **110**, pp 15-18.

41. Werner, P. G., Younis, M. A., Schlingensiepen, R., 1980, "Creep feed em dash an effective method to reduce work surface temperatures in high-efficiency grinding processes," Manufacturing Engineering Transactions, pp 312-331.

42. Xu, X., Malkin, S., 2001, "Comparison of Methods to Measure Grinding Temperatures," Journal of Manufacturing Science and Engineering, **123**, pp 191-195.

43. Rowe, W. B., Black, S. C. E., Mills, B., Qi, H. S., Morgan, M. N., 1995, "Experimental investigation of heat transfer in grinding," CIRP Annals - Manufacturing Technology, **44**(1), pp 329-332.

44. Kohli, S., Guo, C., Malkin, S., 1995, "Energy partition to the workpiece for grinding with aluminum oxide and CBN abrasive wheels," Journal of Engineering for Industry, Transactions of the ASME, **117**(2), pp 160-168.

45. König, W., 1975, "Properties of cutting edges related to chip formation in grinding," Annals of the CIRP, **24/1**, pp 231-236.

46. Verkerk, J., Peters, J., 1977, "Final report concerning cirp cooperative work on the characterization of grinding wheel topography," Annals of the CIRP, **26**(2), pp 385-395.

47. Younis, M. A., Alawi, H., 1984, "Probabilistic analysis of the surface grinding process," Transactions of the Canadian Society for Mechanical Engineers, **8**(4), pp 208-213.

48. König, W., Lortz, w., 1974, "Three dimensional measurement of the griding wheel surface-Evaluation and Effect of Cutting Behavior," Annals of the CIRP, **23/1**, p 231.

49. Brough, D., Bell, W. F., Rowe, W. B., 1981, "Achieving and monitoring high-rate centreless grinding," Swansea, Wales, pp 313-322.

50. Cai, R., 2002, "Assessment of Virtrified CBN Grinding Wheels for Precision Grinding," Ph.D, Liverpool John Moores University

51. Hacker, R. L., 2002, "Part surface roughness modeling and process optimal control of cylindrical grinding," Ph.D, Mechanical engineering, Georgia Institute of Technology

52. Subbiah, S., Melkote, S. N., 2004, "On the size effect in micro-cutting at low and high rake angles," Anaheim, CA, United States **15**, pp 485-493.

53. Shaw, M. C., 1950, "A quantitized theory of strain hardening applied to the cutting metals," Journal of Applied Physics, **21**(6), p 599.

54. Backer, W. R., Marshall, E. R., M.C.Shaw, 1952, "The size effect in metal cutting," Trans. of ASME, pp 61-74.

55. Nakayama, 1968, "Size effect in metal cutting force," J.of engg. for ind., p P119.

56. Atkins, A. G., 2003, "Modelling metal cutting using modern ductile fracture mechanics: Quantitative explanations for some longstanding problems," International Journal of Mechanical Sciences, **45**(2), pp 373-396.

57. Makino, Suto, Fokushima, 1966, "An Experimental Investigation of the Grinding Process," Journal of Mech. Laboratory of Japan, **12**(1), p 17.

58. Albrecht, P., 1960, "New developments in the theory of the metal-cutting process," Transaction of the ASME, p P348.

59. Dinesh, D., Swanminathan, S., Chandrasekar, S., Farris, T. N., 2001, ""An intrinsic size-effect in machining due to the strain gradient"," *Symposium in Fundamental Issues in Machining, Proceedings of ASME IMECE*, pp pp. 197-204.

60. Joshi, S. S., Melkote, S. N., 2004, "An explanation for the size-effect in machining using strain gradient plasticity," Journal of Manufacturing Science and Engineering, Transactions of the ASME, **126**(4), pp 679-684.

61. Liu, K., Melkote, S. N., 2004, "A strain gradient based finite element model for micro/meso-scale orthogonal cutting process," Proceedings of 2004 Japan-USA Symposium on Flexible Automation

62. Moriwaki, T., 1995, "Experimental analysis of ultra-precision machining," Int. J. Japan Soc. Precision Engng, **29**(4), pp 287-290.

63. Ueda, K., Iwata, K., 1980, "Chip formation mechanism in single crystal cutting of beta -brass," Annals of the CIRP, **29**(1), pp 41-46.

64. Sato, M., Yamazaki, T., Shimizu, Y., Takabayashi, T., 1991, "Study on the microcutting of aluminum single crystals," JSME International Journal, Series 3: Vibration, Control Engineering, Engineering for Industry, **34**(4), pp 540-545.

65. Von Turkovich, B. F., Black, J. T., 1970, "Micro-machining of copper and aluminum crystals," **92 Ser B**(1), pp 130-134.

66. Furukawa, Y., Moronuki, N., 1988, "Effect of Material Properties on Ultra Precise Cutting Processes," CIRP Annals, **37**, pp 113-116.

67. Chuzhoy, L., DeVor, R. E., 2003, "Machining simulation of ductile iron and its constituents, Part 2: Numerical simulation and experimental validation of machining," Journal of Manufacturing Science and Engineering, Transactions of the ASME, **125**(2), pp 192-201.

68. Chuzhoy, L., DeVor, R. E., Kapoor, S. G., Beaudoin, A. J., Bammann, D. J., 2003, "Machining simulation of ductile iron and its constituents, Part 1: Estimation of material model parameters and their validation," Journal of Manufacturing Science and Engineering, Transactions of the ASME, **125**(2), pp 181-191.

69. Feng, J., Kim, G. Y., Shih, A. J., Ni, J., 2007, "Investigation of Tool Wear in Microgrinding of Ceramic Materials with Sintered Metal_bonded Wheel," *2nd international conference in micromanufacturing*,Greenville, SC.

70. Gilormini, P., Felder, E., 1983, "Theoretical and experimental study of the ploughing of a rigid-plastic semi-infinite body by a rigid pyramidal indenter," Wear, **88**(2), pp 195-206.

71. Basuray, P. K., Misra, B. K., Lal, G. K., 1977, "Transition from ploughing to cutting during machining with blunt tools," Wear, **43**(3), pp 341-349.

72. Ikawa, N., Shimada, S., Tanaka, H., Ohmori, G., 1991, "Atomistic analysis of nanometric chip removal as affected by tool-work interaction in diamond turning," Palo Alto, CA, USA **40**, pp 551-554.

73. Liu, K., Li, X., 2001, "Modeling of ductile cutting of tungsten carbide," transaction of NAMRI/SME, pp 251-258.

74. Son, S. M., Lim, H. S., Ahn, J. H., 2005, "Effects of the friction coefficient on the minimum cutting thickness in micro cutting," International Journal of Machine Tools & Manufacture, **45**, pp 529-535.

75. Masuko, M., 1956, "Fundamental research on the metal cutting-second report," Bull. of Japan soc. of mech. engg., **22**(118), p p371.

76. Sin, H., Saka, N., Suh, N. P., 1979, "Abrasive wear mechanisms and the grit size effect," Wear, **55**(1), pp 163-190.

77. Goddard, J., Wilman, H., 1965, "A theory of friction and wear during the abrasion of metals," Wear, **5**, pp 114-135.

78. Bhushan, B., 1999, *Tribology and Mechanics of Magnetic Storage Devices*, Springer-Verlag, New york.

79. Merchant, M. E., 1945, "Mechanics of metal cutting process, and type 2 chip," Journal of Applied Physics, **16**(6), pp 318-324.

80. Bil, H., Kilic, S. E., Tekkaya, A. E., 2004, "A comparison of orthogonal cutting data from experiments with three different finite element models," International Journal of Machine Tools and Manufacture, **44**(9), pp 933-944.

81. Johnson, G. R., Cook, W. H., 1985, "Fracture Characteristics of Three Metals Subjected to Various Strains, Strain Rates, Temperatures and Pressures," Engineering Fracture Mechanics **21**(1), pp 31-48.

82. Oxley, P. L. B., 1989, *The Mechanics of Machinin: An Analytical Approach to Assessing Machinability*, E. Horwood, New York.

83. Manjunathaiah, J., Endres, W. J., 2000, "A New Model and Analysis of Orthogonal Machining With an Edge-Radiused Tool," Journal of Manufacturing Science and Engineering, **122**, pp 384-390.

84. Hughes, D. A., Liu, Q., Chrzan, D. C., Hansen, N., 1997, "Scaling of microstructural parameters: misorientations of deformation induced boundaries," Acta mater, **45**(1), pp 105-112.

85. Keith, R. W., 1997, "Numerical scheme for extracting strength model coefficients from Taylor test data," International Journal of Impact Engineering, **19**(9-10), pp 797-810.

86. Boyer, H. E., Gall, T. L., 1985, *Metals Handbook*, American Society for Metals, Materials Park, OH.

87. Furukawa, M., Horita, Z., Nemoto, M., Valiev, R. Z., Langdon, T. G., 1996, "Microhardness measurements and the Hall-Petch relationship in an Al-Mg alloy with submicrometer grain size," Acta Materialia, **44**(11), pp 4619-4629.

88. Totten, G. E., Mackenzie, D. S., 2003, *Handbook of Aluminum*, CRC Press, New York.

89. Nabarro, F. R. N., Basinski, Z. S., Holt, D. B., 1964, "Plasticity of pure single crystals," Advances in Physics, **13**(50), pp 193-323.

90. Liu, Q., Jensen, D. J., Hansen, N., 1998, "Effect of grain orientation on deformation structure in cold-rolled polycrystalline aluminium," Acta mater, **46**(16), pp 5819-5838.

91. Kang, S. H., Bang, W. H., Cho, J. H., Han, H. N., Oh, K. H., Lee, C. G., Kim, S.-J., 2005, "Microtexture Analysis of Friction Stir Welded Al 6061-T651 Plates," Materials Science Forum, **495-497**, pp 901-906.

92. Furukawa, M., Iwahashi, Y., Horita, Z., Nemoto, M., Tsenev, N. K., Valiev, R. Z., Langdon, T. G., 1997, "Structural evolution and the Hall-Petch relationship in an Al-Mg-Li-Zr alloy with ultra-fine grain size," Acta Materialia, **45**(11), pp 4751-4757.

93. Rowe, W. B., Black, S. C. E., Morgan, M. N., Qi, H. S., 1997, "Grinding Temperature and Energy Partitioning," *Proceeding Royal Society, Part A*,**453**, pp 1083-1104.

94. Rowe, W. B., Morgan, M. N., Qi, H. S., Zheng, H. W., 1993, "Effect of deformation on the contact area in grinding," CIRP Annals, **42**(1), pp 409-412.

95. Shi, Z., Malkin, S., 2006, "Wear of electroplated CBN grinding wheels," Journal of Manufacturing Science and Engineering, Transactions of the ASME, **128**(1), pp 110-118.

96. Hou, Z. B., Komanduri, R., 2003, "On the mechanics of the grinding process - Part I. Stochastic nature of the grinding process," International Journal of Machine Tools and Manufacture, **43**(15), pp 1579-1593.

97. Geertruyden, W. H. V., Misiolek, W. Z., Wang, P. T., 2006, "Grain structure evolution in a 6061 aluminum alloy during hot torsion," Materials Science and Engineering A, **419**(1-2), pp 105-114.

98. Brown, J. A. C., Aitchison, J., 1957, *The Lognormal Distribution*, Cambridge University Press, Cambridge (UK).

99. Mackenzie, J. K., 1958, "Second Paper on Statistics Associated with the Random Disorientation of Cubes," Biometrika, **45**(1/2), pp 229-240.

100. Mishima, N., Asida, K., Tanikawa, T.,Maekawa, H.,Kaneko, K. and Tanaka, M. , 2000, "Microfactory and a design evalution method for miniature machine tools," *Proceedings for ASPE 15th Annual Meeting*,Phoenix,AZ.

101. T.Kurita, M. H., 2005, "Development of new-concept desk top size machine tool," International Journal of Machine Tools and Manufacture, **45**, pp 959-965.

102. Vogler., M. P., Liu, X., Kapoor, S. G., DeVor, R. E., Ehmann, K. F., 2002, "Development of Meso-Scale Machine Tool (mMT) Systems," In Trans of North American Manufacturing Research Institution, pp 653-661.

103. Clough, R. W., Penzien, J., 1993, *Dynamics of Structures*, McGraw-Hill, New York.

104. Reshtov, D. N., Portman, V. T., 1988, *Accuracy of Machine Tools*, ASME press, New York.

VITA

Hyung Wook Park was born in Hwan-Do island on Nov. 11, 1975 and grew in Gwang-ju City. He received a Bachelor of Science degree in Mechanical Engineering in January, 2000 from Seoul National University, Korea. After graduation, he attended the graduate school of Seoul National University completing his Master of Science degree in Mechanical Engineering in January, 2002. Then, he joined the Hyundai Motor Company R&D team as a research engineer where he was responsible for design and development of passenger cars for a period of two years.

He had a chance to pursue a Doctor of Philosophy degree in Mechanical Engineering at Georgia Institute of Technology in August, 2003. He performed research on micro-manufacturing and the development of miniaturized manufacturing systems under the supervision of Dr. Steven Liang.